Supporting information

for

Design of Pure Heterodinuclear Lanthanoid Cryptate Complexes

Christian D. Buch,[a] Steen H. Hansen,[a] Dmitri Mitcov,[a] Camilla M. Tram,[a] Gary S. Nichol,[b] Euan K. Brechin,[b] and Stergios Piligkos[a]*

[a]Department of Chemistry, University of Copenhagen, DK-2100 Copenhagen, Denmark
[b]EaStCHEM School of Chemistry, University of Edinburgh, Edinburgh, UK

Contents

Materials and Methods

Materials. During the syntheses no attempts were made to exclude neither moisture nor oxygen. All solvents were purchased commercially and used as received. Tris(2-aminoethyl)amine (tren) and tetrabutylammonium nitrate were also obtained commercially and used as received. 2,6-diformyl-*p*-cresol was obtained following a literature procedure.[1] For its synthesis glacial acetic acid, conc. sulfuric acid, paraformaldehyde, *p*-cresol and hexamethylenetetramine were obtained commercially and used as received. The $Ln(OTf)_3 \cdot xH_2O$ salts were obtained following a literature procedure[2] and their water content was checked using an EDTA titration with xylenol orange as the indicator.

Mass Spectrometry. MALDI mass spectrometry was performed on a Bruker Solarix XR 7T ESI/MALDI FT-ICR MS at The Department of Chemistry University of Copenhagen.

NMR Spectroscopy. ^{1}H and ^{13}C NMR spectra were recorded on a Bruker 500 MHz instrument with a cryoprobe. Calibration of the ^{1}H and ^{13}C NMR was done against the deuterated solvent signal.

Infrared Spectroscopy. IR spectra were recorded on an Agilent Technologies Cary 630 FTIR.

Elemental Analyses. CHNS elemental analyses were obtained using a FLASHEA 1112 instrument at The Microanalytical Laboratory at The Department of Chemistry University of Copenhagen.

Powder X-ray Diffraction. Powder X-ray diffraction (PXRD) data were obtained using a BRUKER D8 ADVANCE powder diffractometer employing a Cu *K*α radiation (λ = 1.5418 Å) source.

Single-Crystal X-ray diffraction. Single crystals of $\mathbf{1_N}$-$\mathbf{10_N}$ were measured at 100 K on a BRUKER D8 VENTURE diffractometer equipped with a Mo *K*α high-brilliance IμS S3 radiation source (λ = 0.71073 Å), a PHOTON 100 CMOS detector and an Oxford Cryosystems cooling system. The APEX2 software package was used to control the setup. The applications SAINT[3] and SADABS[4] were used for the data reduction and absorption corrections of the data, respectively. Structures were solved with SHELXT[5] and refined using SHELXL,[6, 7] interfaced through Olex2.[8, 9] O-bound H atoms were identified from a difference map and refined with geometric restraints; H-atom coordinates were fixed in disordered water, following a few cycles of refinement. C-bound H atoms were placed at calculated positions. Substitutional disorder in heterodinuclear complexes was modelled using EXYZ/EADP constraints on the metal atom sites and the occupancies refined using a free variable. One of the nitrate ligands was modelled as disordered in some complexes using geometric and displacement ellipsoid similarity restraints. The nitrate counter ion was modelled as disordered with a water molecule over two sites consistent with peaks in a difference map.

Magnetometry. Direct current magnetic susceptibility measurements were performed on polycrystalline samples of $\mathbf{1_N}$-$\mathbf{5_N}$, $\mathbf{8_N}$ and $\mathbf{10_N}$ fixated in *n*-hexadecane using a Quantum-Design MPMS-XL SQUID magnetometer. χT data were corrected for diamagnetism of the sample and *n*-hexadecane following Pascal's constants.

Electron paramagnetic resonance. The spectra were recorded on a Bruker Elexsys E500 instrument.

Luminescence spectroscopy. The spectra were recorded on a Horiba-Jobin Yvon Fluorolog fluorimeter equipped with an InGaAs near-infrared detector

Synthesis and Characterisation

Synthesis of 1·3H$_2$O. To a pyridine (60 ml) solution of Gd(OTf)$_3$·9H$_2$O (500 mg; 0.65 mmol) YbL·4H$_2$O (200 mg; 0.22 mmol) is added. When a clear orange solution has formed, the solution is heated to boiling and refluxed for 3 hours. After being refluxed the solution is cooled to room temperature and then poured into diethyl ether (300 ml) which is vigorously stirred. This produces a fine orange precipitate which is isolated, washed twice with diethyl ether (2 x 100 ml) and then dried. The product is then extracted with dichloromethane (100 ml). The orange dichloromethane solution is filtered and evaporated to dryness. To the orange precipitate THF (25 ml) is added and the mixture is stirred overnight (in some cases all the precipitate dissolves at first, but overnight a pale yellow precipitate forms). The pale yellow precipitate is isolated and washed with THF (3x15 ml) and diethyl ether (2x10 ml). Yield: 217 mg (66 %). Analysis calculated for $C_{42}H_{51}F_9N_8O_{15}S_3YbGd$. Calcd.: C, 33.51; H, 3.41; N, 7.44; S, 6.39. Found: C, 34.03; H, 3.49; N, 7.38; S, 6.60. IR(ν=N): 1636 cm^{-1} (Figure S28). MALDI-MS positive mode: 1303.15 *m*/*z* $[YbGdL(OTf)_2]^+$ (Figure S1).

Synthesis of 2-9. The syntheses of **2** - **9** were performed analogously to **1**. However, for **2**, **3**, **4** and **7** five equivalents of Y(OTf)$_3$·9H$_2$O, Yb(OTf)$_3$·9H$_2$O, Yb(OTf)$_3$·9H$_2$O and Lu(OTf)$_3$·9H$_2$O were used, respectively. In addition, **3**, **4** and **7** were refluxed for 24 hours.

Synthesis of 2·3H$_2$O. YbL·4H$_2$O (200 mg; 0.22 mmol), Y(OTf)$_3$·9H$_2$O (760 mg; 1.1 mmol), refluxed 5 hr. Yield: 107 mg (34 %). Analysis calculated for $C_{42}H_{51}F_9N_8O_{15}S_3YbY$. Calcd.: C, 35.10; H, 3.58; N, 7.80; S, 6.69. Found: C, 35.40; H, 3.78; N, 7.17; S, 6.55. IR(ν=N): 1636 cm^{-1} (Figure S29). MALDI-MS positive mode: 1234.14 *m*/*z* $[YbYL(OTf)_2]^+$ (Figure S2).

Synthesis of 3·2H$_2$O. LuL·4H$_2$O (200 mg; 0.22 mmol), Yb(OTf)$_3$·9H$_2$O (850; 1.1 mmol), refluxed for 1 day. Yield: 46 mg (14 %). Analysis calculated for $C_{42}H_{49}F_9N_8O_{14}S_3YbLu$. Calcd.: C, 33.52; H, 3.28; N, 7.45; S, 6.39. Found: C, 33.44; H, 4.16; N, 7.13; S, 6.58. IR(ν=N): 1637 cm^{-1} (Figure S30). MALDI-MS positive mode: 1320.15 *m*/*z* $[LuYbL(OTf)_2]^+$ (Figure S3).

Synthesis of 4·3H$_2$O. YbL·4H$_2$O (200 mg; 0.22 mmol), Yb(OTf)$_3$·9H$_2$O (852; 1.1 mmol), refluxed for 1 day. Yield: 177 mg (53 %). Analysis calculated for $C_{42}H_{51}F_9N_8O_{15}S_3Yb_2$. Calcd.: C, 33.16; H, 3.38; N, 7.37; S, 6.32. Found: C, 33.66; H, 3.30; N, 7.25; S, 6.58. IR(ν=N): 1636 cm^{-1} (Figure S31). MALDI-MS positive mode: 1319.15 *m*/*z* $[Yb_2L(OTf)_2]^+$ (Figure S4).

Synthesis of 5·3H$_2$O. LuL·4H$_2$O (200 mg; 0.22 mmol), Gd(OTf)$_3$·9H$_2$O (500mg; 0.66 mmol), refluxed 3 hr. Yield: 179 mg (55 %). Analysis calculated for $C_{42}H_{51}F_9N_8O_{15}S_3LuGd$. Calcd.: C, 33.47; H, 3.41; N, 7.43; S, 6.38. Found: C, 33.51; H, 3.24; N, 7.20; S, 6.46. IR(ν=N): 1636 cm^{-1} (Figure S32). MALDI-MS positive mode: 1304.13 *m*/*z* $[LuGdL(OTf)_2]^+$ (Figure S5).

Synthesis of 6·3H$_2$O. LLu·4H$_2$O (201 mg; 0.22 mmol), Y(OTf)$_3$·9H$_2$O (457 mg; 0.66 mmol), refluxed 3 hr. Yield: 141 mg (45 %). Analysis calculated for $C_{42}H_{51}F_9N_8O_{15}S_3LuY$. Calcd.: C, 35.06; H, 3.57; N, 7.79; S, 6.68. Found: C, 35.37; H, 3.82; N, 7.58; S, 6.38. IR(ν=N): 1636 cm^{-1} (Figure S33). MALDI-MS positive mode: 1235.14 *m*/*z* $[LuYL(OTf)_2]^+$ (Figure S6). ^{1}H NMR (500 MHz, CD_3CN) δ/ppm 8.31 (s, 3H), 8.30 (s, 3H), 7.48 (s, 3H), 7.47 (s, 3H), 3.79 (m, 6H), 3.68 (m, 6H), 3.31 (m, 6H), 2.86 (m, 6H), and 2.31 (s, 9H) (Figure 2). ^{13}C NMR (125.74 MHz, CD_3CN) δ/ppm 172.6, 172.0, 159.5, 144.2, 143.8, 128.5, 124.34, 124.28, 62.0, 61.6, 61.03, 60.95, and 19.5 (Figure S50).

Synthesis of 7·2H$_2$O. LuL·4H$_2$O (200 mg; 0.22 mmol), Lu(OTf)$_3$·9H$_2$O (852 mg; 1.1 mmol), refluxed for 1 day. Yield: 140 mg (43 %). Analysis calculated for $C_{42}H_{49}F_9N_8O_{14}S_3Lu_2$. Calcd.: C, 33.47; H, 3.28; N, 7.44; S, 6.38. Found: C, 33.42; H, 3.43; N, 7.18; S, 6.57. IR(ν=N): 1637 cm^{-1} (Figure S34). MALDI-MS positive mode: 1321.19 *m*/*z* $[Lu_2L(OTf)_2]^+$ (Figure S7). ^{1}H NMR (500 MHz, CD_3CN) δ/ppm 8.30 (s, 6H), 7.48 (s, 6H), 3.79 (m, 6H), 3.68 (m, 6H), 3.31 (m, 6H), 2.86 (m, 6H), and 2.31 (s, 9H) (Figure S51). ^{13}C NMR (125.74 MHz, CD_3CN) δ/ppm 172.4, 159.5, 143.8, 128.6, 124.4, 62.0, 60.9, and 19.5 (Figure S52).

Synthesis of 8·3H$_2$O. YL·4H$_2$O (200 mg; 0.24 mmol), Gd(OTf)$_3$·9H$_2$O (552 mg; 0.72 mmol), refluxed 3 hr. Yield: 192 mg (56 %). Analysis calculated for $C_{42}H_{51}F_9N_8O_{15}S_3GdY$. Calcd.: C, 35.49; H, 3.62; N, 7.88; S, 6.77. Found: C, 35.54; H, 3.91; N, 7.68; S, 6.83. IR(ν=N): 1636 cm^{-1} (Figure S35). MALDI-MS positive mode: 1218.11 *m*/*z* $[YGdL(OTf)_2]^+$ (Figure S8).

Synthesis of 9·3H$_2$O. YL·4H$_2$O (200 mg; 0.24 mmol), Y(OTf)$_3$·9H$_2$O (552 mg; 0.72 mmol), refluxed 3 hr. Yield: 192 (57 %). Analysis calculated for $C_{42}H_{51}F_9N_8O_{15}S_3Y_2$. Calcd.: C, 37.29; H, 3.80; N, 8.28; S, 7.11. Found: C, 37.22; H, 4.45; N, 7.98; S, 7.39. IR(ν=N): 1637 cm^{-1} (Figure S36). MALDI-MS positive mode: 1149.10 *m*/*z* $[Y_2L(OTf)_2]^+$ (Figure S9). ^{1}H NMR (500 MHz, CD_3CN) δ/ppm 8.31 (s, 6H), 7.47 (s, 6H), 3.80 (m, 6H), 3.70 (m, 6H), 3.32 (m, 6H), 2.86 (m, 6H), and 2.30 (s, 9H) (Figure S53). ^{13}C NMR (125.74 MHz, CD_3CN) δ/ppm 172.1, 159.4, 144.3, 128.4, 124.3, 61.7, 61.1, and 19.5 (Figure S54).

Synthesis of 10·3H$_2$O. To a suspension of GdL* (210 mg; 0.28 mmol) in pyridine (60 ml) Gd(OTf)$_3$·9H$_2$O (654 mg; 0.85 mmol) is added. The solution is heated to boiling and tren (42 mg; 0.29 mmol) in pyridine (5 ml) is added dropwise. The red solution is then refluxed for 3 hours. After being cooled to room temperature the solution is poured into 300 ml vigorously stirred diethyl ether (300 ml) yielding an orange precipitate. This is isolated and washed twice with diethyl ether (2x100 ml) and dried. The product is extracted with dichloromethane (100 ml). The orange dichloromethane solution is then filtered and evaporated to dryness. To the orange precipitate is added THF (25 ml) and the suspension is stirred overnight forming a pale yellow precipitate. This is isolated and washed with 3x15 ml tetrahydrofuran and 2x10 ml diethyl ether. Yield: 143 mg (34 %). Analysis calculated for $C_{42}H_{51}F_9N_8O_{15}S_3Gd_2$. Calcd.: C, 33.87; H, 3.45; N, 7.52; S, 6.46. Found: C, 33.73; H, 3.12; N, 7.26; S, 6.60. IR(ν=N): 1632 cm^{-1} (Figure S37). MALDI-MS positive mode: 1287.12 *m*/*z* $[Gd_2L(OTf)_2]^+$ (Figure S10).

Synthesis of 1$_N$ - 10$_N$. The nitrate analogs of **1 - 10** (**1$_N$ - 10$_N$**) were obtained through a recrystallization of **1 - 10**.

Synthesis of 1$_N$·EtOH·3H$_2$O. To an ethanol (1 ml) solution of **1·3H$_2$O** (100 mg; 66 μmol) is added another ethanol (1 ml) solution of Bu_4NNO_3 (102 mg; 335 μmol). The final solution is stirred and left for one hour to initiate the precipitation. After one hour the solution is stirred and left for another hour. The precipitate is isolated and washed with 3x2ml ethanol, 2x2ml acetone and 2x1 ml diethyl ether. Yield: 54 mg (63 %). Analysis calculated for $C_{41}H_{57}N_{11}O_{16}YbGd$. Calcd.: C, 38.17; H, 4.45; N, 11,94. Found: C, 38.46; H, 4.46; N, 11.22. IR(ν=N): 1637 cm^{-1} (Figure S38). MALDI-MS positive mode: 1127.20 *m*/*z* $[YbGdL(NO_3)_2]^+$ (Figure S11).

Synthesis of 2$_N$·EtOH·3H$_2$O. Bu_4NNO_3 (86 mg; 0.28 mmol) and **2·2H$_2$O** (80 mg; 56 μmol). Yield: 41 mg (60 %). Analysis calculated for $C_{41}H_{57}N_{11}O_{16}YbY$. Calcd.: C, 40.30; H, 4.70; N, 12.61. Found: C, 40.20; H, 4.59; N, 12.10. IR(ν=N): 1636 cm^{-1} (Figure S39). MALDI-MS positive mode: 1060.18 *m*/*z* $[YbYL(NO_3)_2]^+$ (Figure S12).

Synthesis of 3$_N$·EtOH·3H$_2$O. Bu_4NNO_3 (33 mg; 108 μmol), **3·3H$_2$O** (30 mg; 20 μmol). Yield: 17 mg (66 %). Analysis calculated for $C_{41}H_{57}N_{11}O_{16}YbLu$. Calcd.: C, 37.65; H, 4.39; N, 11.78. Found: C, 37.57; H, 4.26; N, 11.59. IR(ν=N): 1636 cm^{-1} (Figure S40). MALDI-MS positive mode: 1146.22 *m*/*z* $[LuYbL(NO_3)_2]^+$ (Figure S13).

Synthesis of 4$_N$·EtOH·2H$_2$O. Bu_4NNO_3 (75 mg; 0.25 mmol), **4·3H$_2$O** (72 mg; 47 μmol). Yield: 39 mg (64 %). Analysis calculated for $C_{41}H_{57}N_{11}O_{15}Yb_2$. Calcd.: C, 38.23; H, 4.30; N, 11.96. Found: C, 37.79; H, 4.29; N, 11.67. IR(ν=N): 1636 cm^{-1} (Figure S41). MALDI-MS positive mode: 1143.21 *m*/*z* $[Yb_2L(NO_3)_2]^+$ (Figure S14).

Synthesis of 5$_N$·EtOH·3H$_2$O. Bu_4NNO_3 (94 mg; 309 μmol), **5·3H$_2$O** (92 mg; 62 μmol). Yield: 45 mg (57 %). Analysis calculated for $C_{41}H_{57}N_{11}O_{16}LuGd$. Calcd.: C, 38.11; H, 4.45; N, 11.92. Found: C, 37.83; H, 4.13; N, 11.47. IR(ν=N): 1637 cm^{-1} (Figure S42). MALDI-MS positive mode: 1130.21 *m*/*z* $[LuGdL(NO_3)_2]^+$ (Figure S15).

Synthesis of 6$_N$·EtOH·3.5H$_2$O Bu_4NNO_3 (65 mg; 0.21 mmol) and **6·3H$_2$O** (60 mg; 42 μmol). Yield: 28 mg (54 %). Analysis calculated for $C_{41}H_{58}N_{11}O_{16.5}LuY$. Calcd.: C, 39.94; H, 4.74; N, 12.50. Found: C, 39.42; H, 4.49; N, 12.15. IR(ν=N): 1635 cm^{-1} (Figure S43). MALDI-MS positive mode: 1162.26 *m*/*z* $[LuYL(NO_3)_2]^+$ (Figure S16). ^{1}H NMR (500 MHz, D_2O) δ/ppm 8.39 (s, 6H), 7.56 (s, 3H), 7.54 (s, 3H), 3.88 (m, 6H), 3.76 (m, 6H), 3.34 (m, 6H), 2.93 (m, 6H), and 2.32 (s, 9H) (Figure S60).

Synthesis of 7$_N$·EtOH·4H$_2$O. Bu_4NNO_3 (100 mg; 382 μmol) and **6·2H$_2$O** (100 mg; 66 μmol). Yield: 59 mg (67 %). Analysis calculated for $C_{41}H_{59}N_{11}O_{17}Lu_2$. Calcd.: C, 37.08; H, 4.48; N, 11.60. Found: C, 36.63; H, 4.09; N, 11.33. IR(ν=N): 1637 cm^{-1} (Figure S44). MALDI-MS positive mode: 1147.22 *m*/*z*

$[Lu_2L(NO_3)_2]^+$ (Figure S17). ^{1}H NMR (500 MHz, D_2O) δ/ppm 8.39 (s, 6H), 7.55 (s, 6H), 3.87 (m, 6H), 3.76 (m, 6H), 3.35 (m, 6H), 2.91 (m, 6H), and 2.32 (s, 9H) (Figure S61).

Synthesis of $\mathbf{8_N \cdot EtOH \cdot 3H_2O}$. Bu_4NO_3 (88 mg; 0.29 mmol) and **$\mathbf{8 \cdot 3H_2O}$** (81 mg; 57 µmol). Yield: 47 mg (68 %). Analysis calculated for $C_{41}H_{57}N_{11}O_{16}YGd$. Calcd.: C, 40.83; H, 4.76; N, 12.77. Found: C, 40.66; H, 4.41; N, 12.41. IR(ν=N): 1636 cm^{-1} (Figure S45). MALDI-MS positive mode: 1044.17 *m*/*z* $[YGdL(NO_3)_2]^+$ (Figure S18).

Synthesis of $\mathbf{9_N \cdot EtOH \cdot 3H_2O}$ Bu_4NNO_3 (114 mg; 374 µmol) and **$\mathbf{10 \cdot 3H_2O}$** (100 mg; 74 µmol). Yield: 55.4 mg (66 %). Analysis calculated for $C_{41}H_{57}N_{11}O_{16}Y_2$. Calcd.: C, 43.28; H, 5.05; N, 13.54. Found: C, 43.79; H, 4.84; N, 12.87. IR(ν=N): 1636 cm^{-1} (Figure S46). MALDI-MS positive mode: 975.15 m/z $[Y_2L(NO_3)_2]^+$ (Figure S19). ^{1}H NMR (500 MHz, D_2O) δ/ppm 8.40 (s, 6H), 7.55 (s, 6H), 3.89 (m, 6H), 3.78 (m, 6H), 3.35 (m, 6H), 2.94 (m, 6H), and 2.32 (s, 9H) (Figure S62).

Synthesis of $\mathbf{10_N \cdot EtOH \cdot 3H_2O}$ Bu_4NNO_3 (81 mg; 0.27 mmol) and **$\mathbf{10 \cdot 3H_2O}$** (80 mg; 54 µmol). Yield: 33 mg (48 %). Analysis calculated for $C_{41}H_{57}N_{11}O_{16}Gd_2$. Calcd.: C, 38.64; H, 4.51; N, 12.09. Found: C, 38.06; H, 3.94; N, 11.91. IR(ν=N): 1634 cm^{-1} (Figure S47). MALDI-MS positive mode: 1113.21 *m*/*z* $[Gd_2L(NO_3)_2]^+$ (Figure S20).

Synthesis of $\mathbf{YL \cdot 4H_2O}$ and $\mathbf{LuL \cdot 4H_2O}$. The complexes $YL \cdot 4H_2O$ and $LuL \cdot 4H_2O$ were synthesised using a similar procedure to one employed for $YbL \cdot 4H_2O$.

Synthesis of $\mathbf{YL \cdot 4H_2O}$. dfmp (2.51 g; 15 mmol) and $Y(OTf)_3 \cdot 9H_2O$ (3.58 g; 5 mmol) are dissolved in hot acetonitrile (300 ml). To this a solution of tris(2-aminoethyl)amine (tren, 1.50 g; 10 mmol) in methanol (25 ml) is added dropwise during 30 min. The resulting orange solution is boiled for 10 min and then triethylamine (2.5 ml; 18 mmol) is added to the boiling solution, which is quickly removed from the heat. During a few hours a yellow precipitate forms, which is isolated and washed with ethanol and diethyl ether. Yield: 2.79 g (66 %). Anal. Calcd for $C_{39}H_{53}N_8O_7Y$: C, 56.11; H, 6.40; N, 13.42. Found: C, 55.81; H, 5.89; N, 13.59. IR(ν=N): 1619 and 1599 cm^{-1} (Figure S48). MALDI-MS positive mode 763.28 *m*/*z* $[YLH]^+$ (Figure S26).

Synthesis of $\mathbf{LuL \cdot 4H_2O}$. The Synthesis of $LuL \cdot 4H_2O$ was performed analogously to $YL \cdot 4H_2O$. dfmp (1.88 g; 11 mmol), $Lu(OTf)_3 \cdot 9H_2O$ (3.00 g; 3.8 mmol), tren (1.13 g; 7.7 mmol) and triethylamine (1.6 ml; 12 mmol). Yield: 2.58 (73 %). Anal. Calcd for $C_{39}H_{53}N_8O_7Lu$: C, 50.87; H, 5.80; N, 12.17. Found: C, 50.87; H, 5.36; N, 11.87. IR(ν=N): 1618 and 1600 cm^{-1} (Figure S49). MALDI-MS positive mode 849.31 *m*/*z* (Figure S27).

Synthesis of $\mathbf{YbL \cdot 4H_2O}$ and of GdL*. $YbL \cdot 4H_2O$ and GdL* were synthesized according to literature.[10, 11]

$\mathbf{2_N}$' and **$\mathbf{3_N}$'** are dilute samples of **$\mathbf{2_N}$** and **$\mathbf{3_N}$** in a host of **$\mathbf{9_N}$**. The powders were prepared similarly to the synthesis of **$\mathbf{9_N}$**, by employing a 3:97 molar ratio of (**$\mathbf{2_N}$**, **$\mathbf{3_N}$**) and **$\mathbf{9_N}$**.

Mass spectrometry

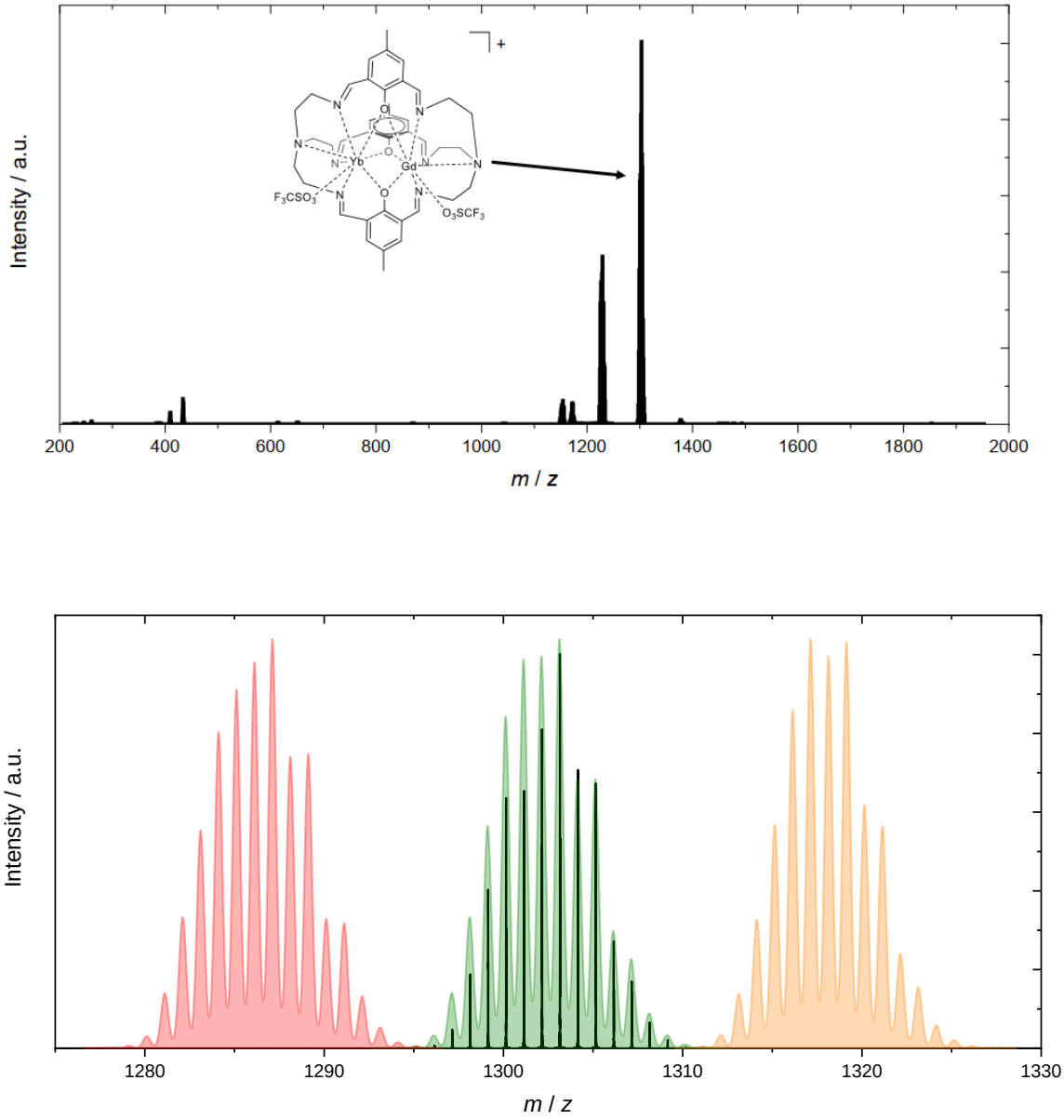

Figure S1. MALDI positive mode mass spectrum of **1** (top) with enlargement of the region of the molecular ion (bottom). Color code: signal (black), predicted isotope pattern for $[YbGdL(OTf)_2]^+$ (green), predicted isotope pattern for $[Gd_2L(OTf)_2]^+$ (red) and predicted isotope pattern for $[Yb_2L(OTf)_2]^+$ (orange).

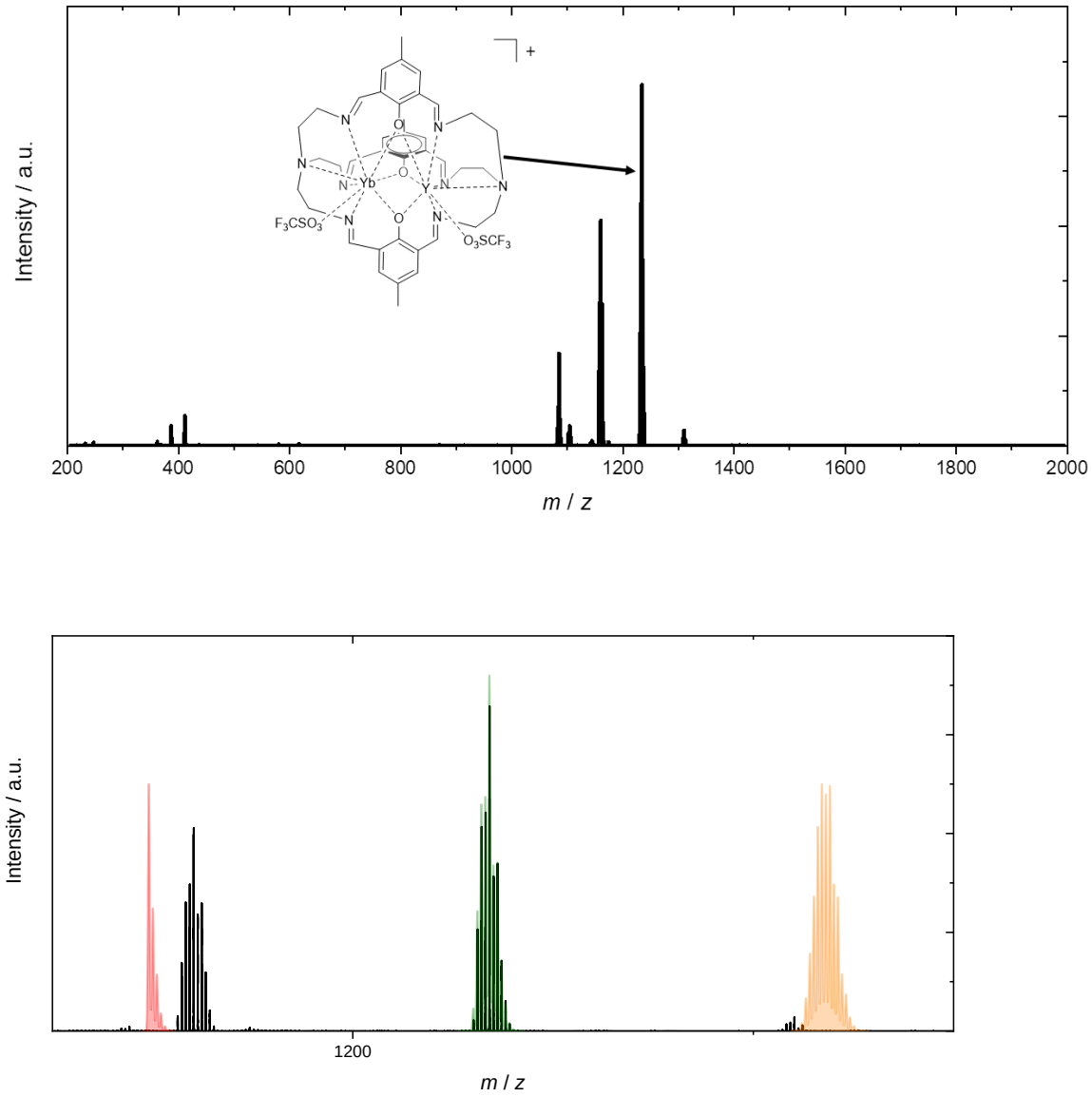

Figure S2. MALDI positive mode mass spectrum of **2** (top) with enlargement of the region of the molecular ion (bottom). Color code: signal (black), predicted isotope pattern for $[YbYL(OTf)_2]^+$ (green), predicted isotope pattern for $[Y_2L(OTf)_2]^+$ (red) and predicted isotope pattern for $[Yb_2L(OTf)_2]^+$ (orange).

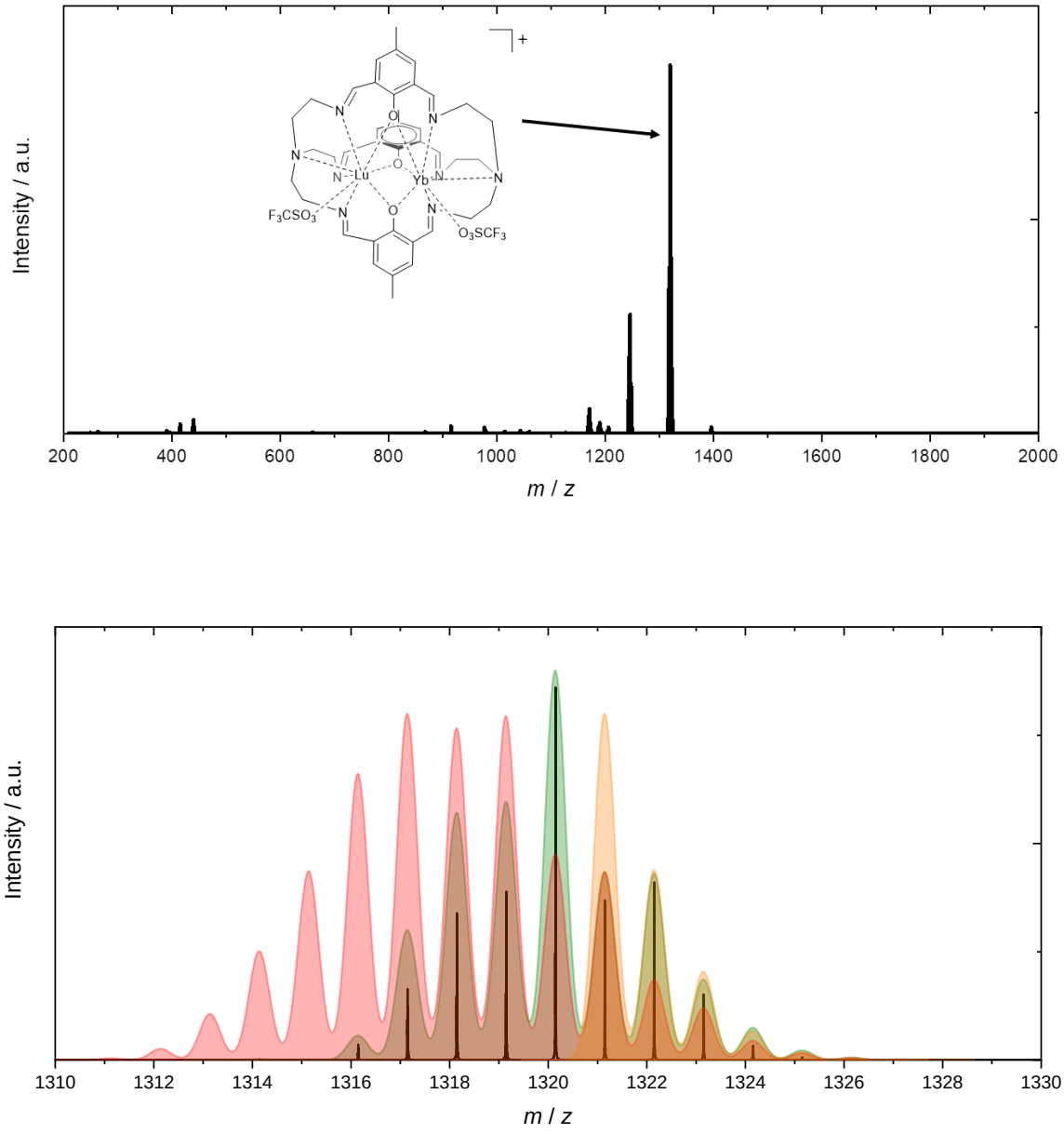

Figure S3. MALDI positive mode mass spectrum of **3** (top) with enlargement of the region of the molecular ion (bottom). Color code: signal (black), predicted isotope pattern for $[LuYbL(OTf)_2]^+$ (green), predicted isotope pattern for $[Yb_2L(OTf)_2]^+$ (red) and predicted isotope pattern for $[Lu_2L(OTf)_2]^+$ (orange).

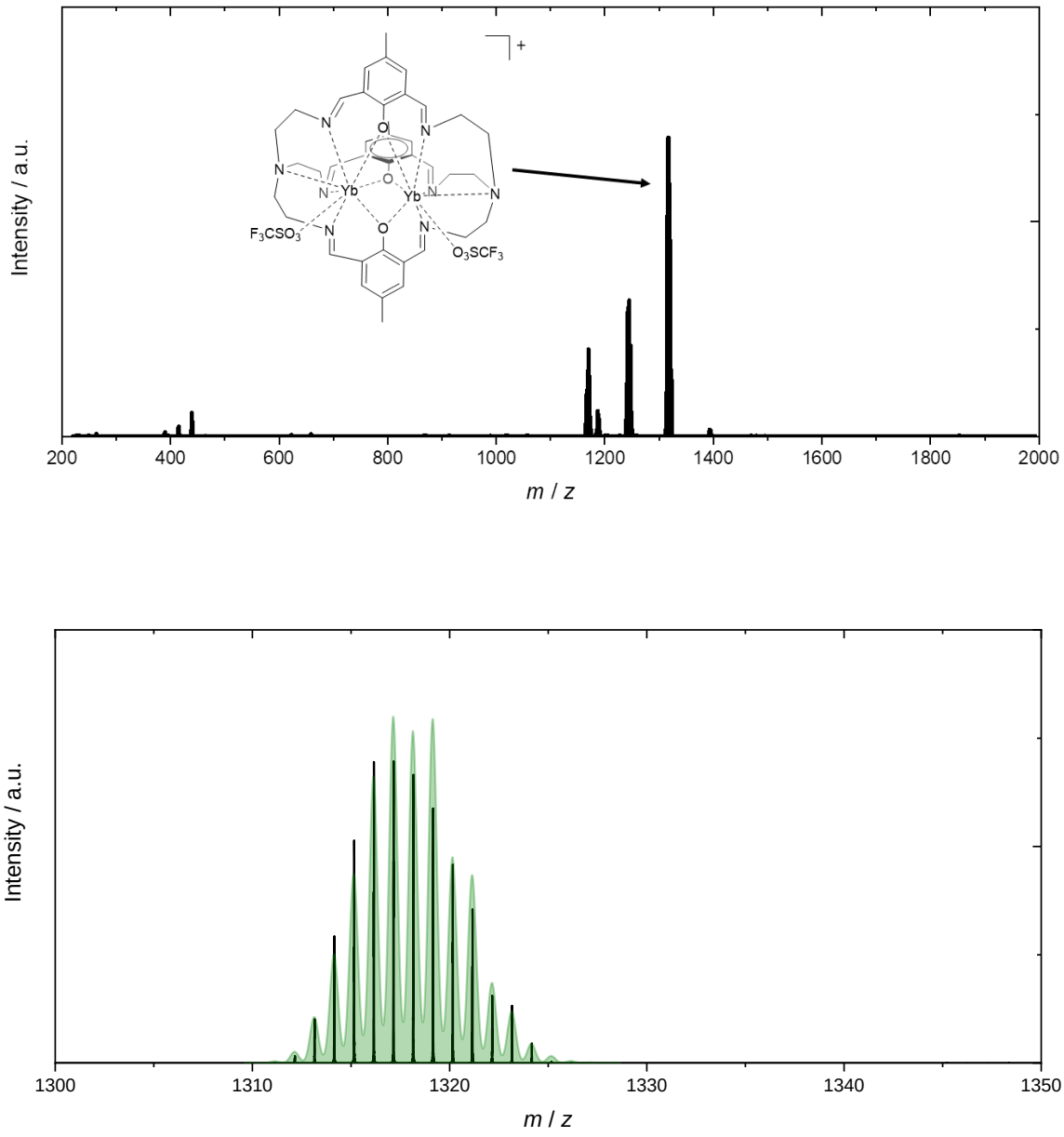

Figure S4. MALDI positive mode mass spectrum of **4** (top) with enlargement of the region of the molecular ion (bottom). Color code: signal (black) and predicted isotope pattern for $[Yb_2L(OTf)_2]^+$ (green).

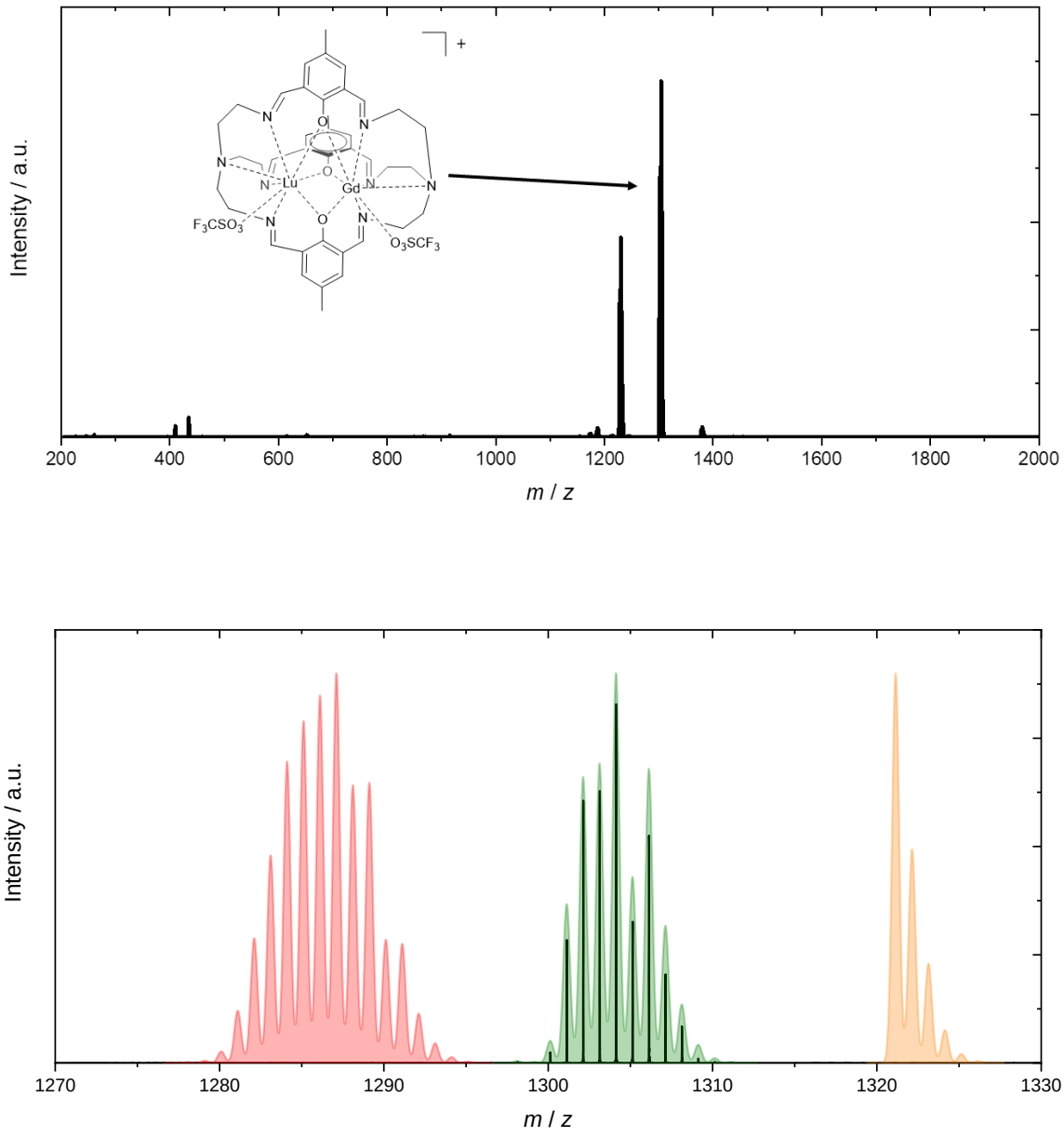

Figure S5. MALDI positive mode mass spectrum of **5** (top) with enlargement of the region of the molecular ion (bottom). Color code: signal (black), predicted isotope pattern for $[LuGdL(OTf)_2]^+$ (green), predicted isotope pattern for $[Gd_2L(OTf)_2]^+$ (red) and predicted isotope pattern for $[Lu_2L(OTf)_2]^+$ (orange).

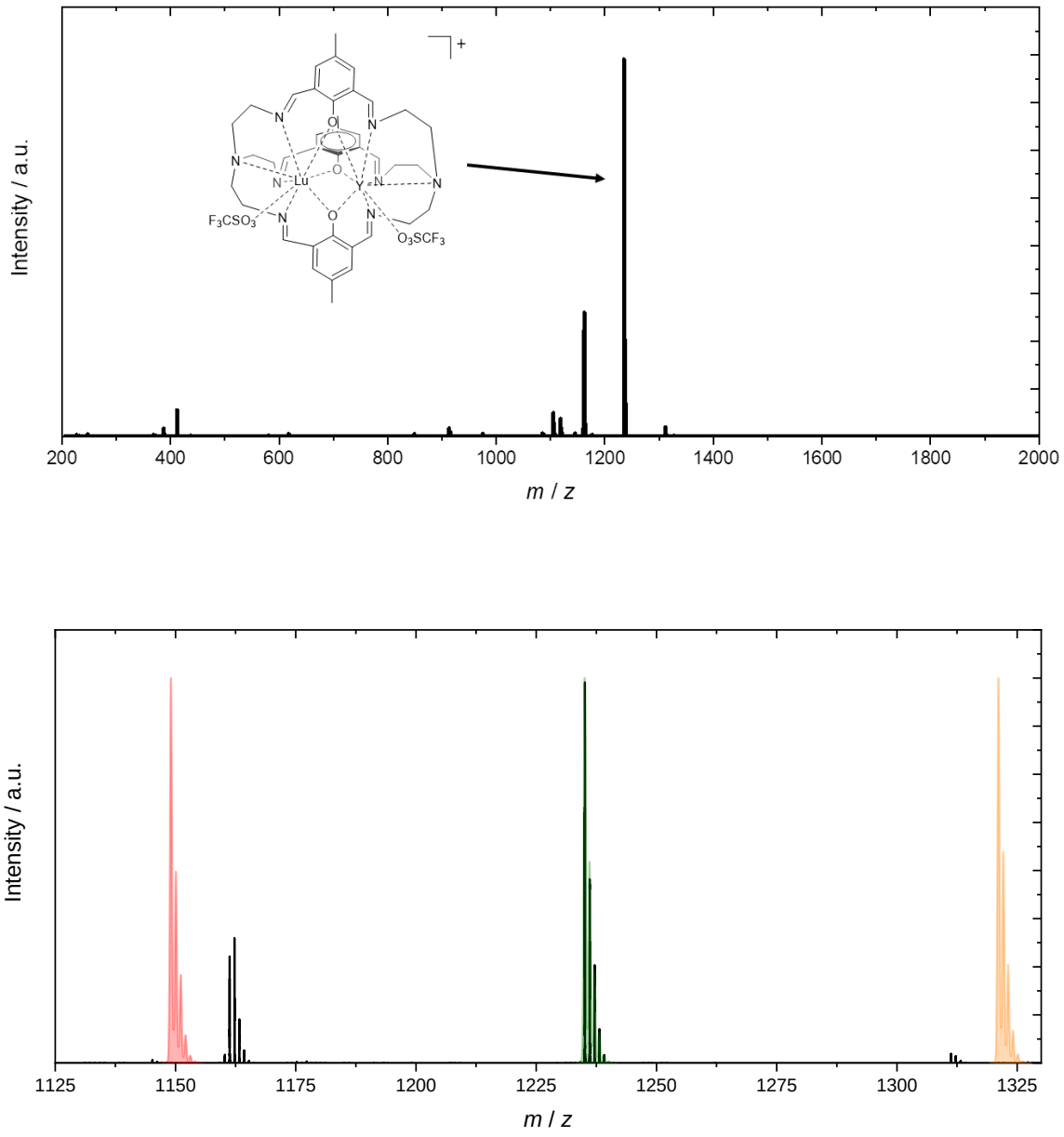

Figure S6. MALDI positive mode mass spectrum of **6** (top) with enlargement of the region of the molecular ion (bottom). Color code: signal (black), predicted isotope pattern for $[LuYL(OTf)_2]^+$ (green), predicted isotope pattern for $[Y_2L(OTf)_2]^+$ (red) and predicted isotope pattern for $[Lu_2L(OTf)_2]^+$ (orange).

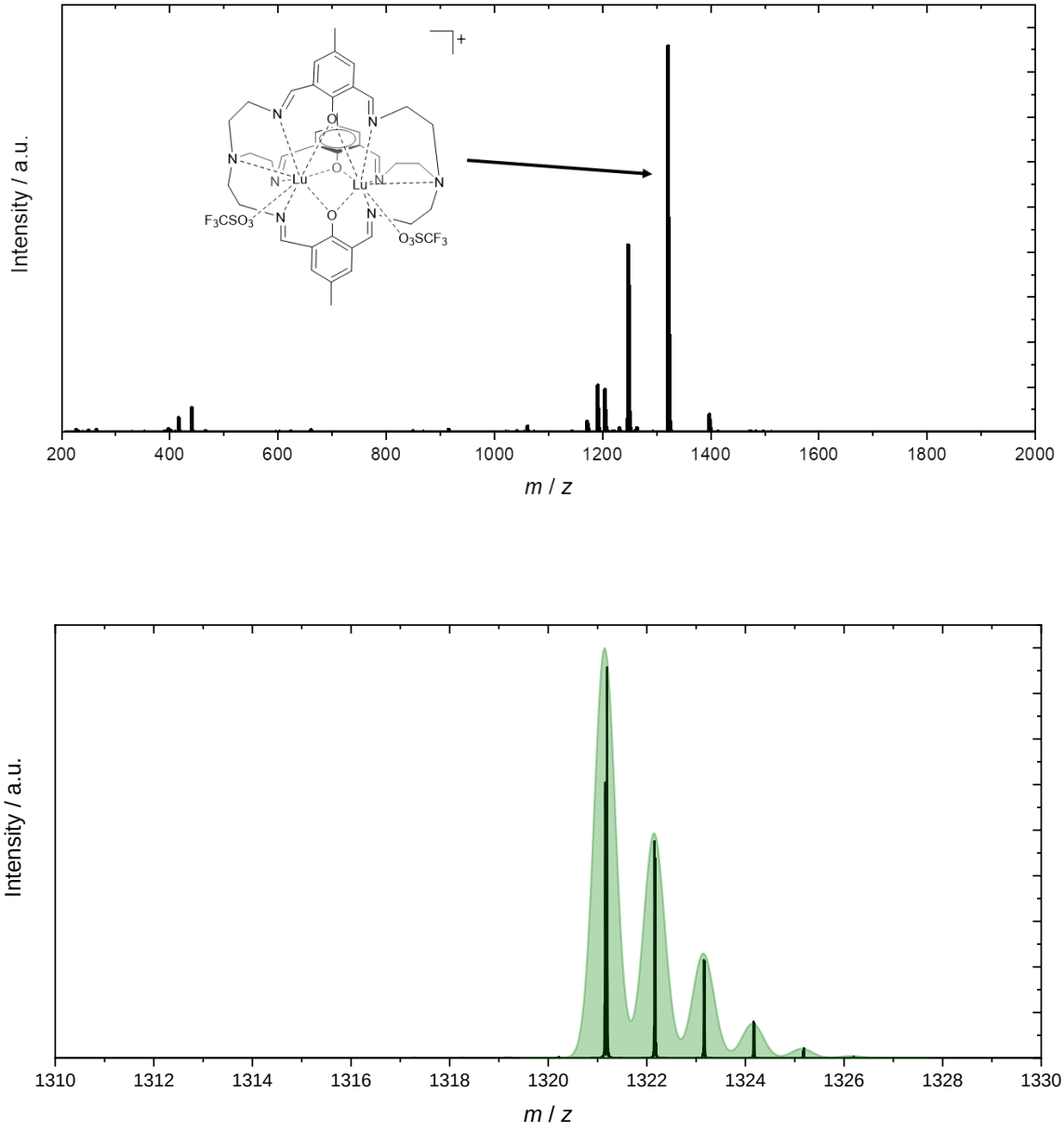

Figure S7. MALDI positive mode mass spectrum of **7** (top) with enlargement of the region of the molecular ion (bottom). Color code: signal (black) and predicted isotope pattern for $[Lu_2L(OTf)_2]^+$ (green).

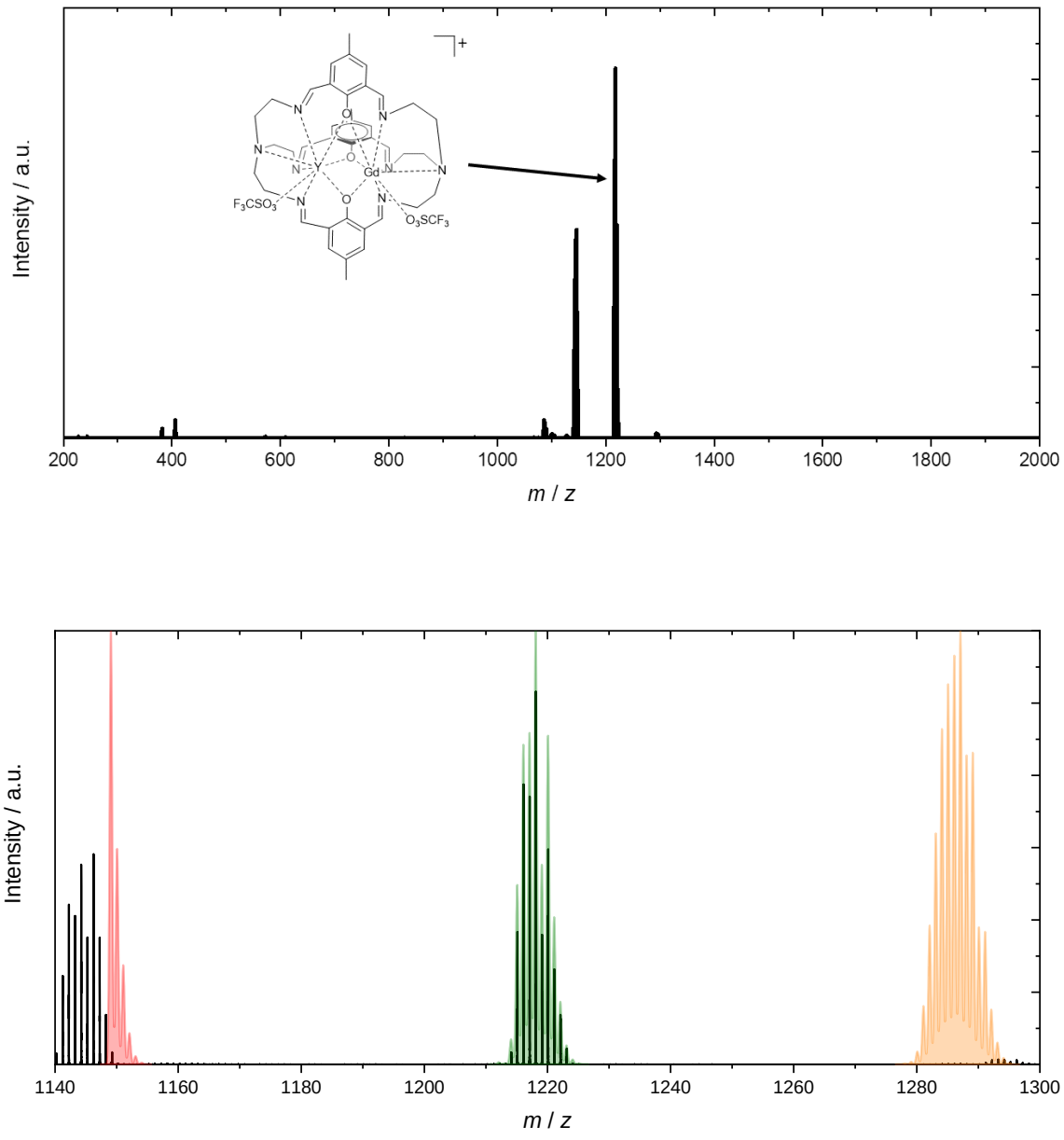

Figure S8. MALDI positive mode mass spectrum of **8** (top) with enlargement of the region of the molecular ion (bottom). Color code: signal (black), predicted isotope pattern for $[YGdL(OTf)_2]^+$ (green), predicted isotope pattern for $[Y_2L(OTf)_2]^+$ (red) and predicted isotope pattern for $[Gd_2L(OTf)_2]^+$ (orange).

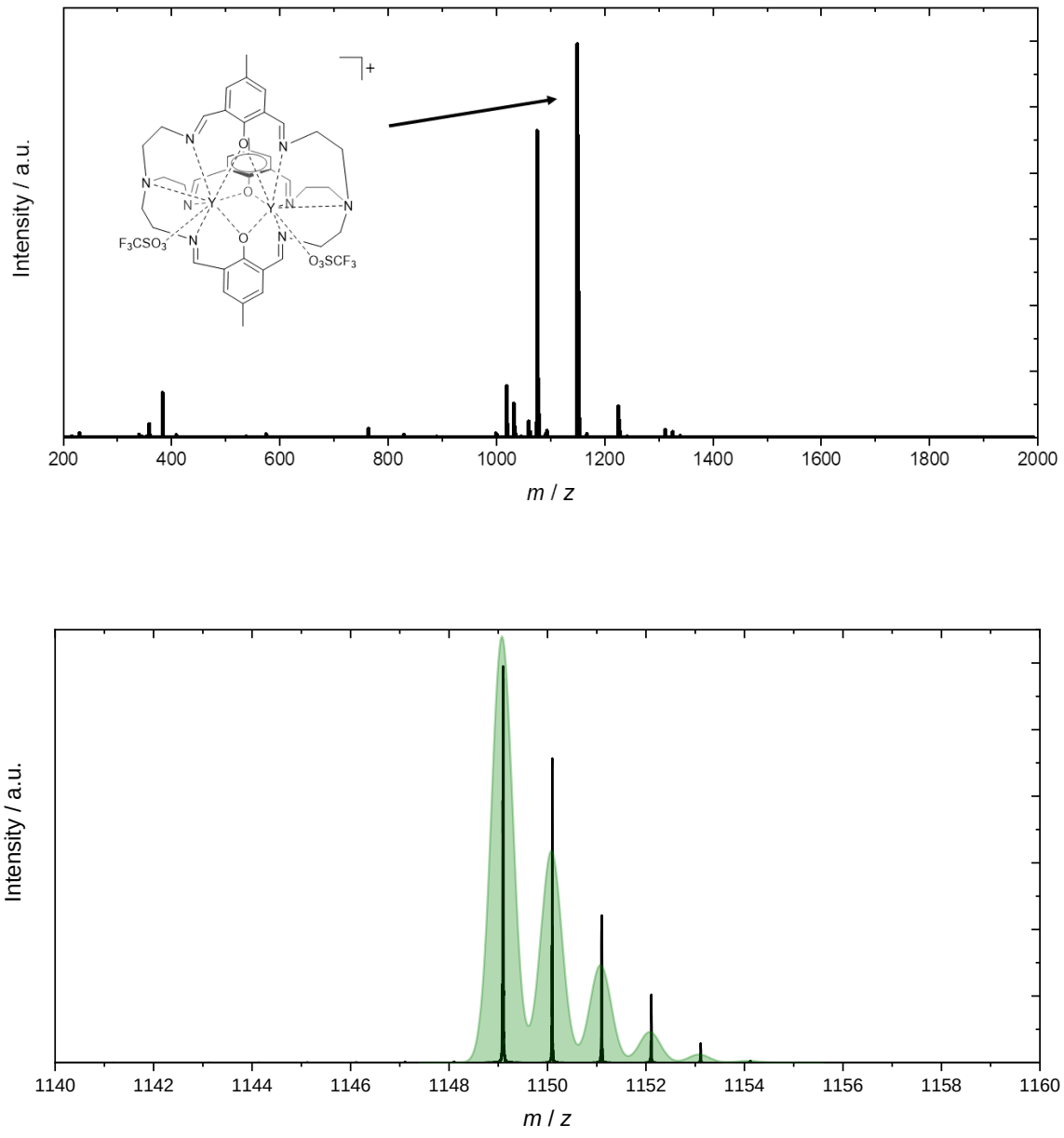

Figure S9. MALDI positive mode mass spectrum of **9** (top) with enlargement of the region of the molecular ion (bottom). Color code: signal (black) and predicted isotope pattern for $[Y_2L(OTf)_2]^+$ (green).

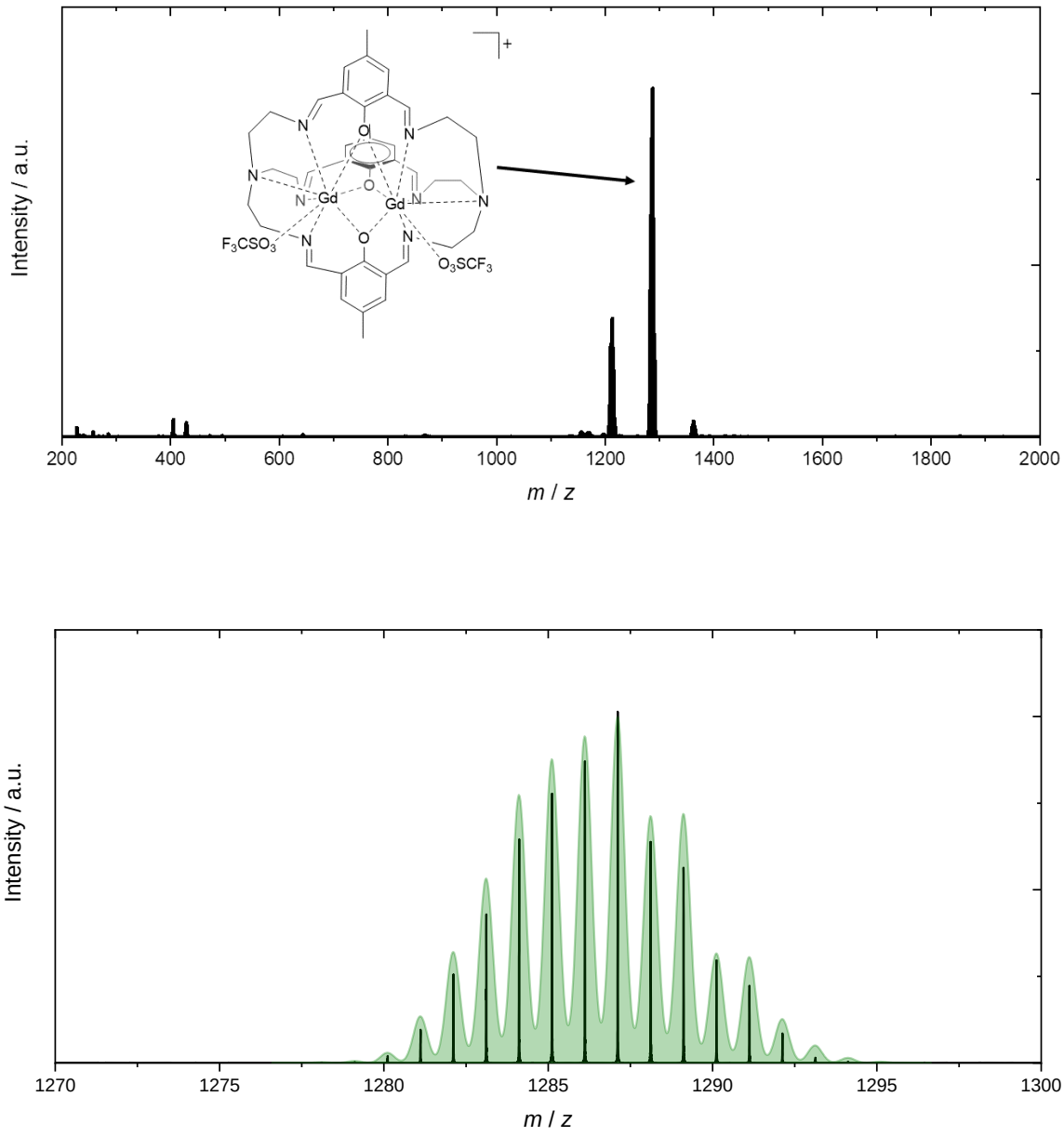

Figure S10. MALDI positive mode mass spectrum of **10** (top) with enlargement of the region of the molecular ion (bottom). Color code: signal (black) and predicted isotope pattern for $[Gd_2L(OTf)_2]^+$ (green).

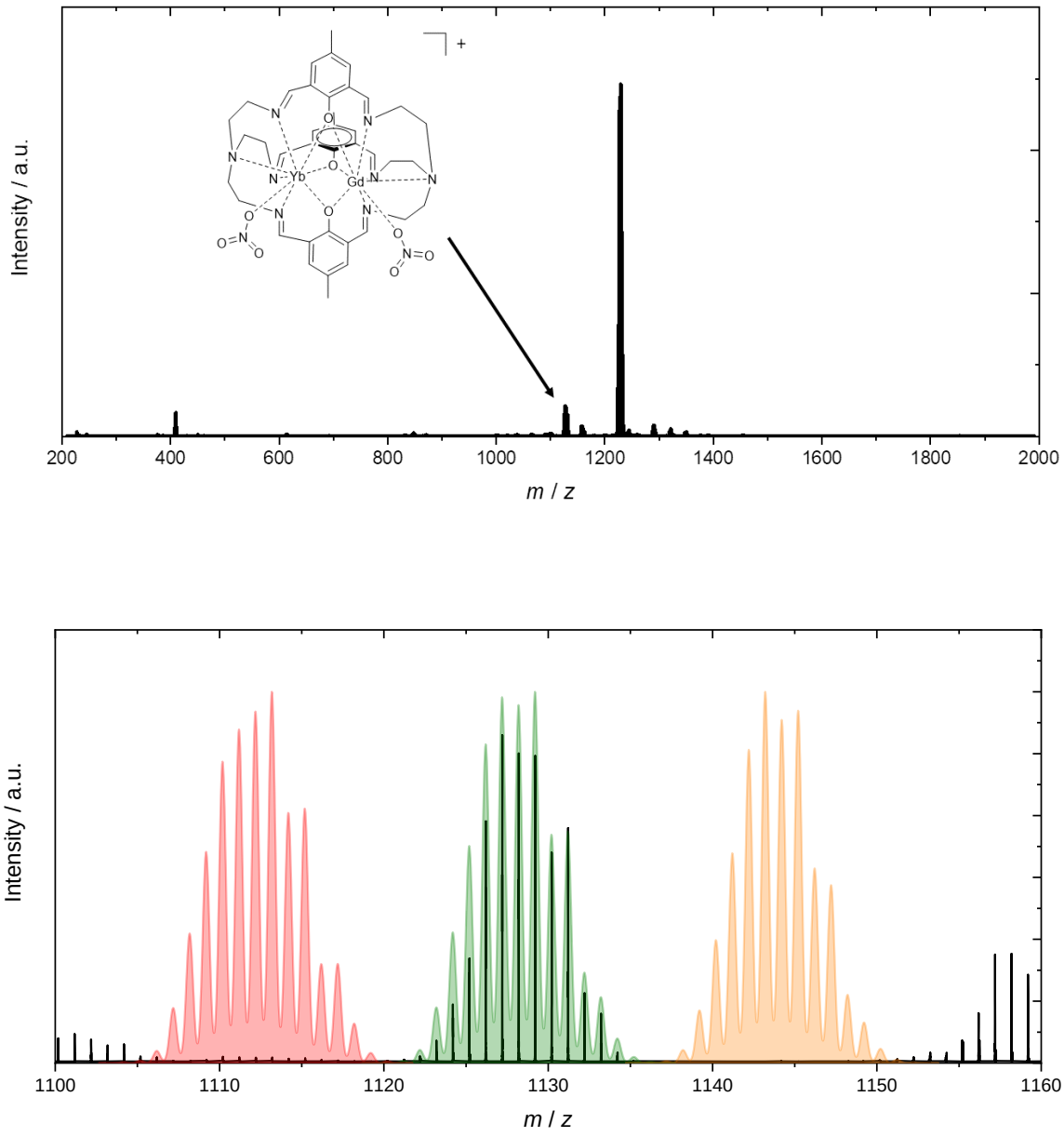

Figure S11. MALDI positive mode mass spectrum of $\mathbf{1_N}$ (top) with enlargement of the region of the molecular ion (bottom). Color code: signal (black), predicted isotope pattern for $[YbGdL(NO_3)_2]^+$ (green), predicted isotope pattern for $[Gd_2L(NO_3)_2]^+$ (red) and predicted isotope pattern for $[Yb_2L(NO_3)_2]^+$ (orange).

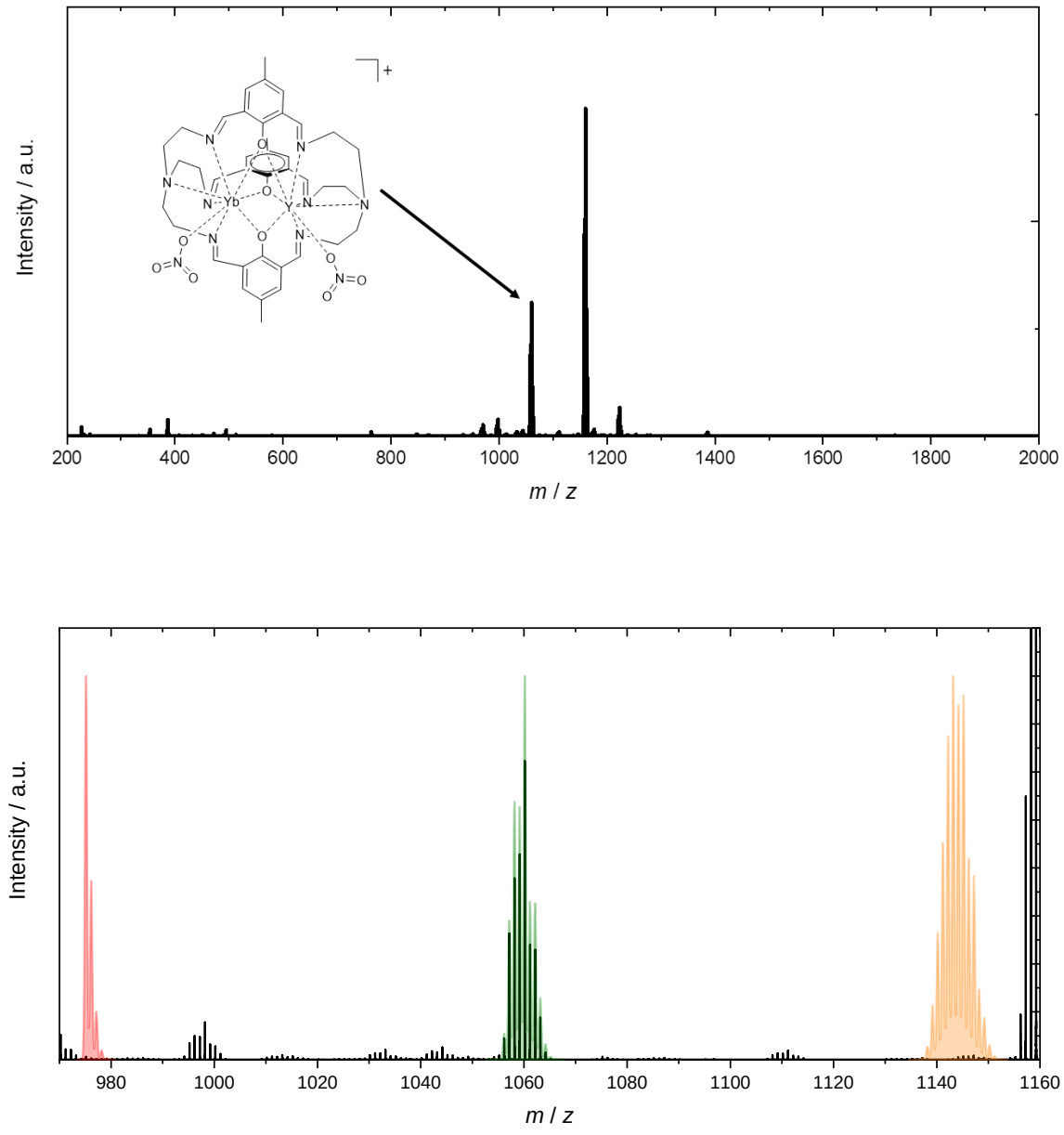

Figure S12. MALDI positive mode mass spectrum of $\mathbf{2_N}$ (top) with enlargement of the region of the molecular ion (bottom). Color code: signal (black), predicted isotope pattern for $[YbYL(NO_3)_2]^+$ (green), predicted isotope pattern for $[Y_2L(NO_3)_2]^+$ (red) and predicted isotope pattern for $[Yb_2L(NO_3)_2]^+$ (orange).

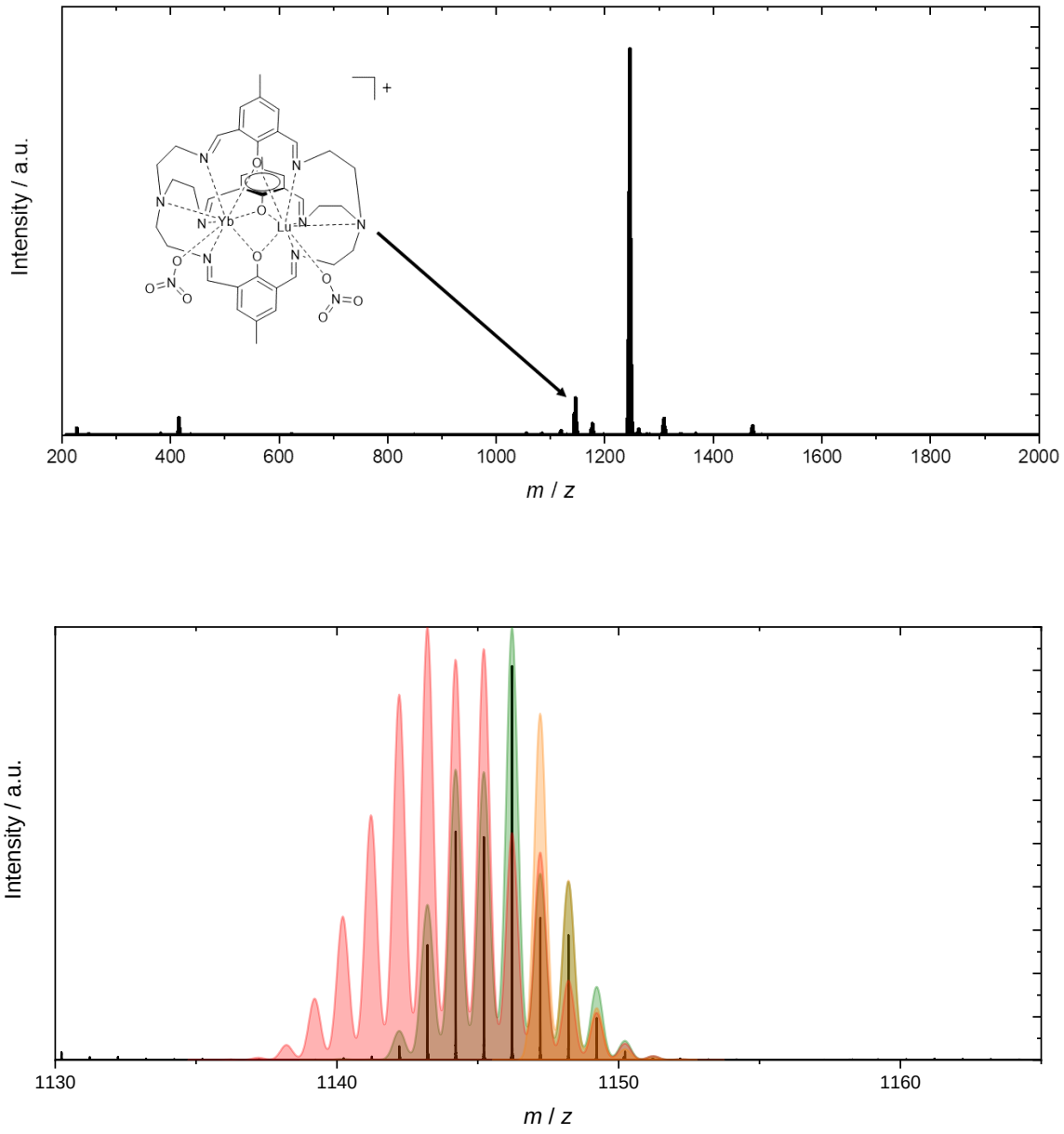

Figure S13. MALDI positive mode mass spectrum of $\mathbf{3_N}$ (top) with enlargement of the region of the molecular ion (bottom). Color code: signal (black), predicted isotope pattern for $[LuYbL(NO_3)_2]^+$ (green), predicted isotope pattern for $[Yb_2L(NO_3)_2]^+$ (red) and predicted isotope pattern for $[Lu_2L(NO_3)_2]^+$ (orange).

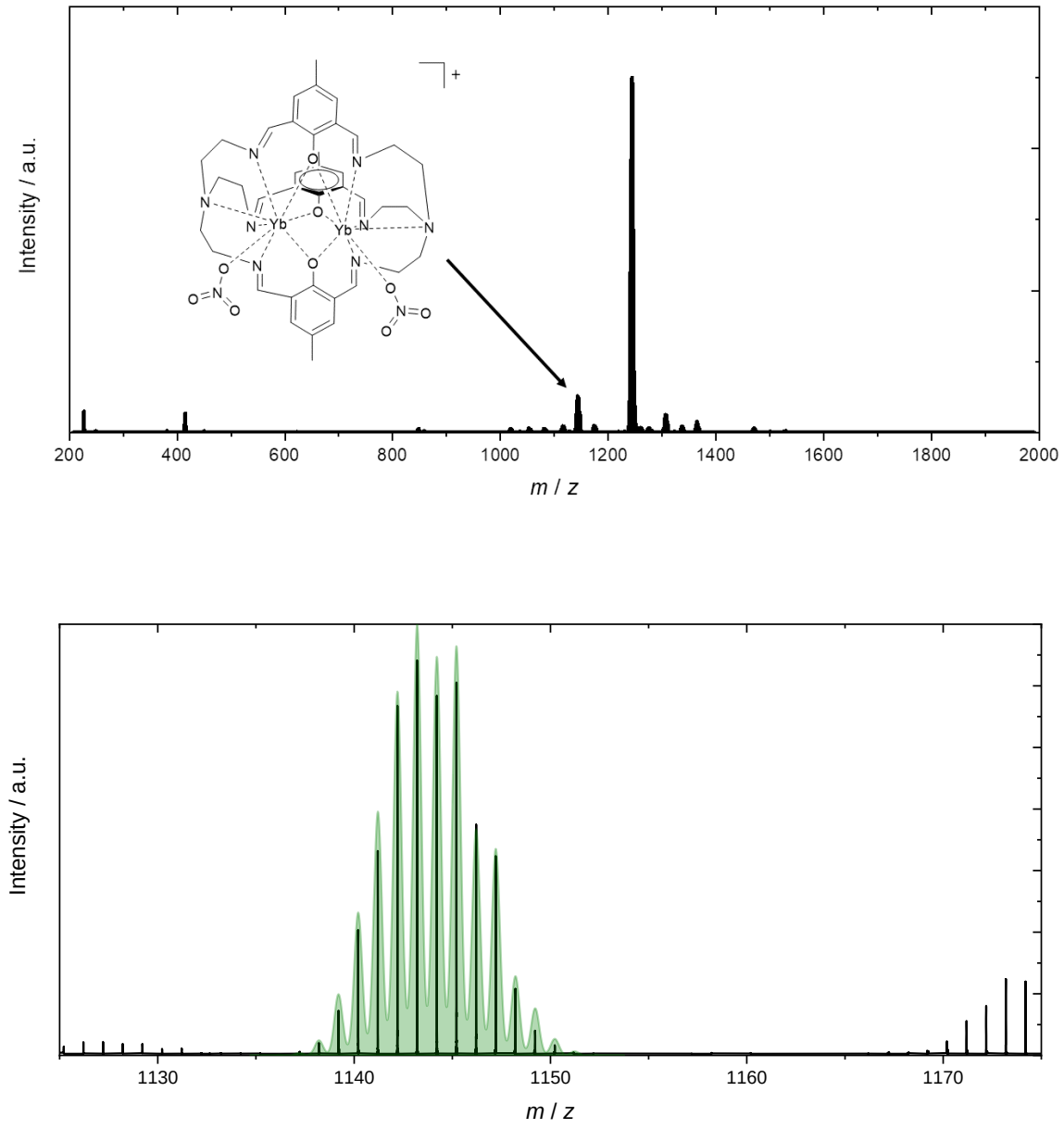

Figure S14. MALDI positive mode mass spectrum of $\mathbf{4_N}$ (top) with enlargement of the region of the molecular ion (bottom). Color code: signal (black) and predicted isotope pattern for $[Yb_2L(NO_3)_2]^+$ (green).

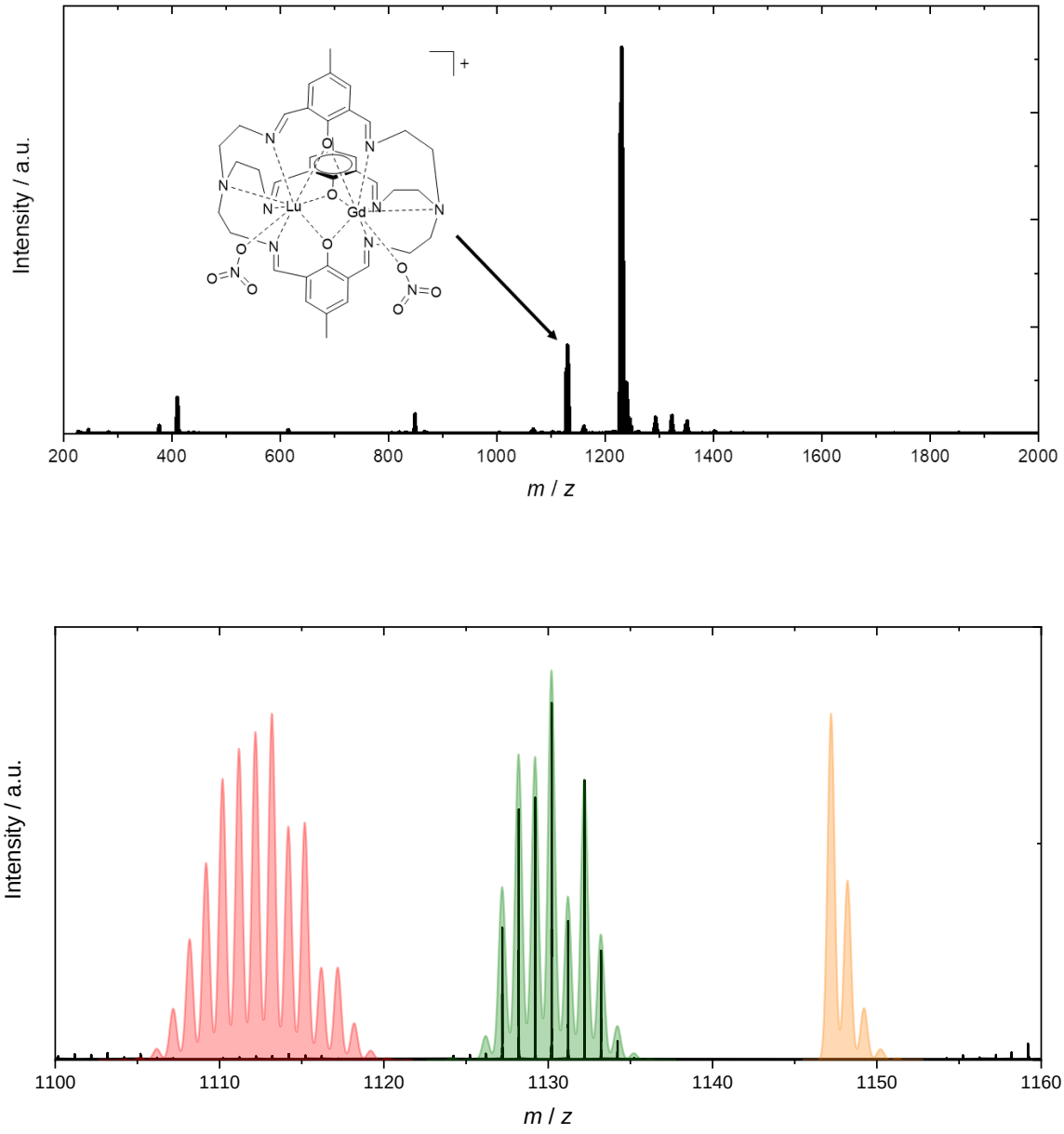

Figure S15. MALDI positive mode mass spectrum of $\mathbf{5_N}$ (top) with enlargement of the region of the molecular ion (bottom). Color code: signal (black), predicted isotope pattern for $[LuGdL(NO_3)_2]^+$ (green), predicted isotope pattern for $[Gd_2L(NO_3)_2]^+$ (red) and predicted isotope pattern for $[Lu_2L(NO_3)_2]^+$ (orange).

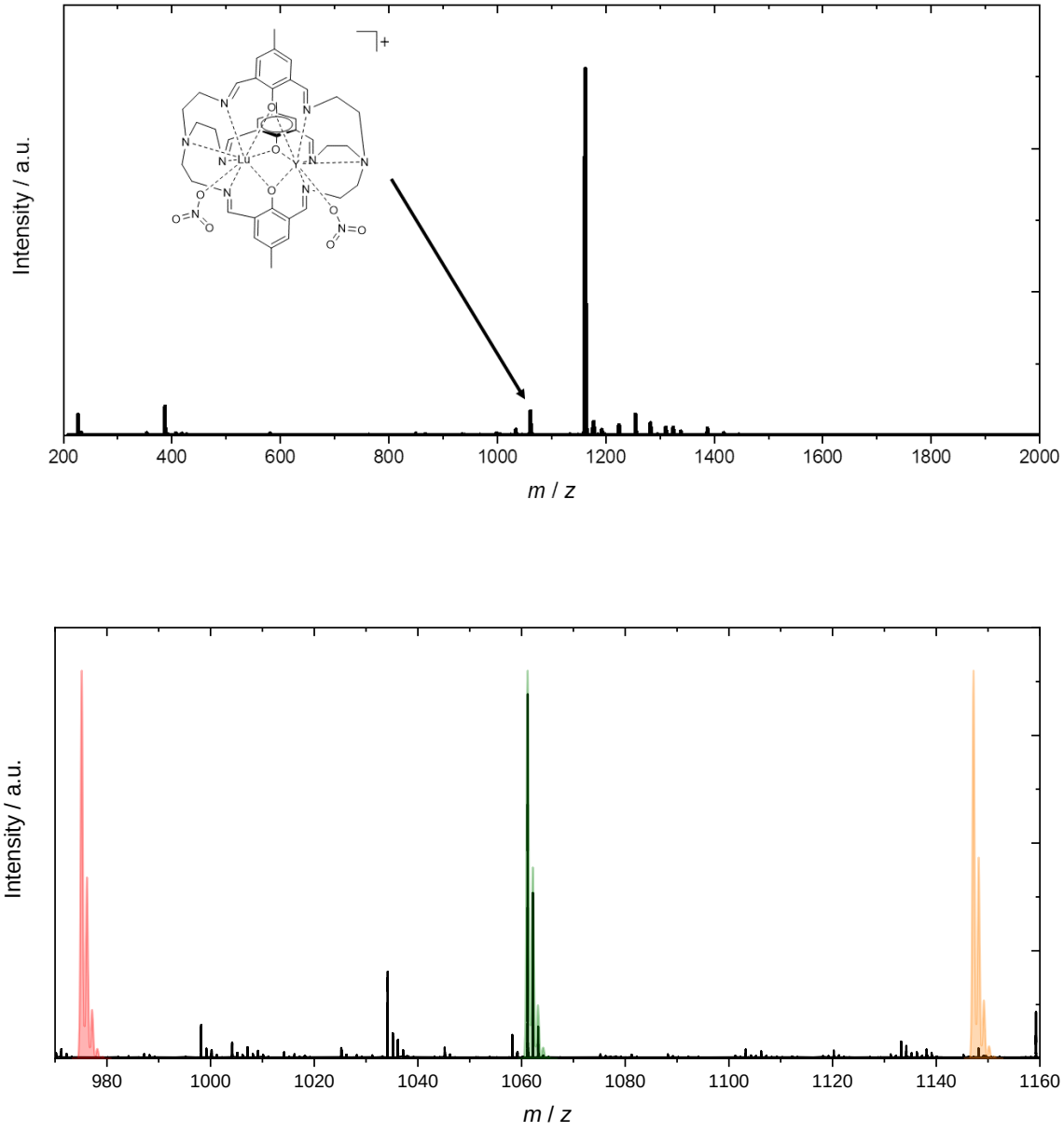

Figure S16. MALDI positive mode mass spectrum of $\mathbf{6_N}$ (top) with enlargement of the region of the molecular ion (bottom). Color code: signal (black), predicted isotope pattern for $[LuYL(NO_3)_2]^+$ (green), predicted isotope pattern for $[Y_2L(NO_3)_2]^+$ (red) and predicted isotope pattern for $[Lu_2L(NO_3)_2]^+$ (orange).

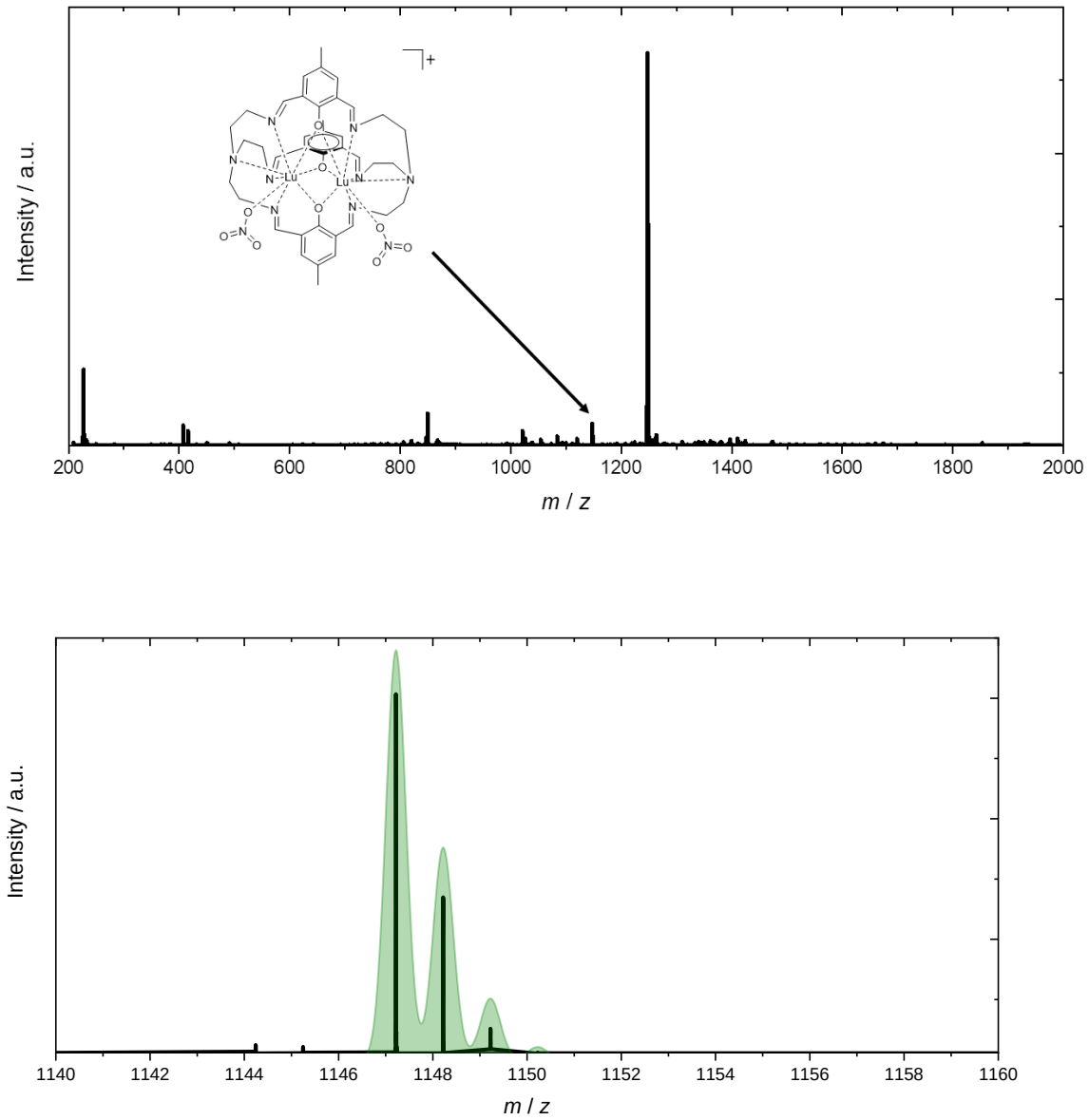

Figure S17. MALDI positive mode mass spectrum of $\mathbf{7_N}$ (top) with enlargement of the region of the molecular ion (bottom). Color code: signal (black) and predicted isotope pattern for $[Lu_2L(NO_3)_2]^+$ (green).

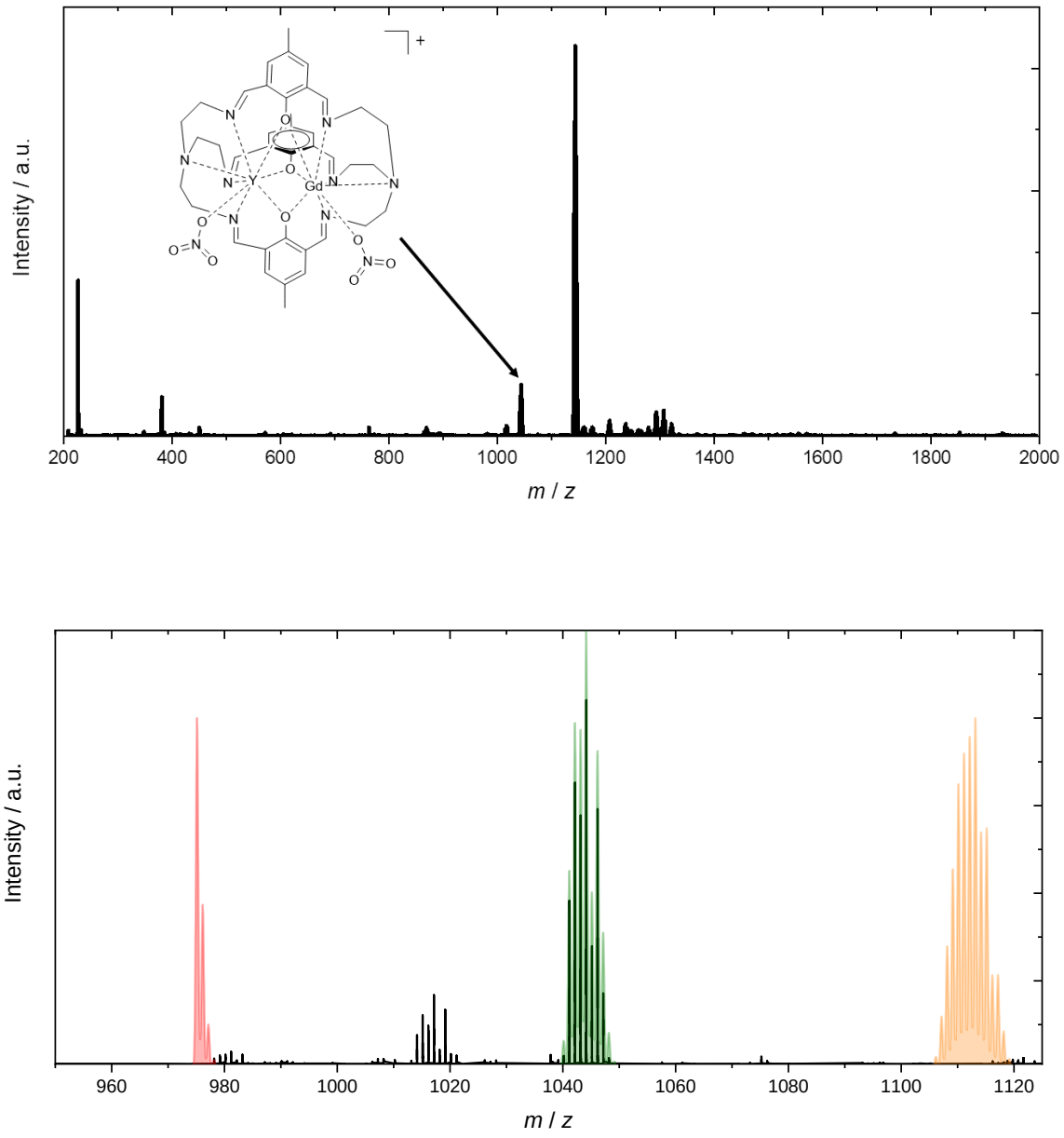

Figure S18. MALDI positive mode mass spectrum of $\mathbf{8_N}$ (top) with enlargement of the region of the molecular ion (bottom). Color code: signal (black), predicted isotope pattern for $[YGdL(NO_3)_2]^+$ (green), predicted isotope pattern for $[Y_2L(NO_3)_2]^+$ (red) and predicted isotope pattern for $[Gd_2L(NO_3)_2]^+$ (orange).

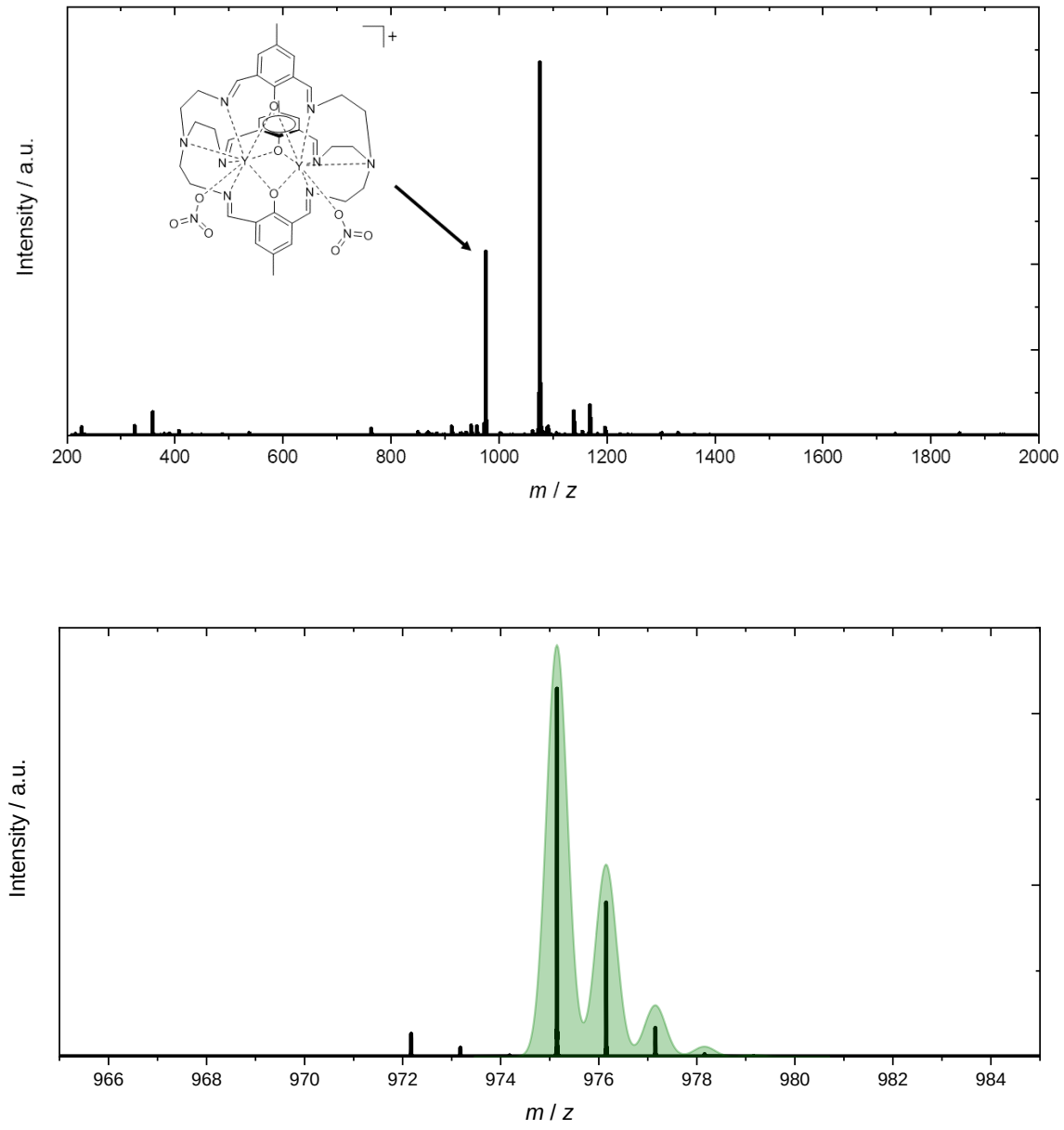

Figure S19. MALDI positive mode mass spectrum of $\mathbf{9_N}$ (top) with enlargement of the region of the molecular ion (bottom). Color code: signal (black) and predicted isotope pattern for $[Y_2L(NO_3)_2]^+$ (green).

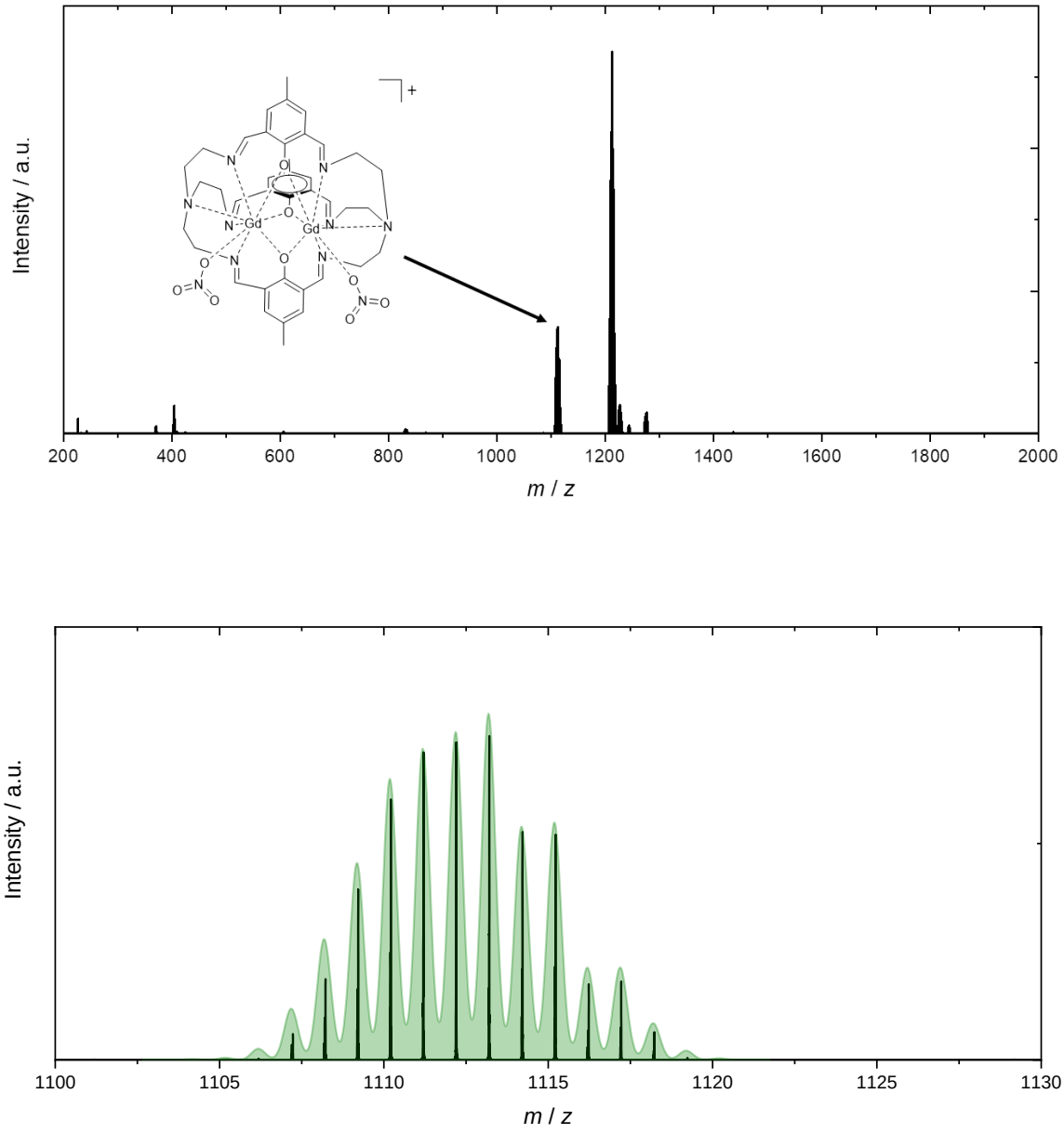

Figure S20. MALDI positive mode mass spectrum of **10**$_{\mathbf{N}}$ (top) with enlargement of the region of the molecular ion (bottom). Color code: signal (black) and predicted isotope pattern for $[Gd_2L(NO_3)_2]^+$ (green).

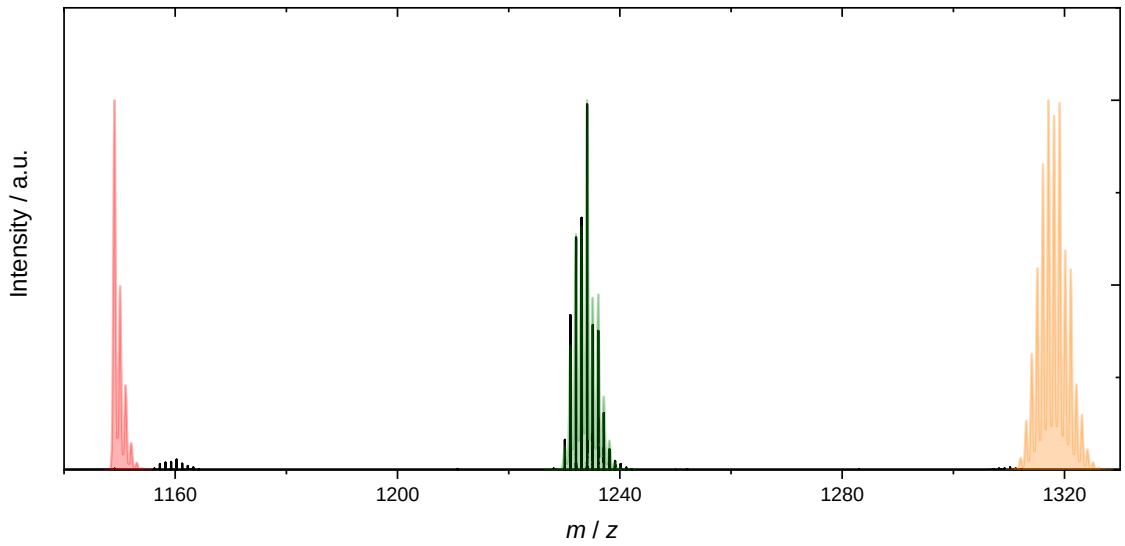

Figure S21. MALDI positive mode mass spectrum of a reaction involving $YbL \cdot 4H_2O$ and 3 eq. of $Y(OTf)_3 \cdot 9H_2O$ in pyridine refluxed for 3 hours. Color code: Signal (black), predicted isotope pattern for $[YbYL(OTf)_2]^+$ (green), predicted isotope pattern for $[Y_2L(OTf)_2]^+$ (red) and predicted isotope pattern for $[Yb_2L(OTf)_2]^+$ (orange).

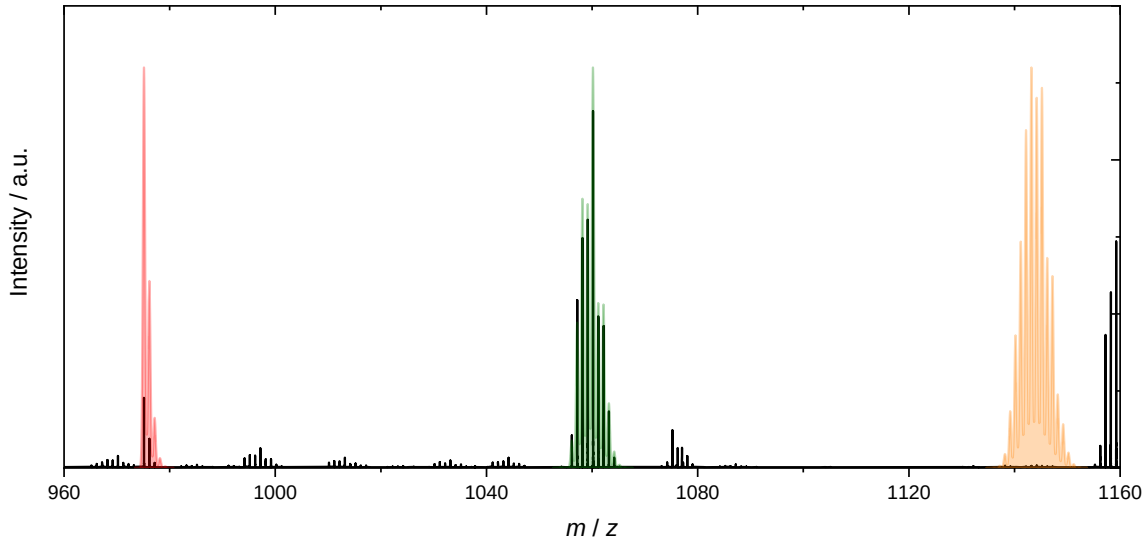

Figure S22. MALDI positive mode mass spectrum of a reaction involving $YbL \cdot 4H_2O$ and 3 eq. of $Y(NO_3)_3 \cdot 6H_2O$ in pyridine refluxed for 3 hours. Color code: Signal (black), predicted isotope pattern for $[YbYL(NO_3)_2]^+$ (green), predicted isotope pattern for $[Y_2L(NO_3)_2]^+$ (red) and predicted isotope pattern for $[Yb_2L(NO_3)_2]^+$ (orange).

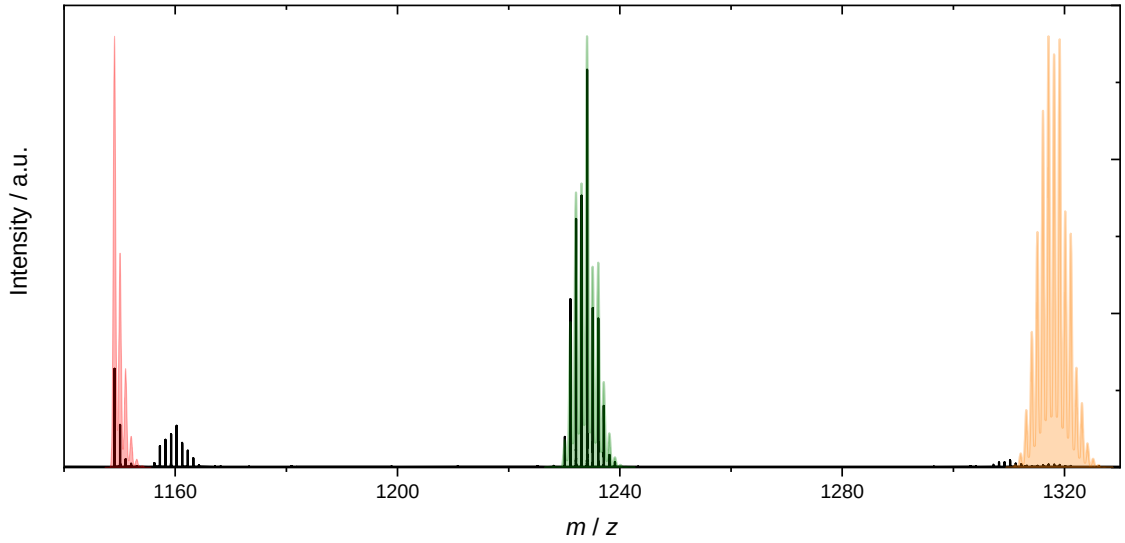

Figure S23. MALDI positive mode mass spectrum of a reaction involving $YbL \cdot 4H_2O$ and 3 eq. of $Y(OTf)_3 \cdot 9H_2O$ in PrCN refluxed for 3 hours. Color code: Signal (black), predicted isotope pattern for $[YbYL(OTf)_2]^+$ (green), predicted isotope pattern for $[Y_2L(OTf)_2]^+$ (red) and predicted isotope pattern for $[Yb_2L(OTf)_2]^+$ (orange).

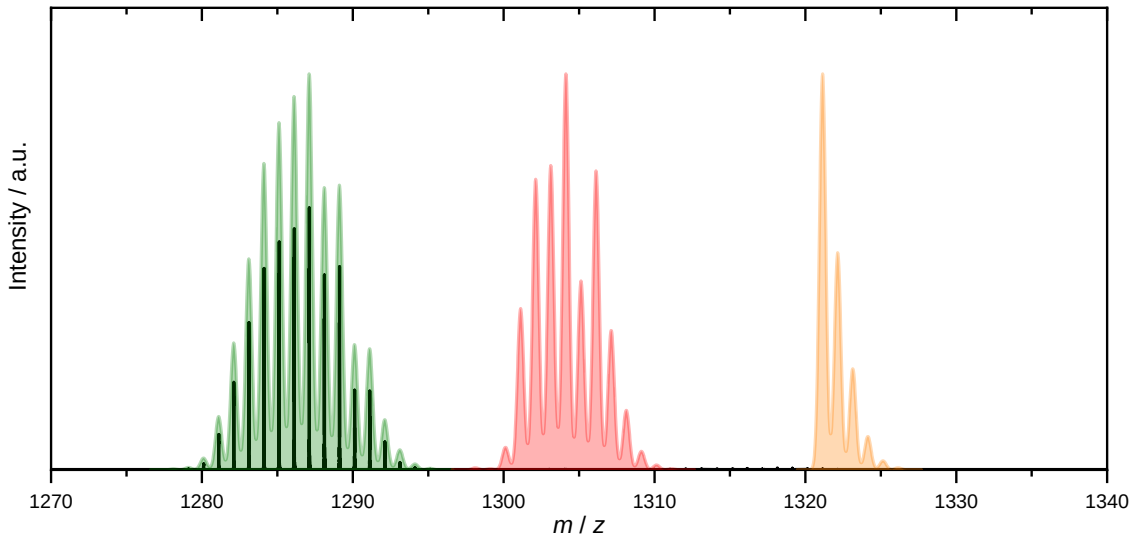

Figure S24. MALDI positive mode mass spectrum of a solution of **10** and 100 eq. of $Lu(OTf)_3 \cdot 9H_2O$ stirred for one week in MeOH. Color code: Signal (black), predicted isotope pattern for $[Gd_2L(OTf)_2]^+$ (green), predicted isotope pattern for $[LuGdL(OTf)_2]^+$ (red) and predicted isotope pattern for $[Lu_2L(OTf)_2]^+$ (orange).

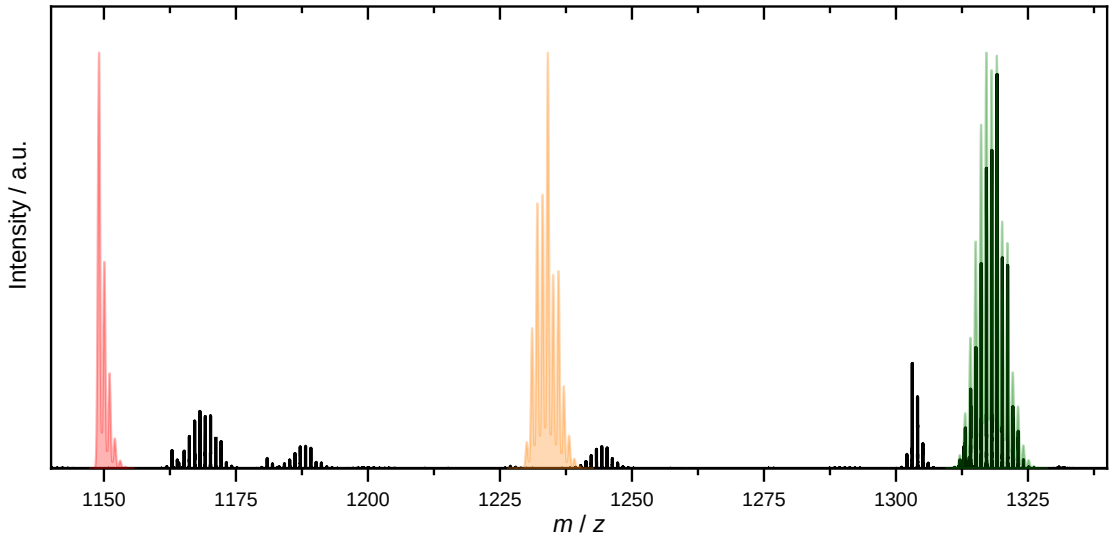

Figure S25. MALDI positive mode mass spectrum of a solution of **4** and 100 eq. of $Y(OTf)_3 \cdot 9H_2O$ stirred for one week in MeOH. Color code: Signal (black), predicted isotope pattern for $[Yb_2L(OTf)_2]^+$ (green), predicted isotope pattern for $[Y_2L(OTf)_2]^+$ (red) and predicted isotope pattern for $[YbYL(OTf)_2]^+$ (orange).

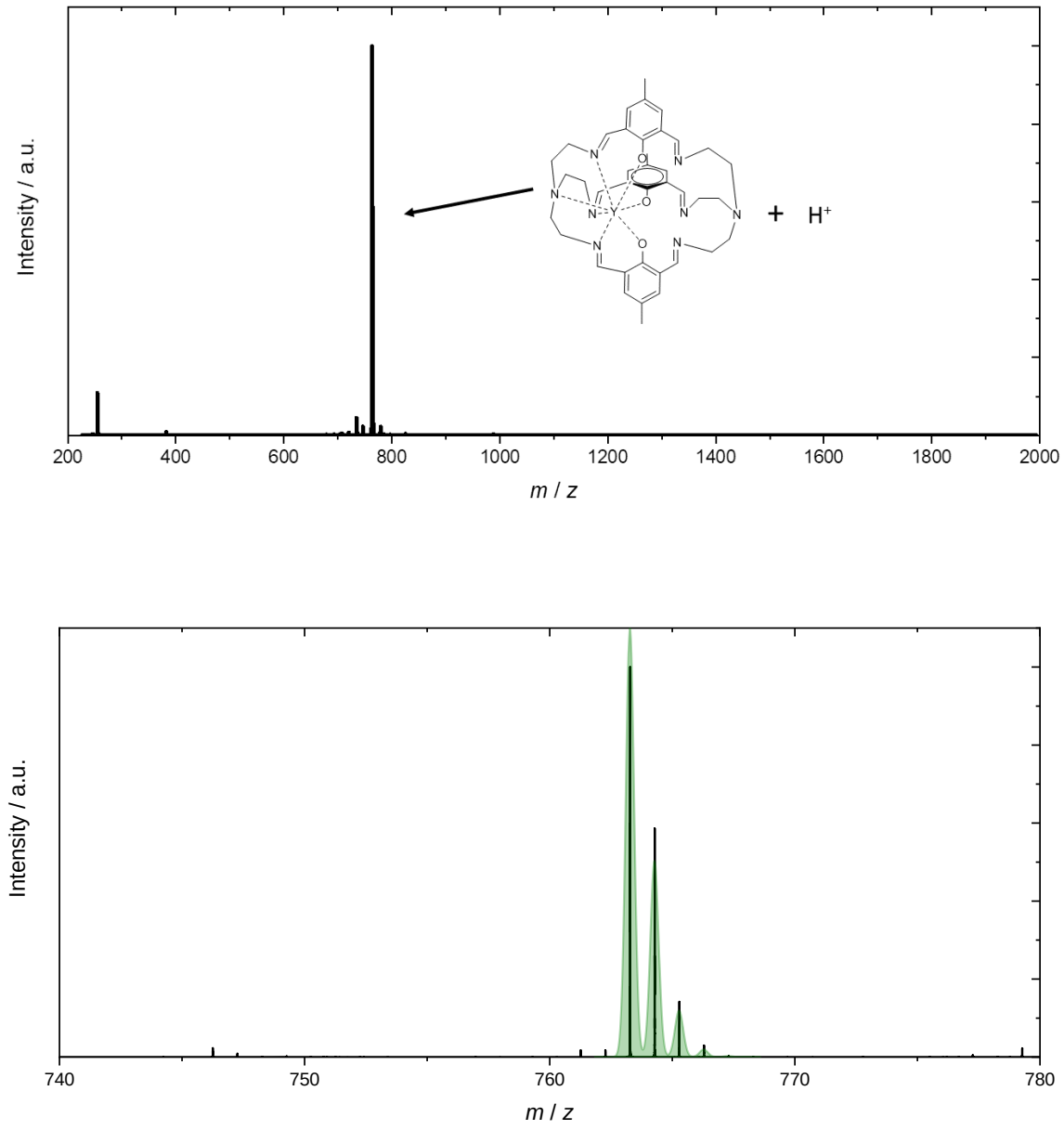

Figure S26. MALDI positive mode mass spectrum of $YL \cdot 4H_2O$ (top) with enlargement of the molecular region (bottom). Color code: Signal (black) and predicted isotope pattern (green).

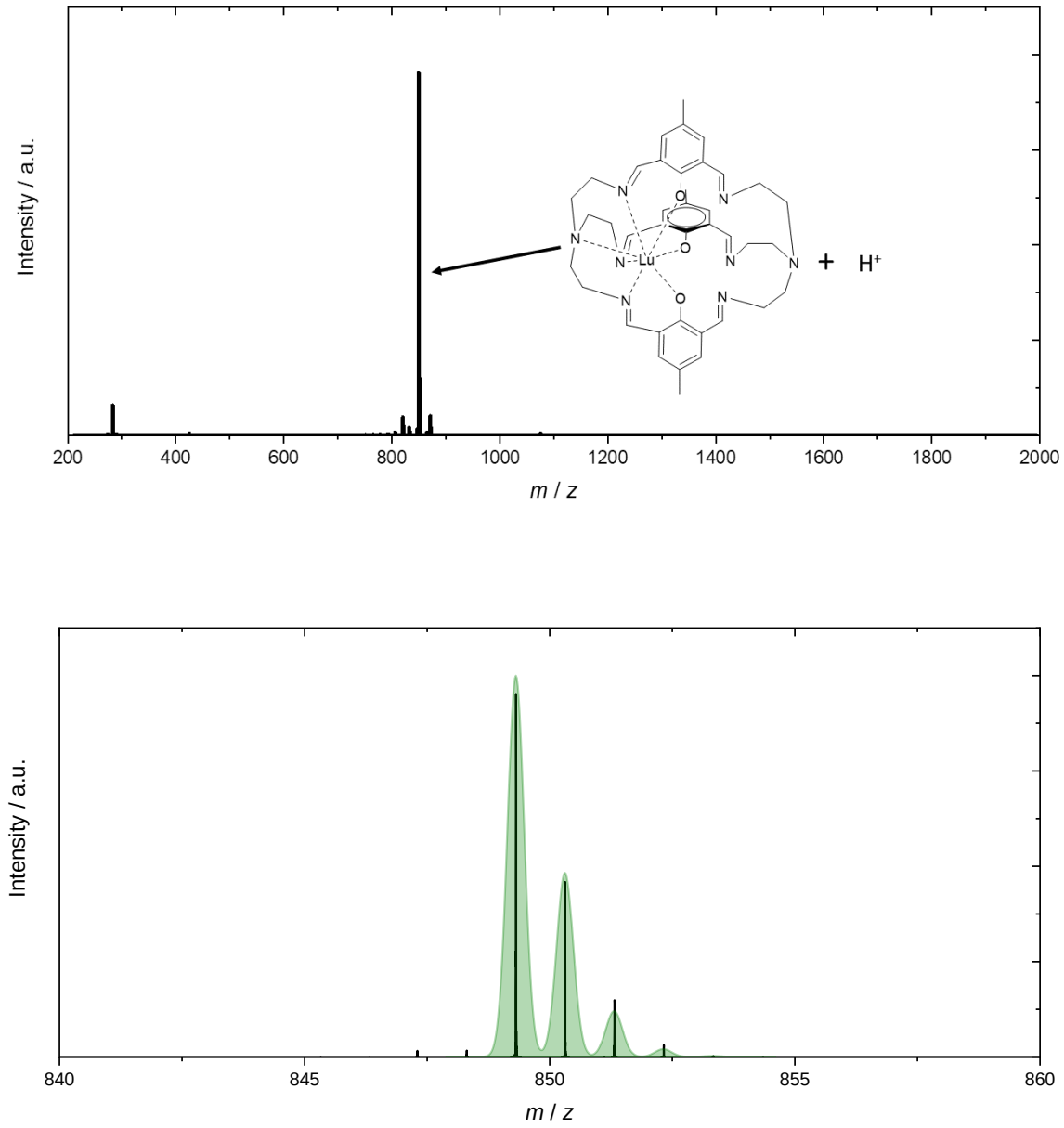

Figure S27. MALDI positive mode mass spectrum of $LuL \cdot 4H_2O$ (top) with enlargement of the molecular region (bottom). Color code: Signal (black) and predicted isotope pattern (green).

Infrared spectroscopy

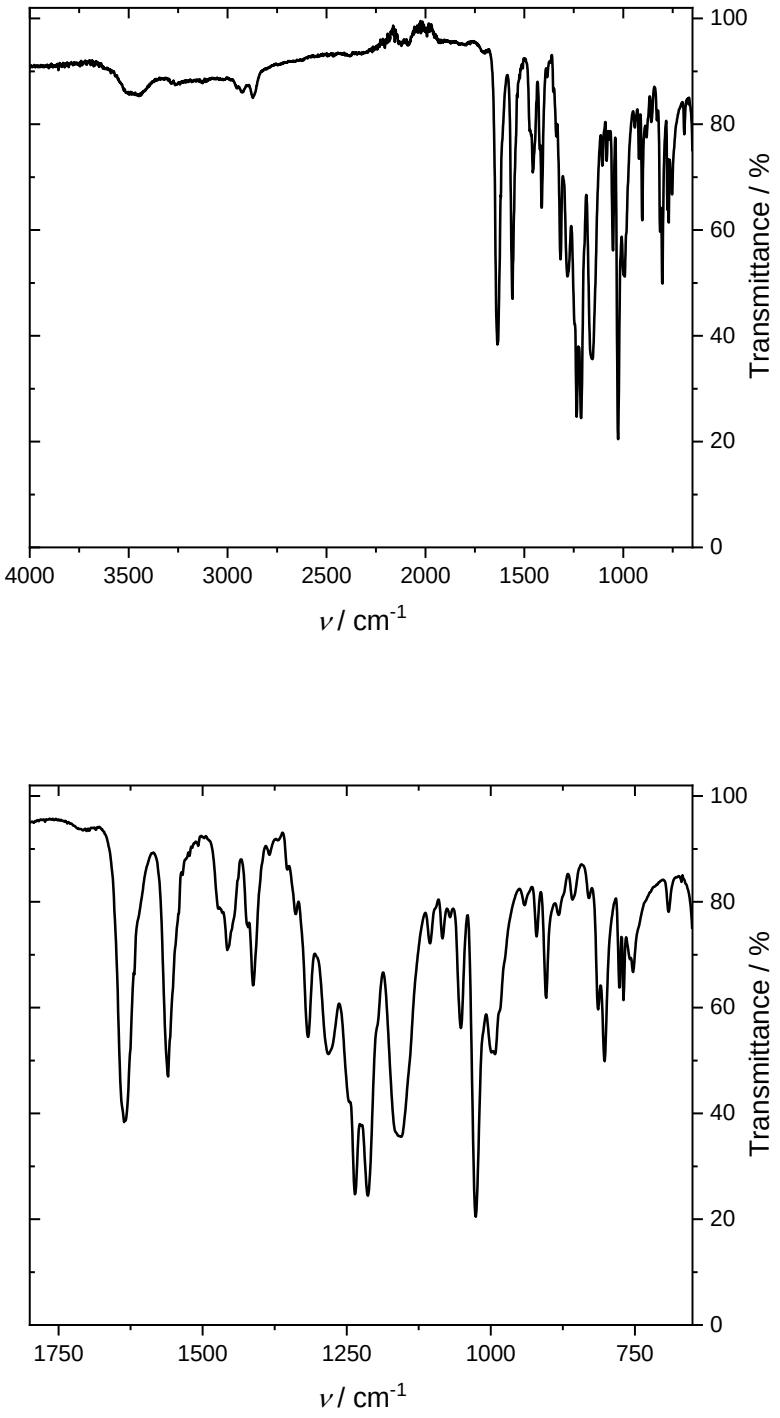

Figure S28. IR spectrum of **1** full range (top) and enlargement of the region 650-1800 cm^{-1} (bottom).

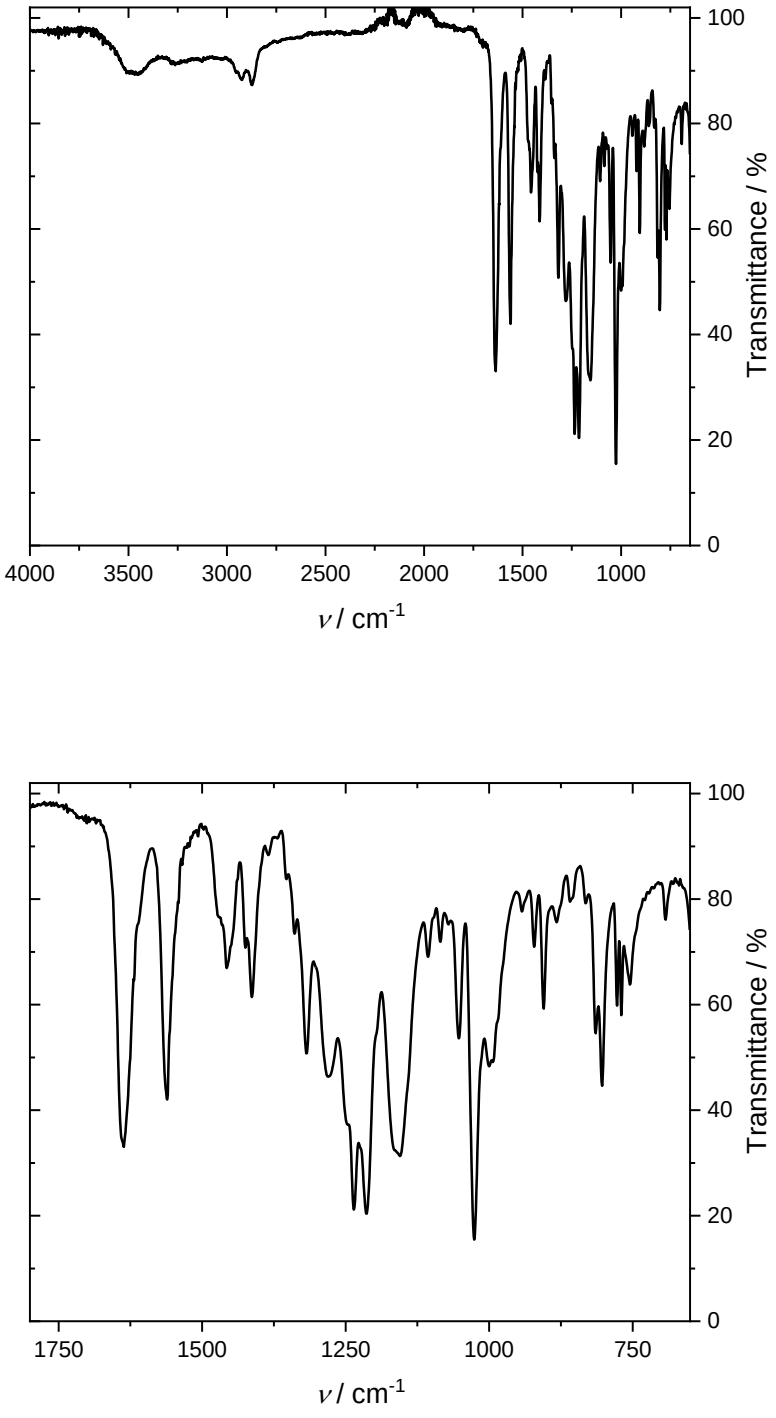

Figure S29. IR spectrum of **2** full range (top) and enlargement of the region 650-1800 cm^{-1} (bottom).

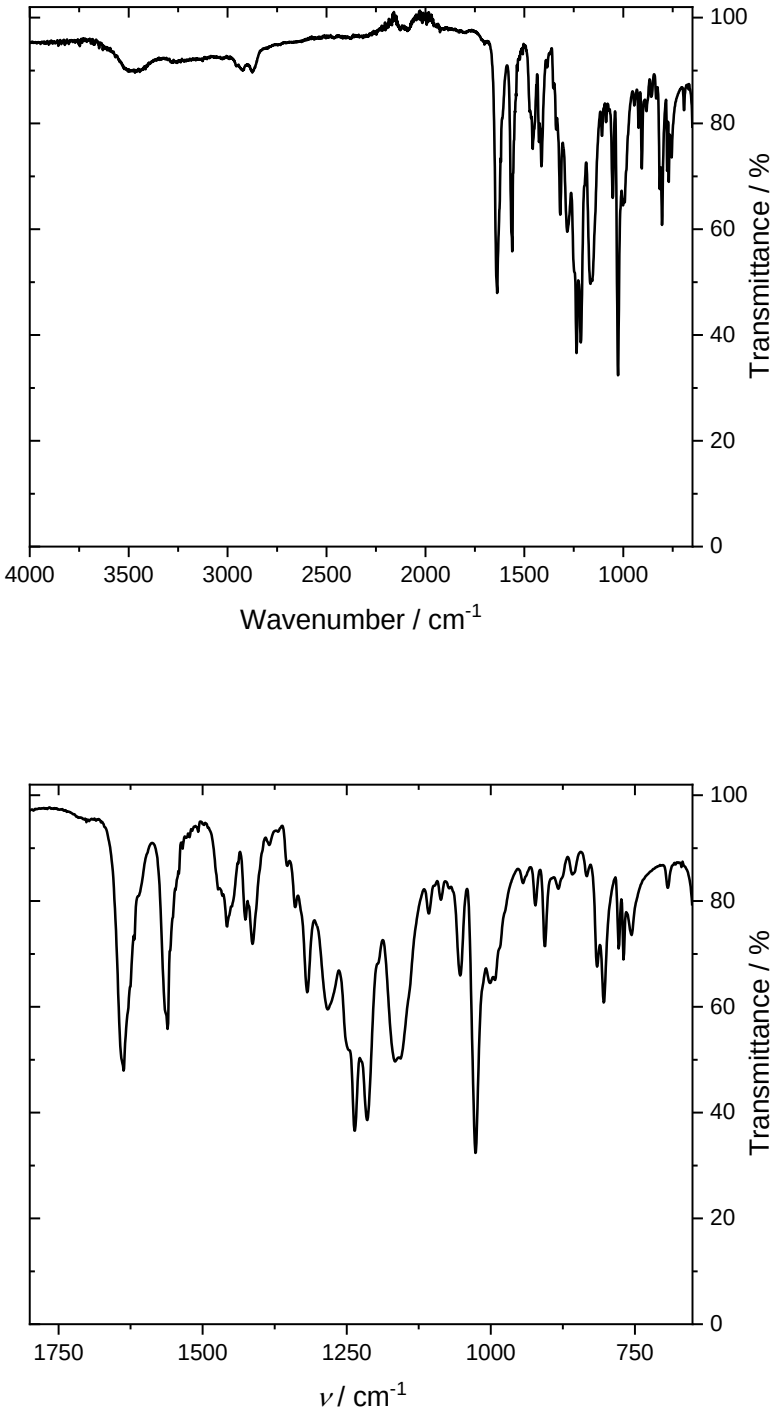

Figure S30. IR spectrum of **3** full range (top) and enlargement of the region 650-1800 cm^{-1} (bottom).

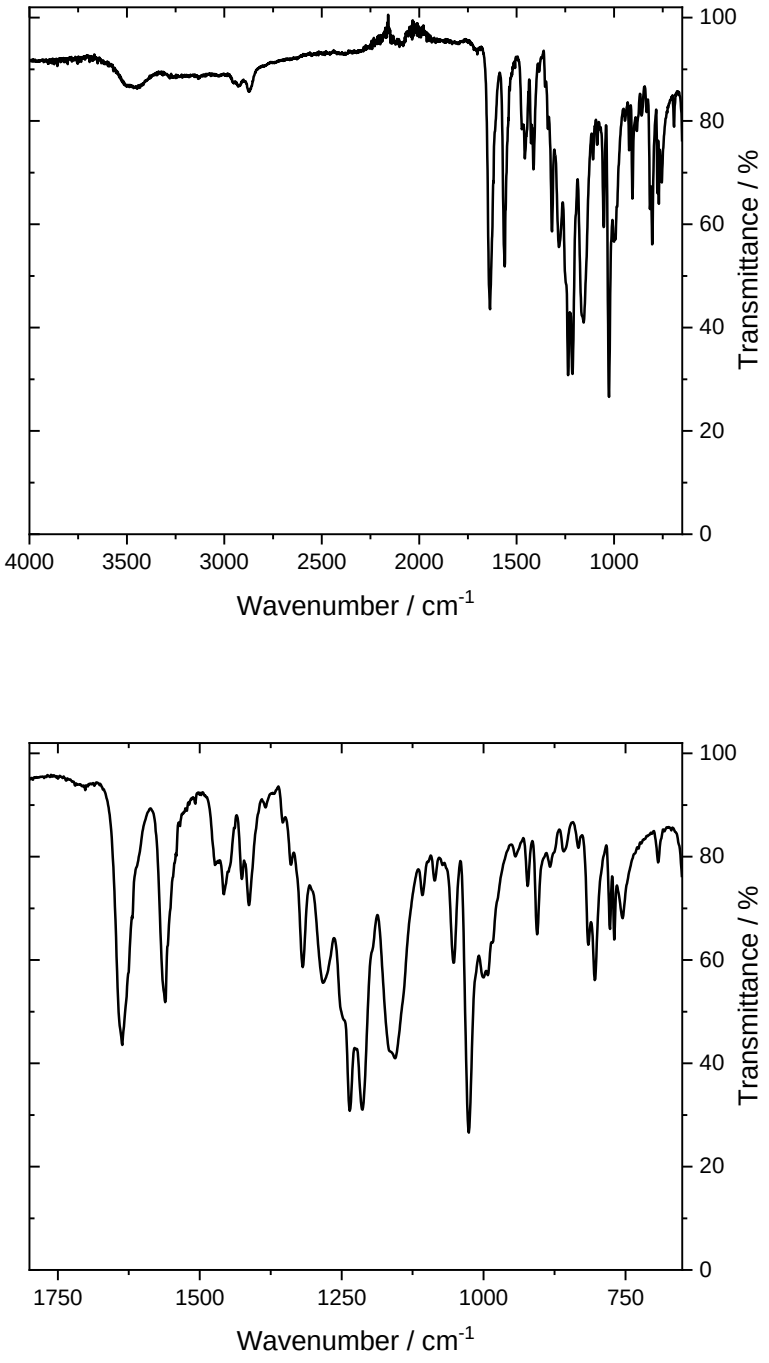

Figure S31. IR spectrum of **4** full range (top) and enlargement of the region 650-1800 cm^{-1} (bottom).

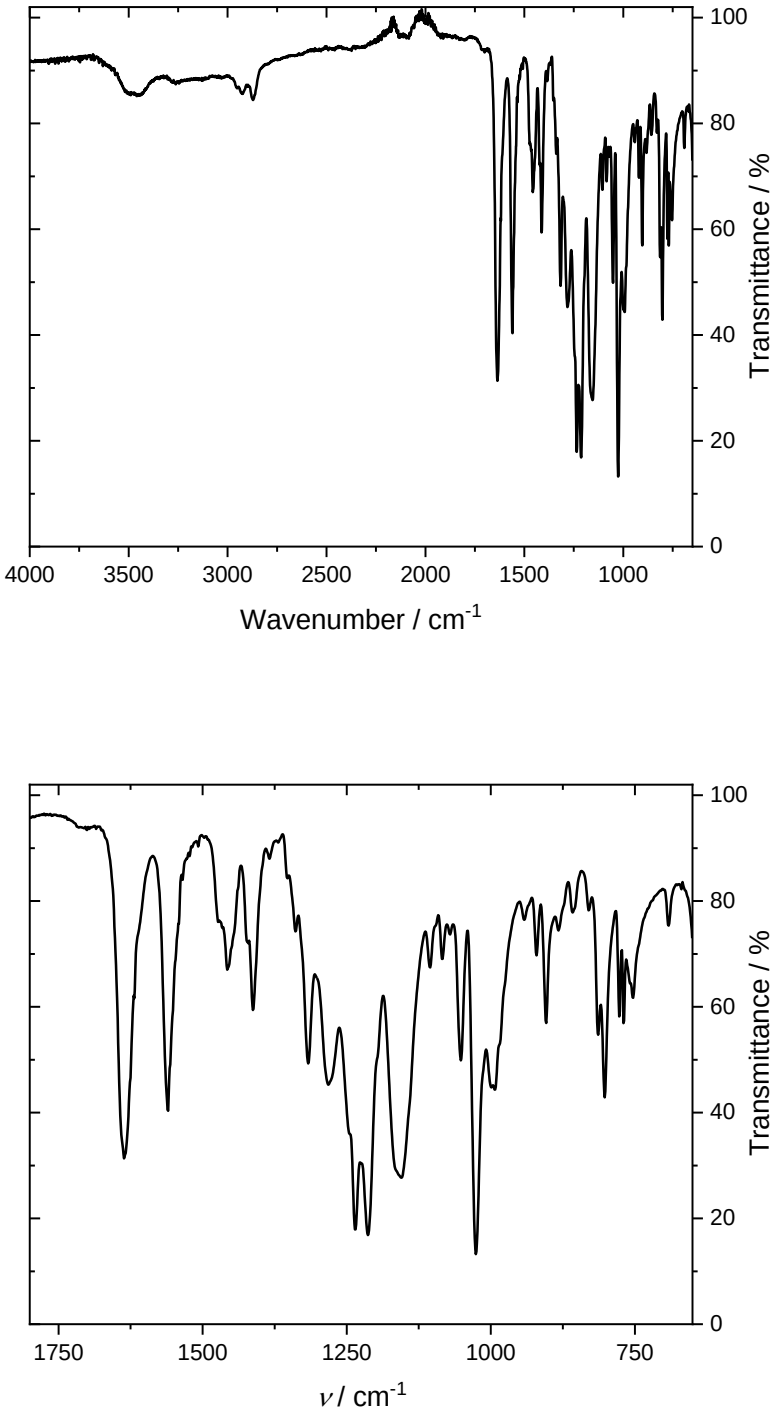

Figure S32. IR spectrum of **5** full range (top) and enlargement of the region 650-1800 cm^{-1} (bottom).

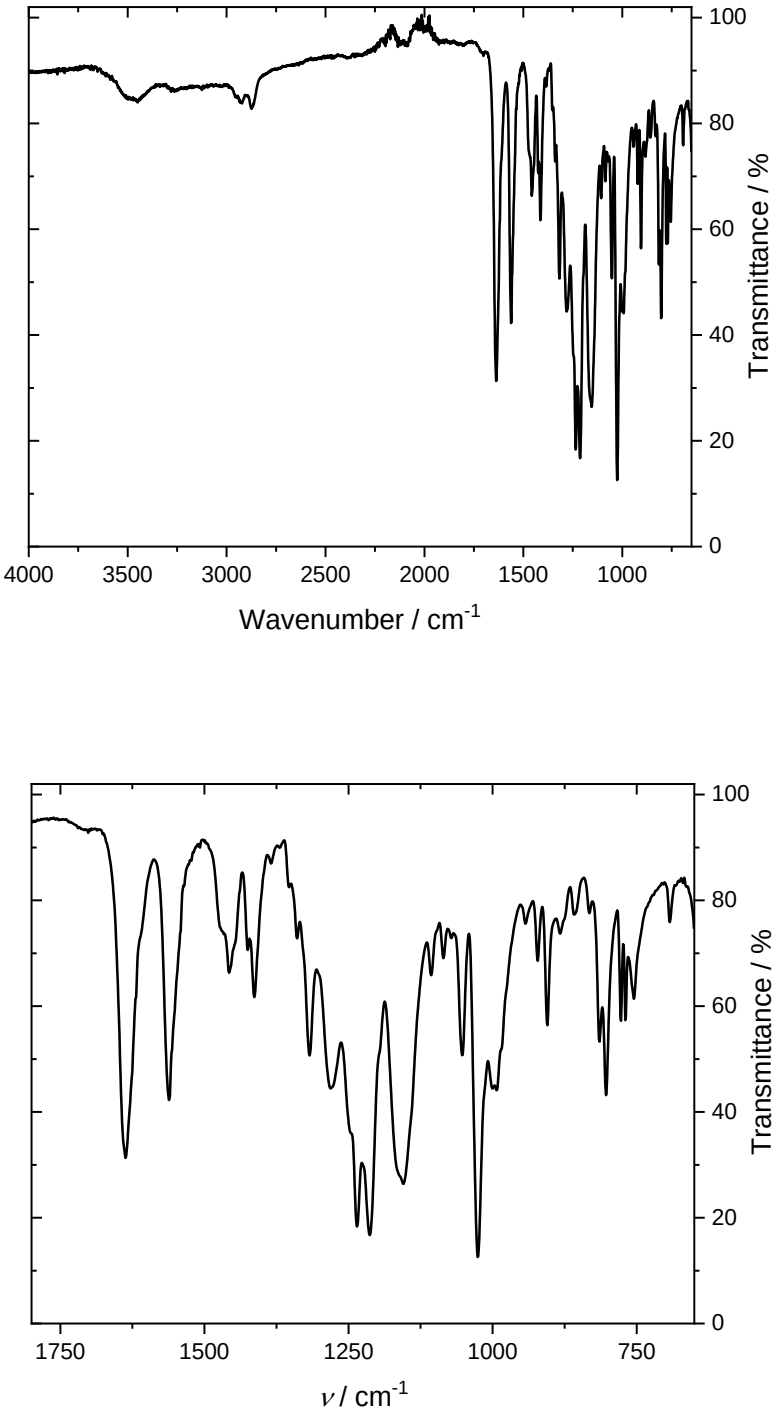

Figure S33. IR spectrum of **6** full range (top) and enlargement of the region 650-1800 cm^{-1} (bottom).

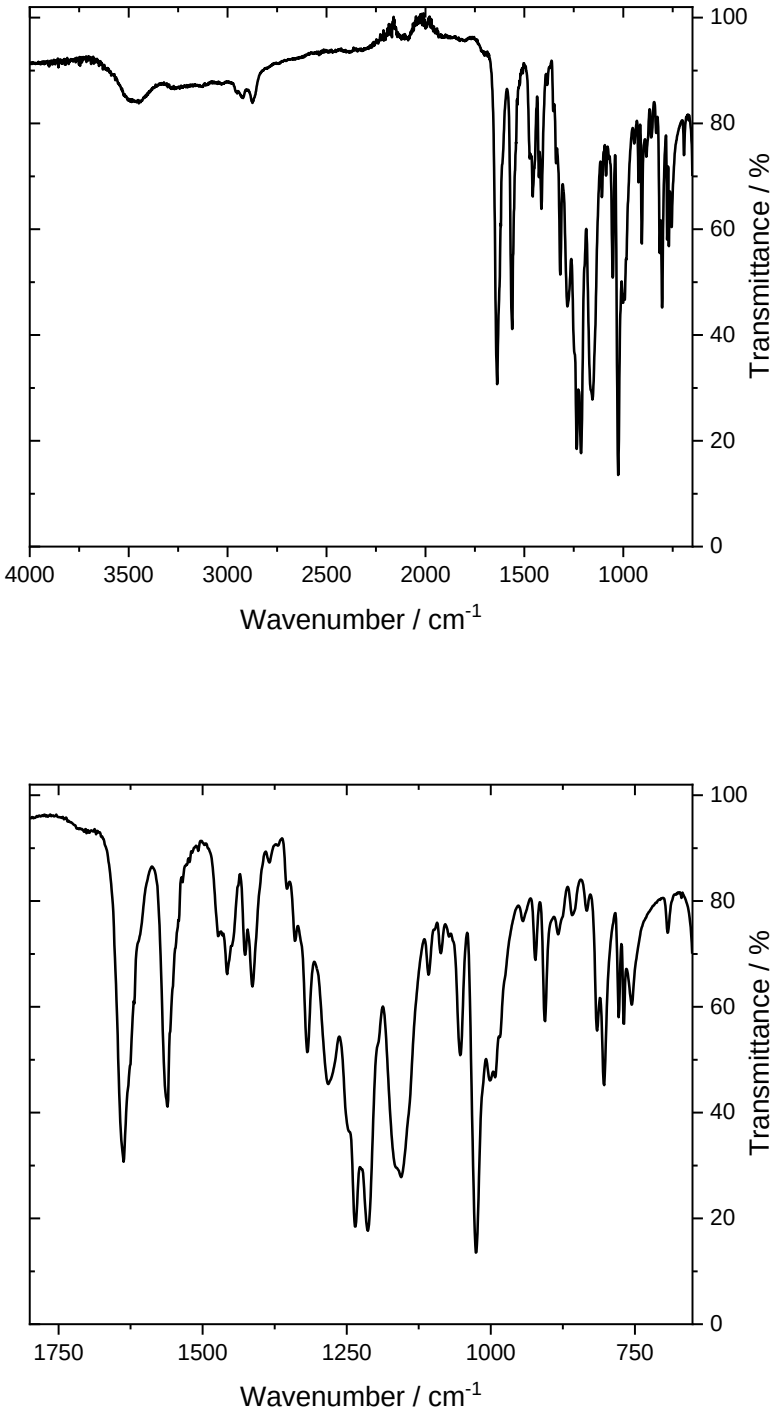

Figure S34. IR spectrum of **7** full range (top) and enlargement of the region 650-1800 cm^{-1} (bottom).

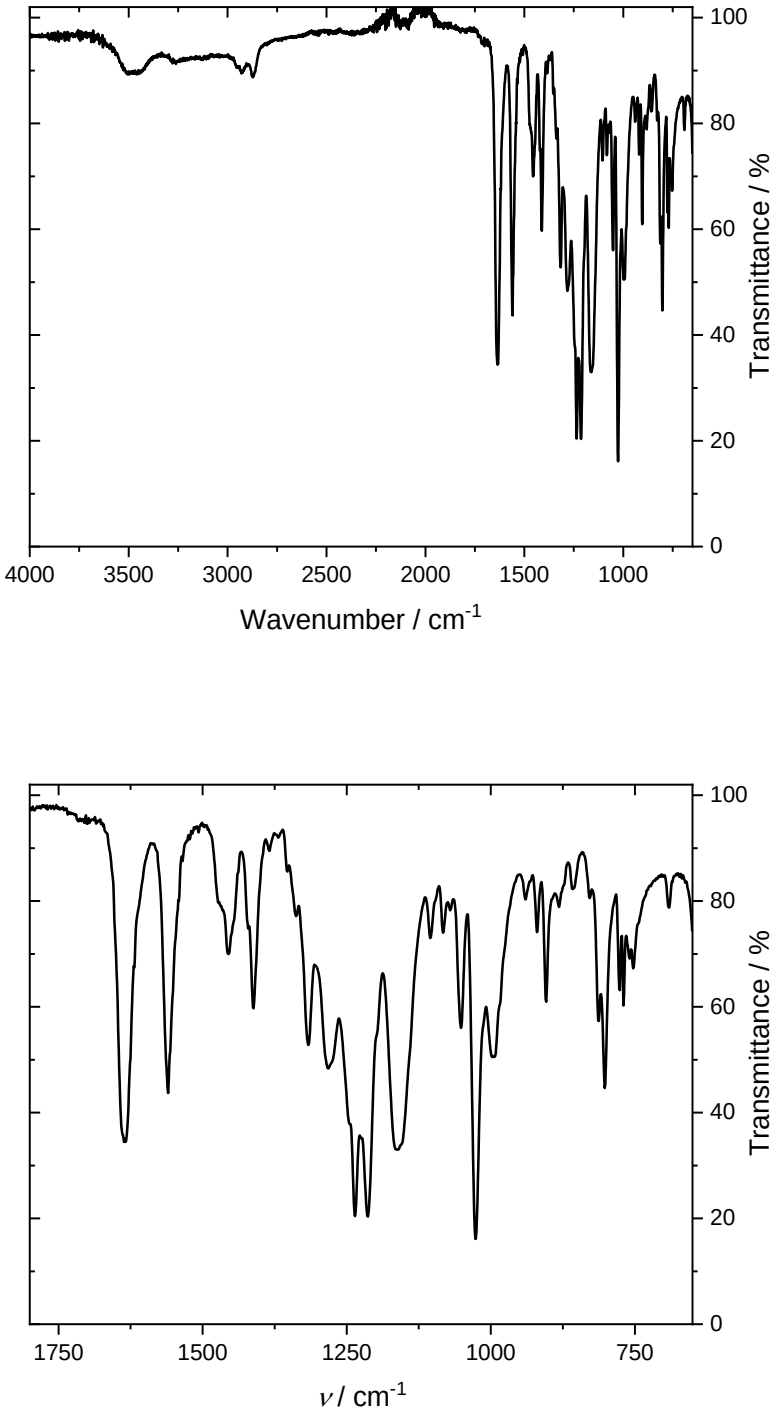

Figure S35. IR spectrum of **8** full range (top) and enlargement of the region 650-1800 cm^{-1} (bottom).

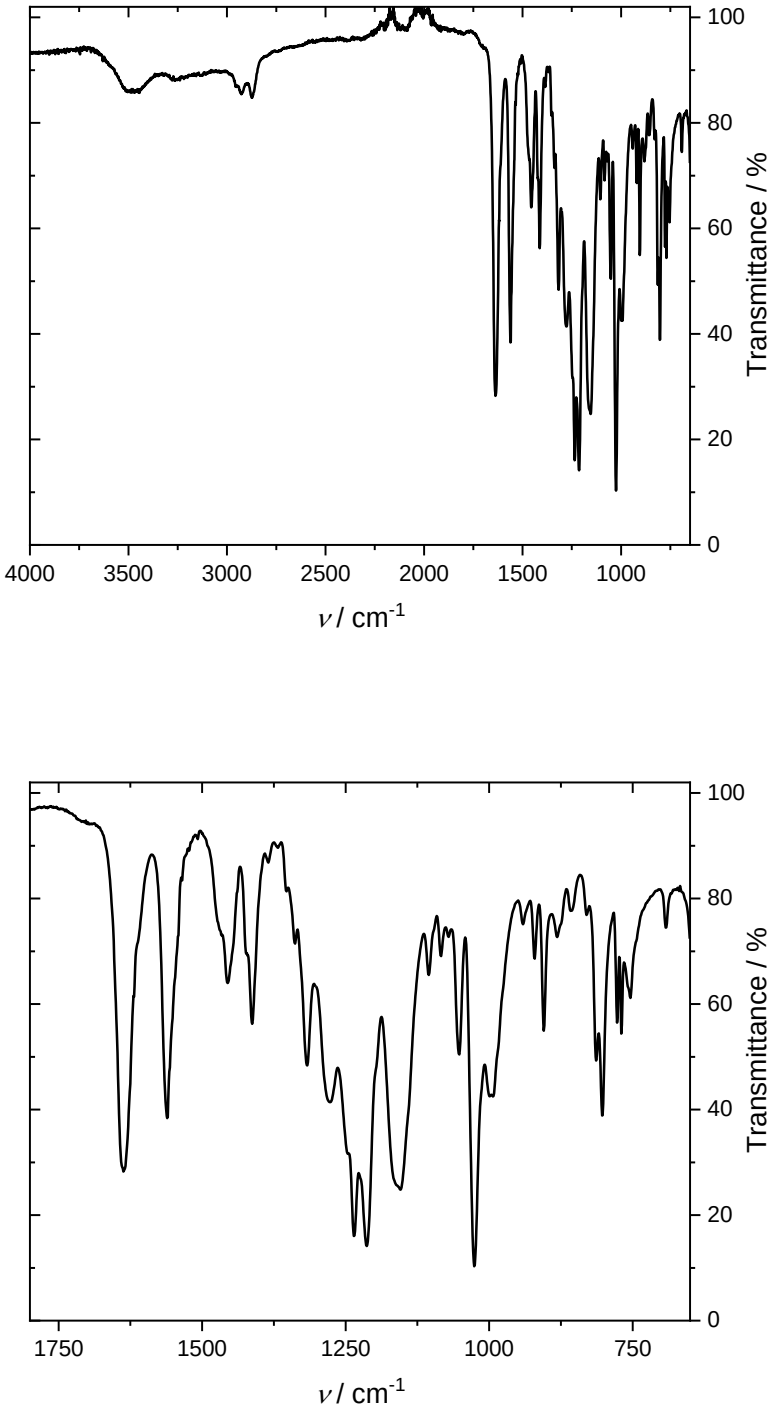

Figure S36. IR spectrum of **9** full range (top) and enlargement of the region 650-1800 cm^{-1} (bottom).

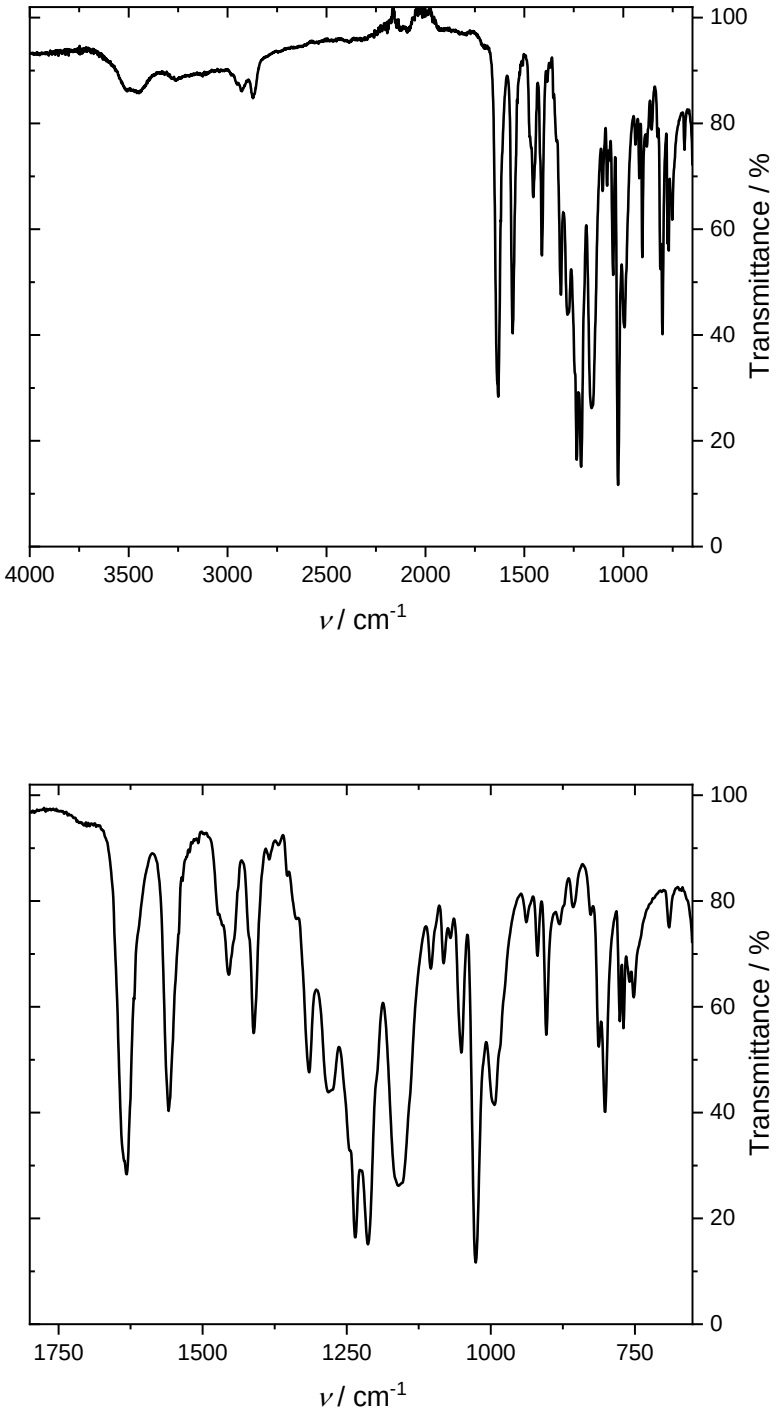

Figure S37. IR spectrum of **10** full range (top) and enlargement of the region 650-1800 cm^{-1} (bottom).

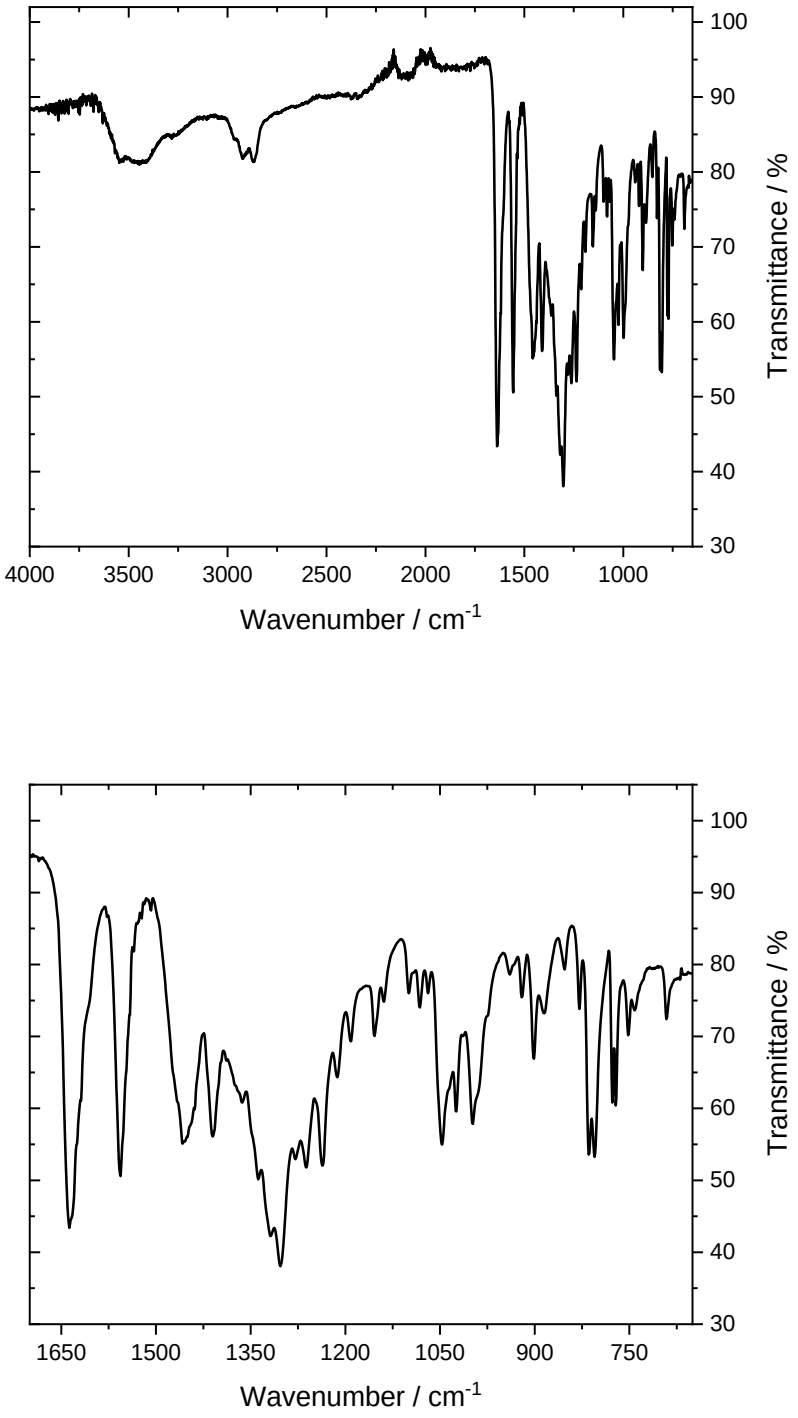

Figure S38. IR spectrum of $\mathbf{1_N}$ full range (top) and enlargement of the region 650-1700 cm^{-1} (bottom).

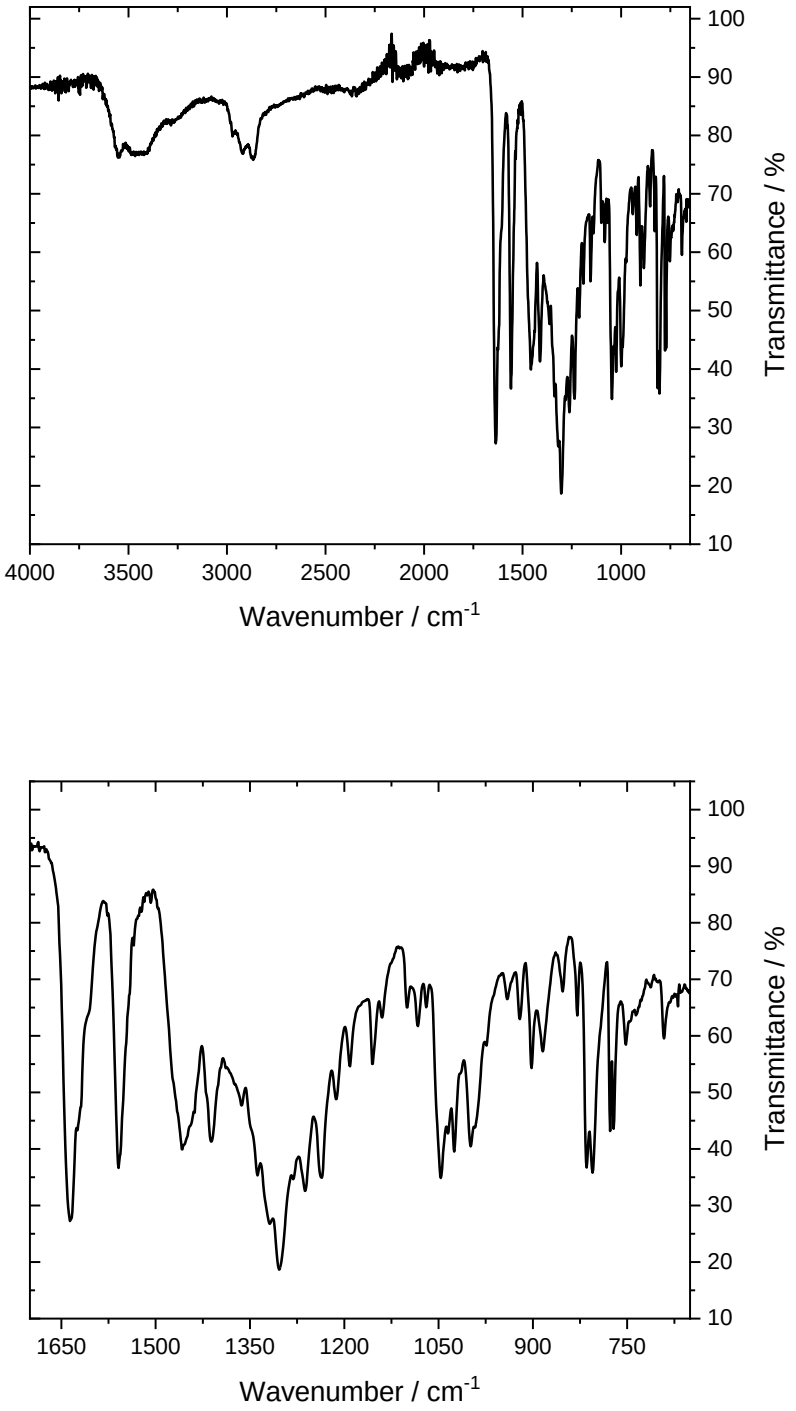

Figure S39. IR spectrum of $\mathbf{2_N}$ full range (top) and enlargement of the region 650-1700 cm^{-1} (bottom).

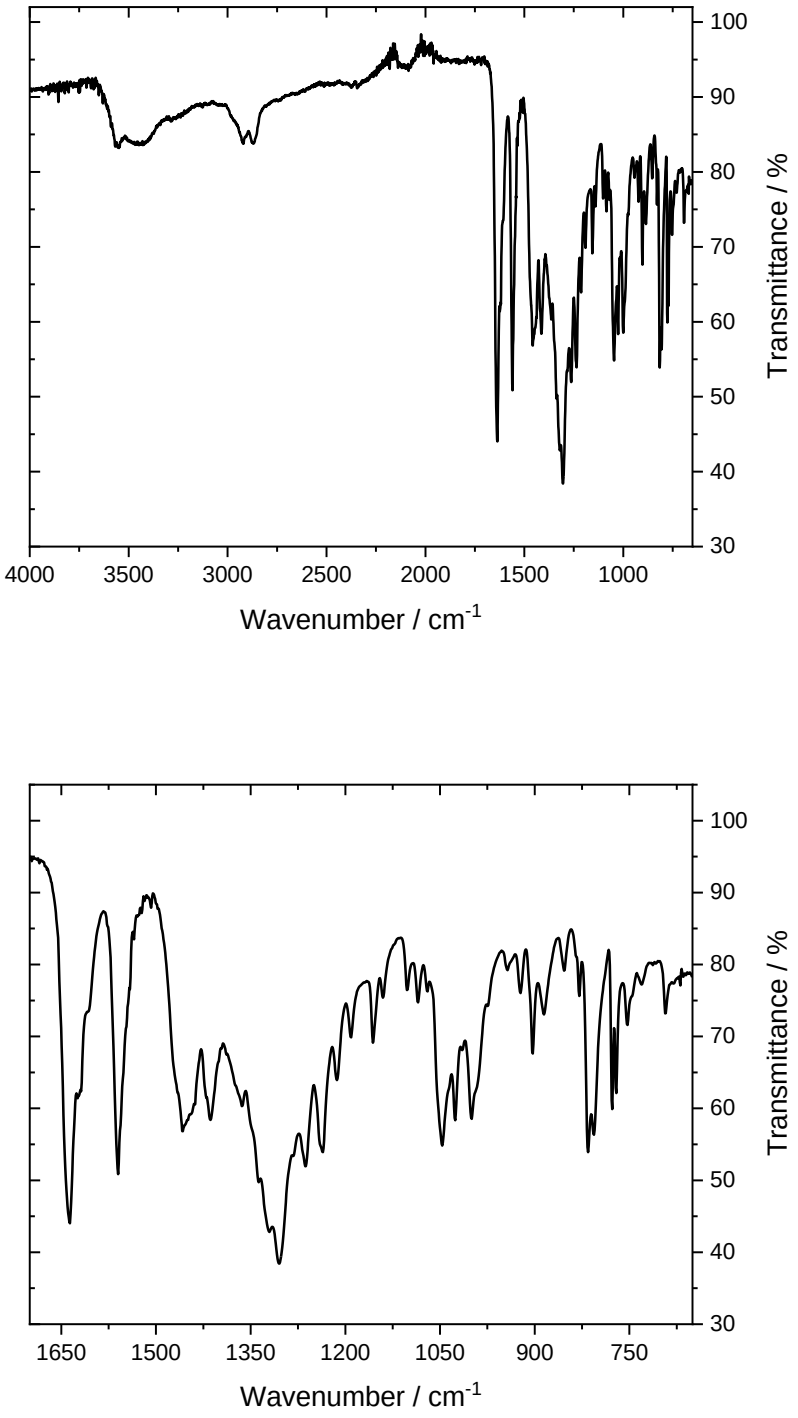

Figure S40. IR spectrum of $\mathbf{3_N}$ full range (top) and enlargement of the region 650-1700 cm^{-1} (bottom).

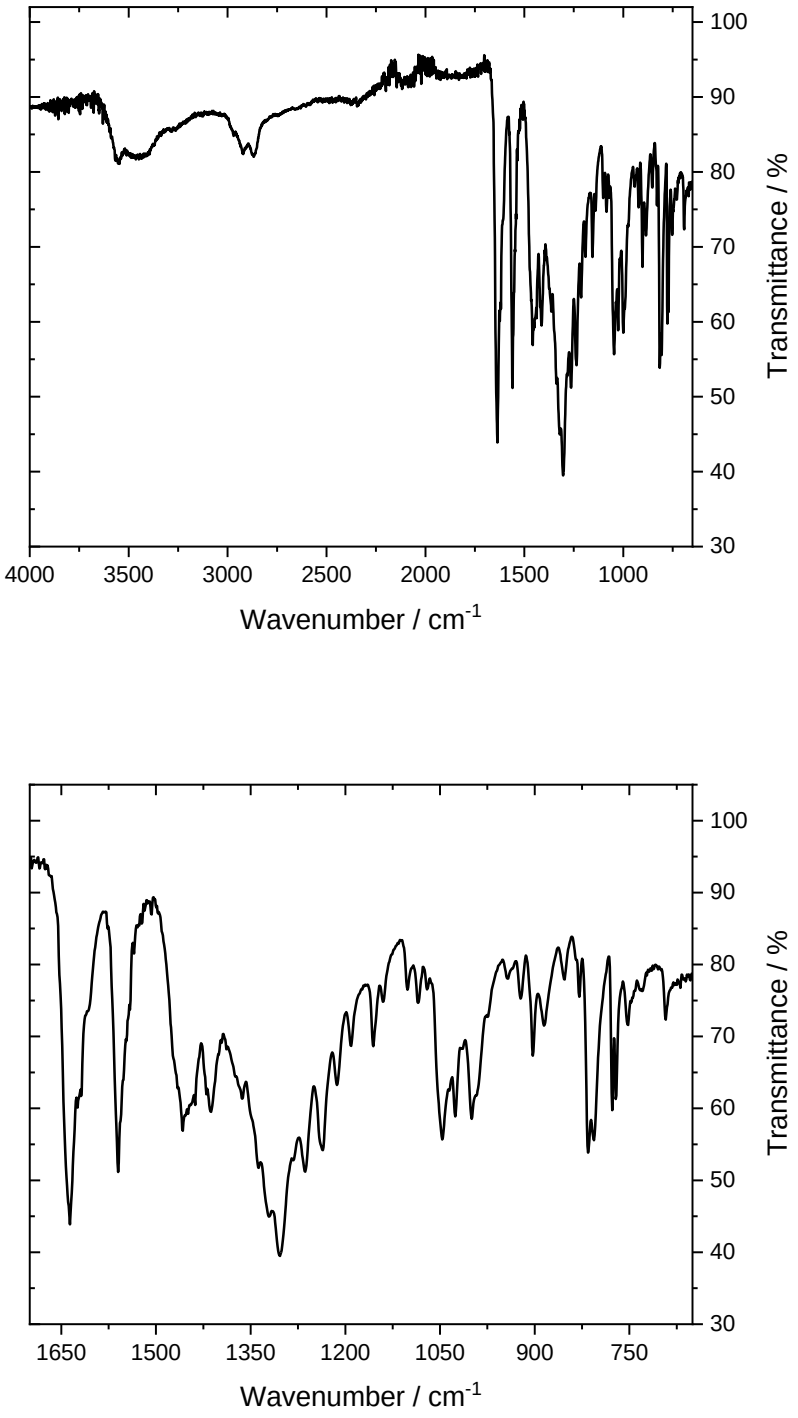

Figure S41. IR spectrum of $\mathbf{4_N}$ full range (top) and enlargement of the region 650-1700 cm^{-1} (bottom).

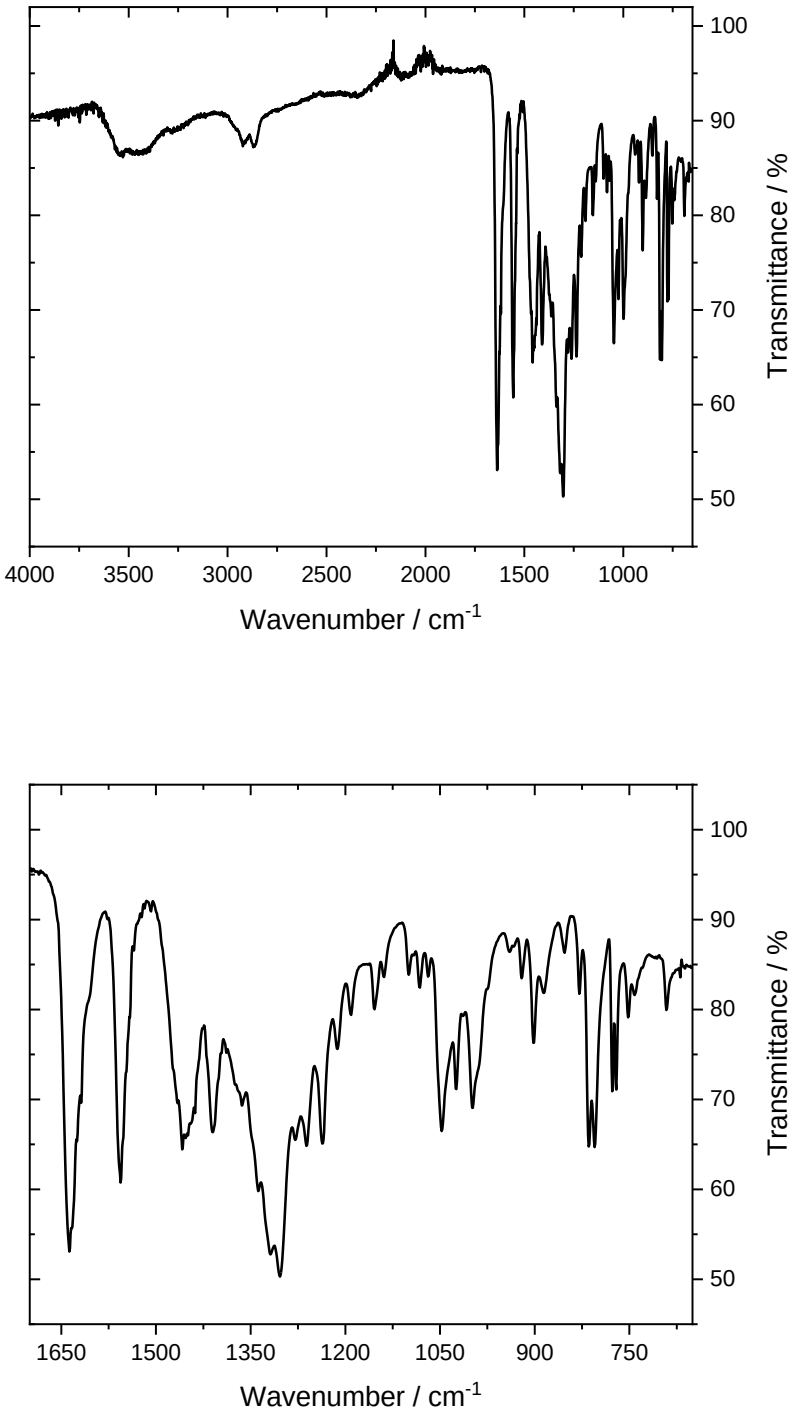

Figure S42. IR spectrum of $\mathbf{5_N}$ full range (top) and enlargement of the region 650-1700 cm^{-1} (bottom).

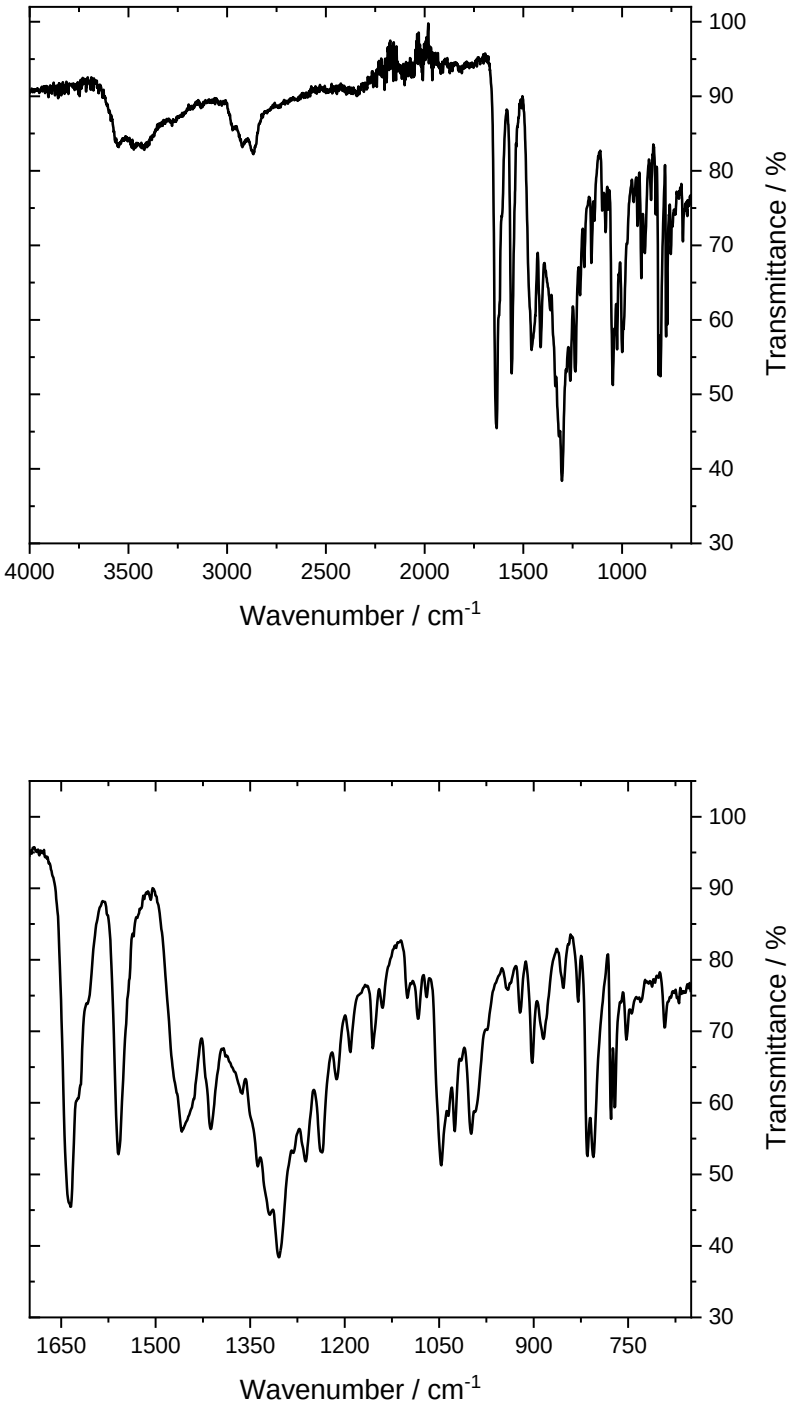

Figure S43. IR spectrum of $\mathbf{6_N}$ full range (top) and enlargement of the region 650-1700 cm^{-1} (bottom).

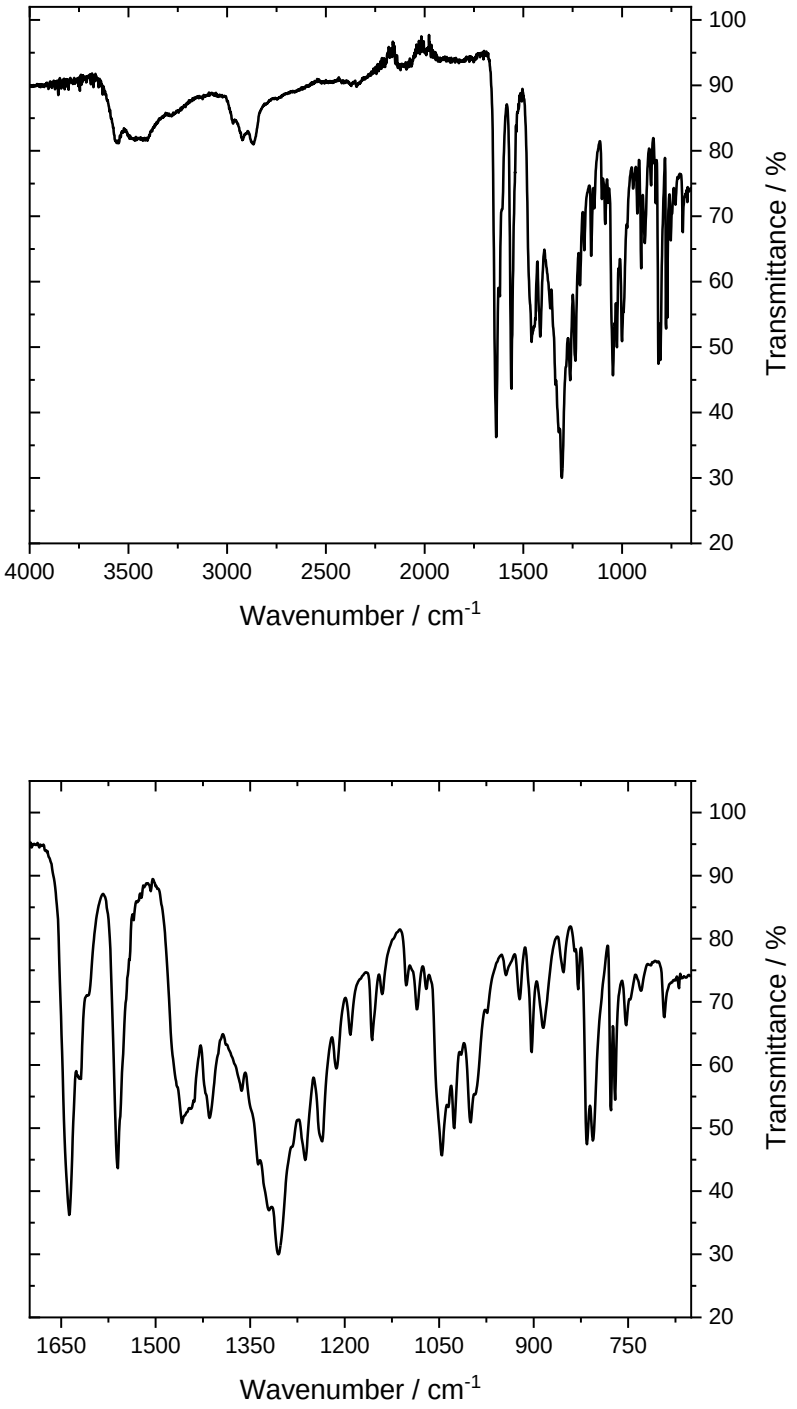

Figure S44. IR spectrum of $\mathbf{7_N}$ full range (top) and enlargement of the region 650-1700 cm^{-1} (bottom).

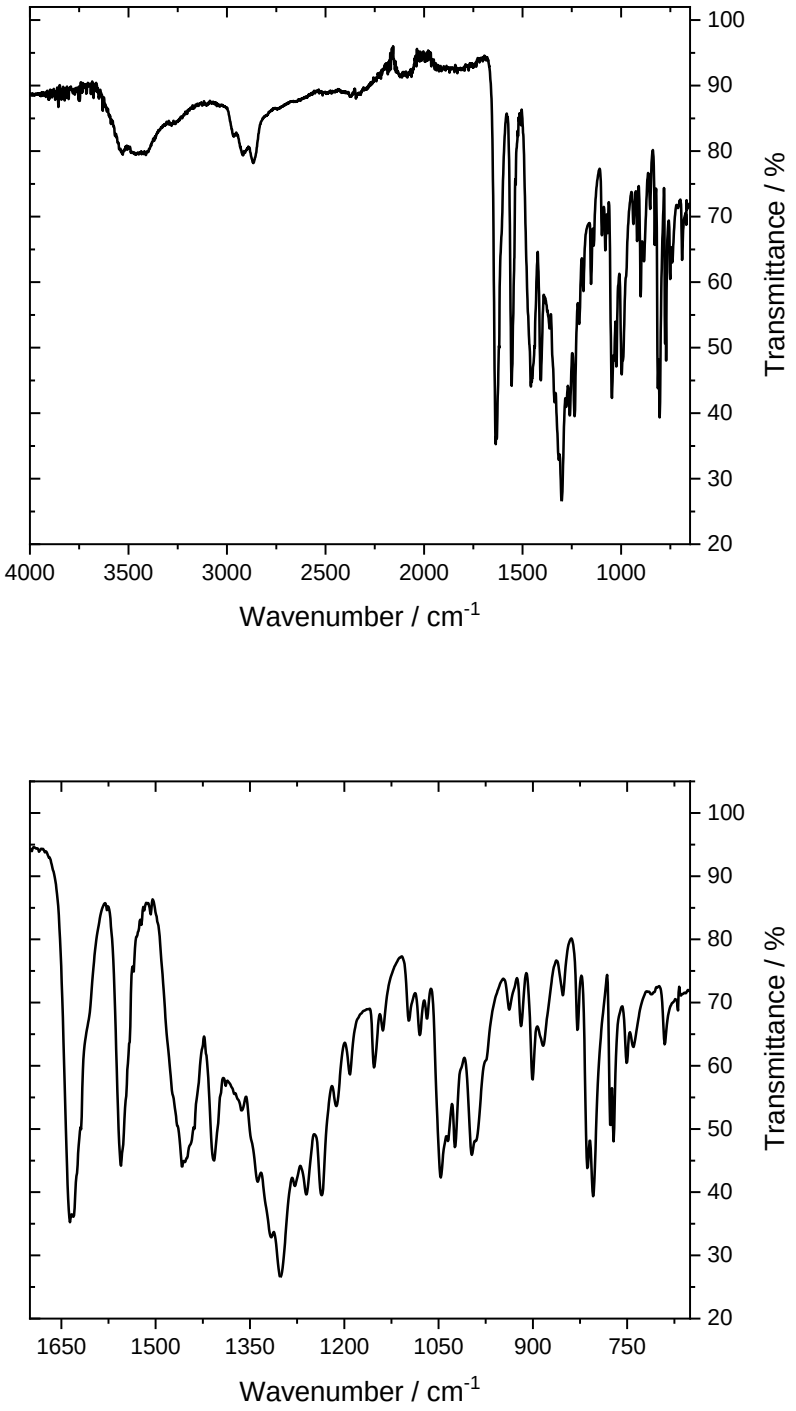

Figure S45. IR spectrum of $\mathbf{8_N}$ full range (top) and enlargement of the region 650-1700 cm^{-1} (bottom).

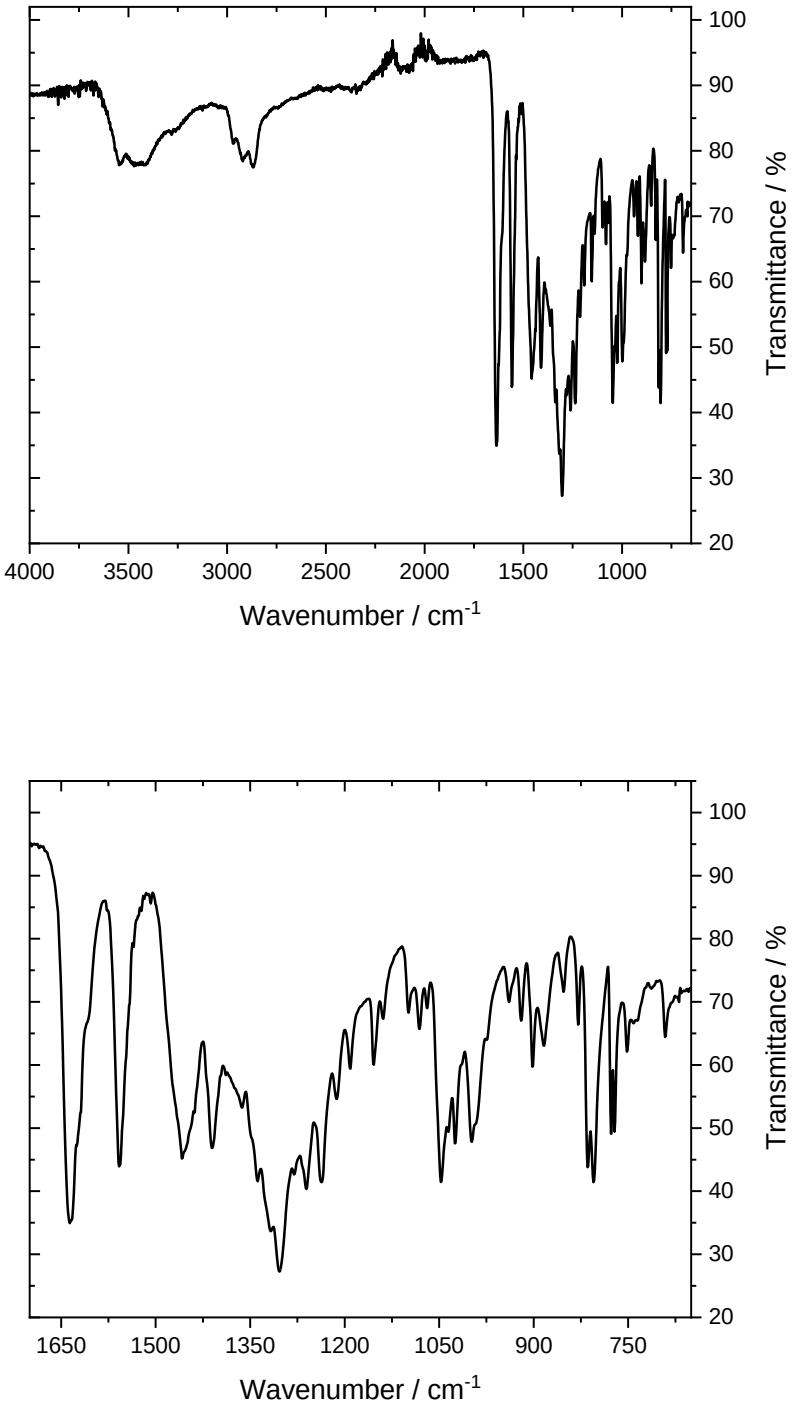

Figure S46. IR spectrum of $\mathbf{9_N}$ full range (top) and enlargement of the region 650-1700 cm^{-1} (bottom).

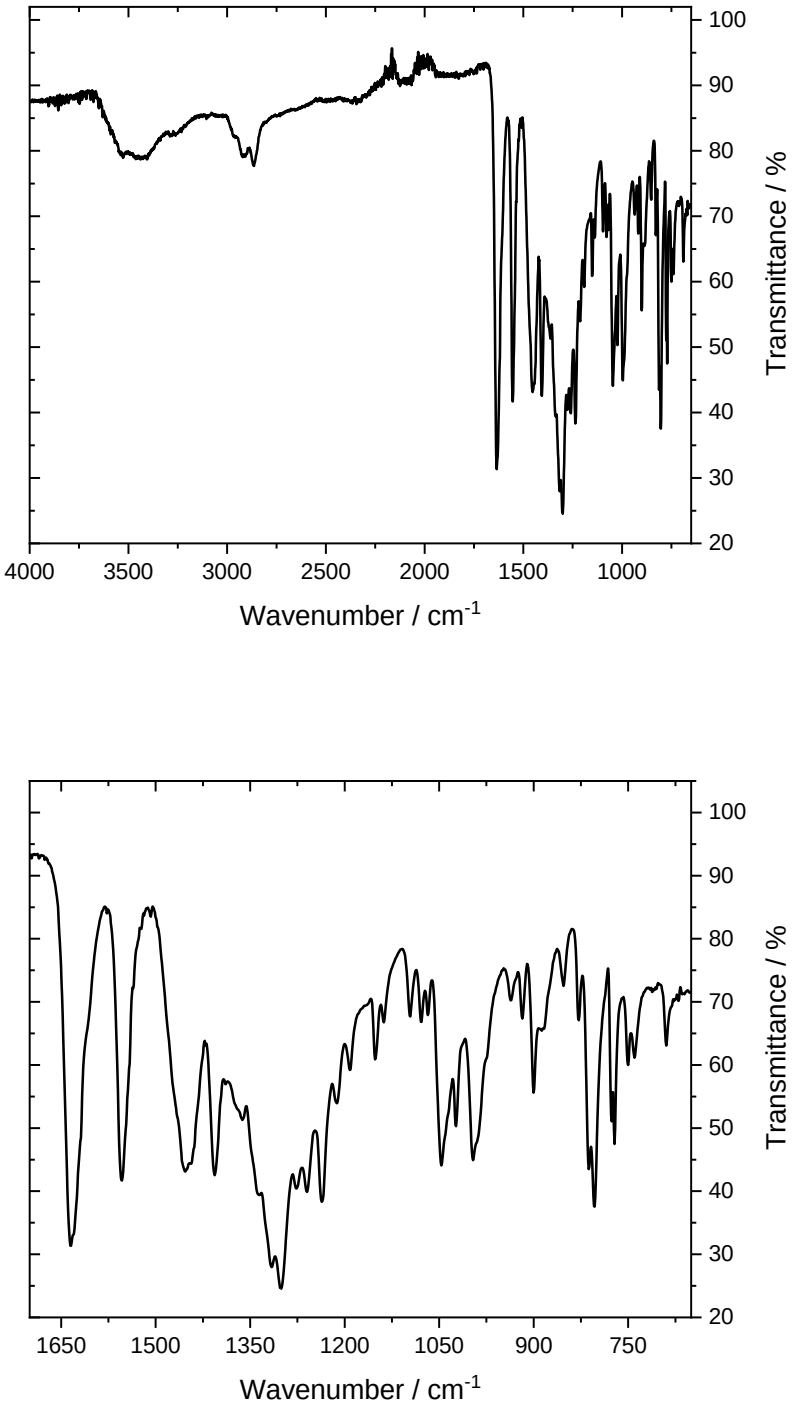

Figure S47. IR spectrum of $\mathbf{10_N}$ full range (top) and enlargement of the region 650-1700 cm^{-1} (bottom).

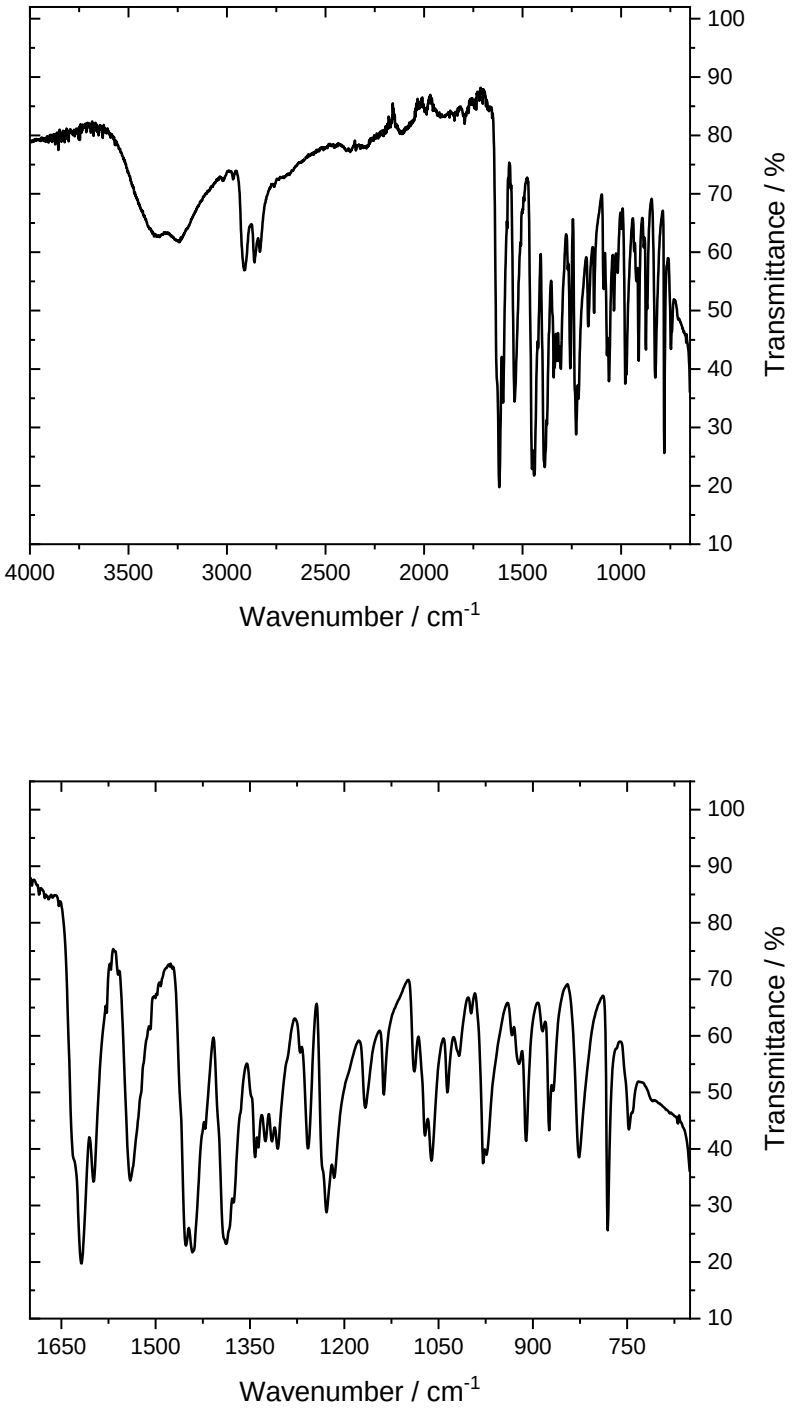

Figure S48. IR spectrum of **YL·4H$_2$O** full range (top) and enlargement of the region 650-1700 cm^{-1} (bottom).

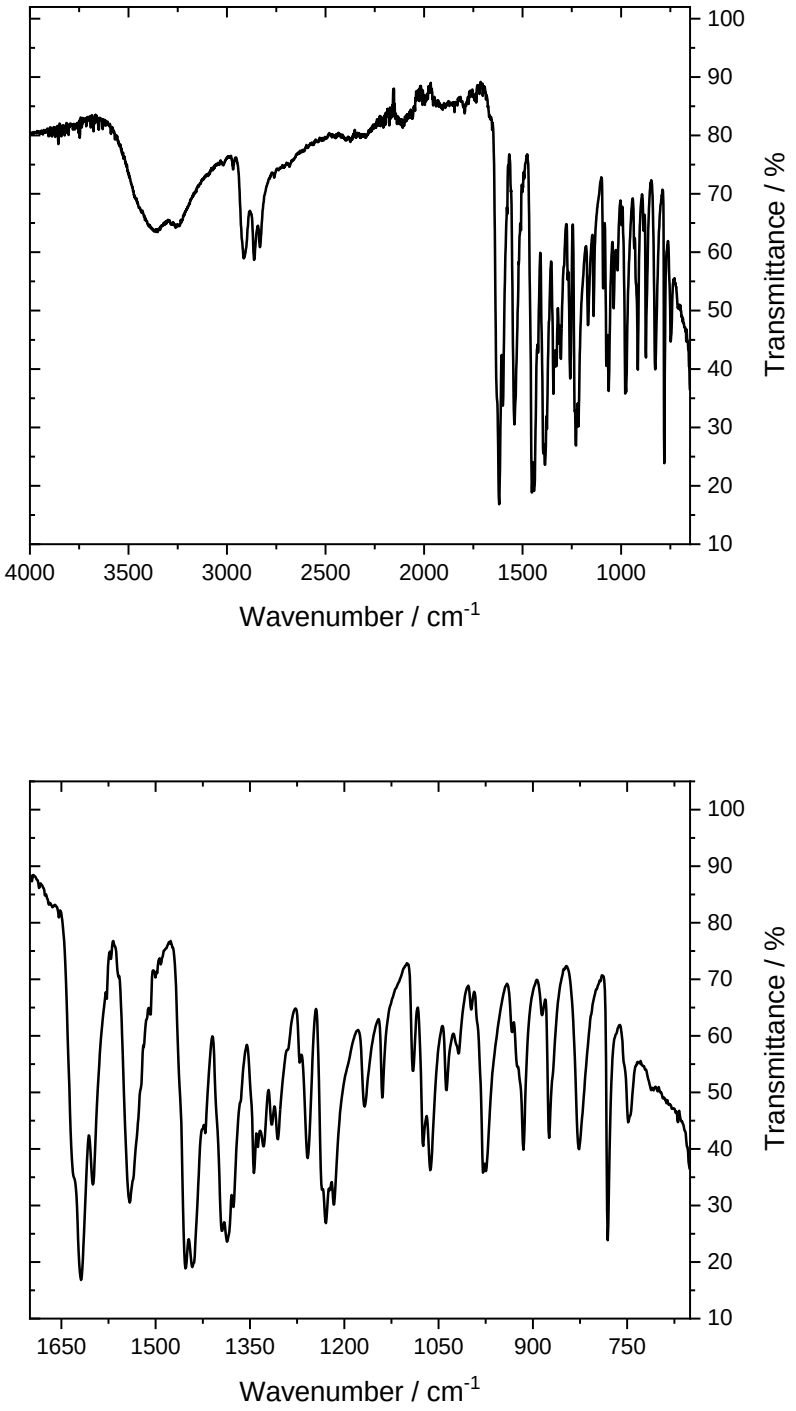

Figure S49. IR spectrum of **LuL·4H$_2$O** full range (top) and enlargement of the region 650-1700 cm^{-1} (bottom).

NMR

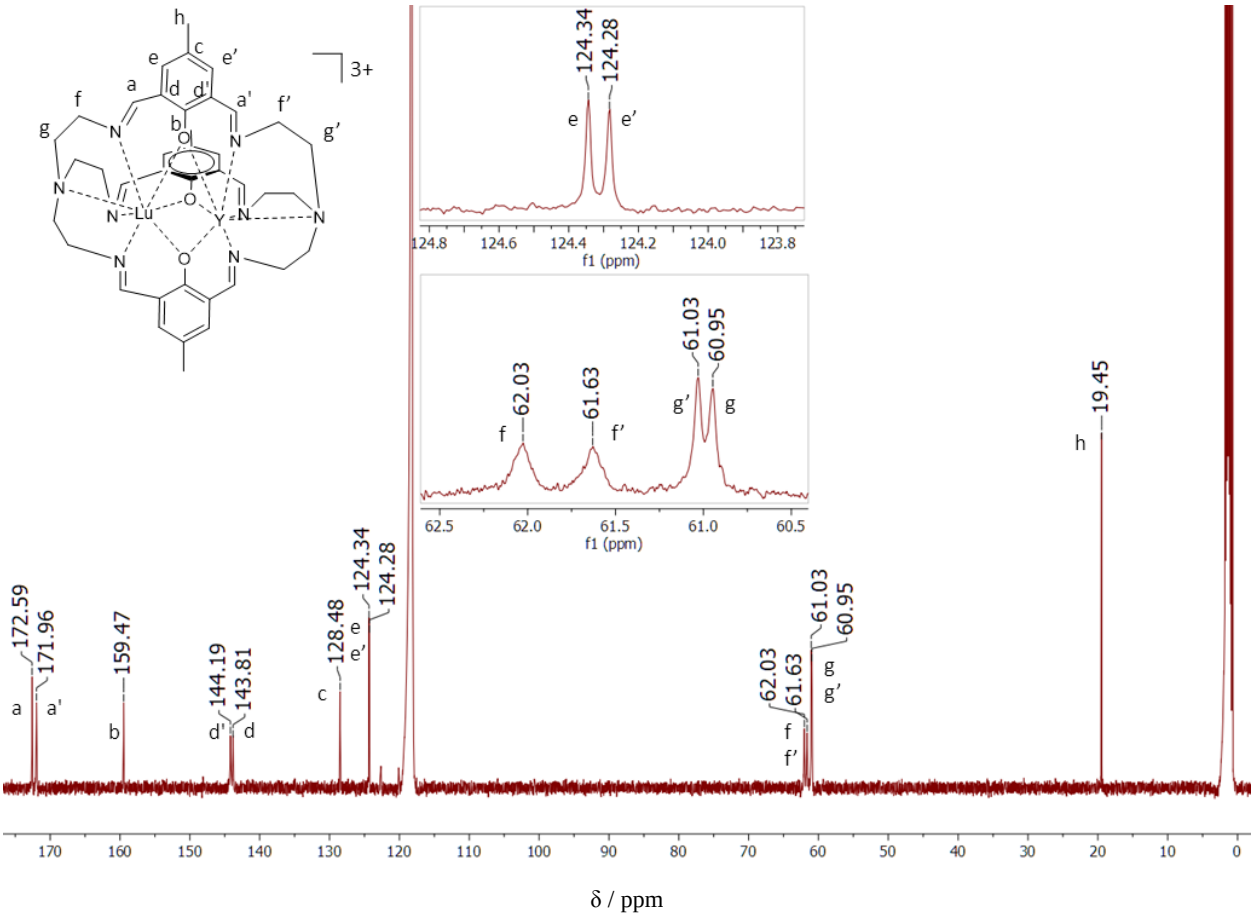

Figure S50. ^{13}C NMR of **6** in CD_3CN. The large signals at 120 and 0 ppm are from CD_3CN. The two inserts are enlargements of the two signals at 124 ppm and the four signals at 62-61 ppm, respectively.

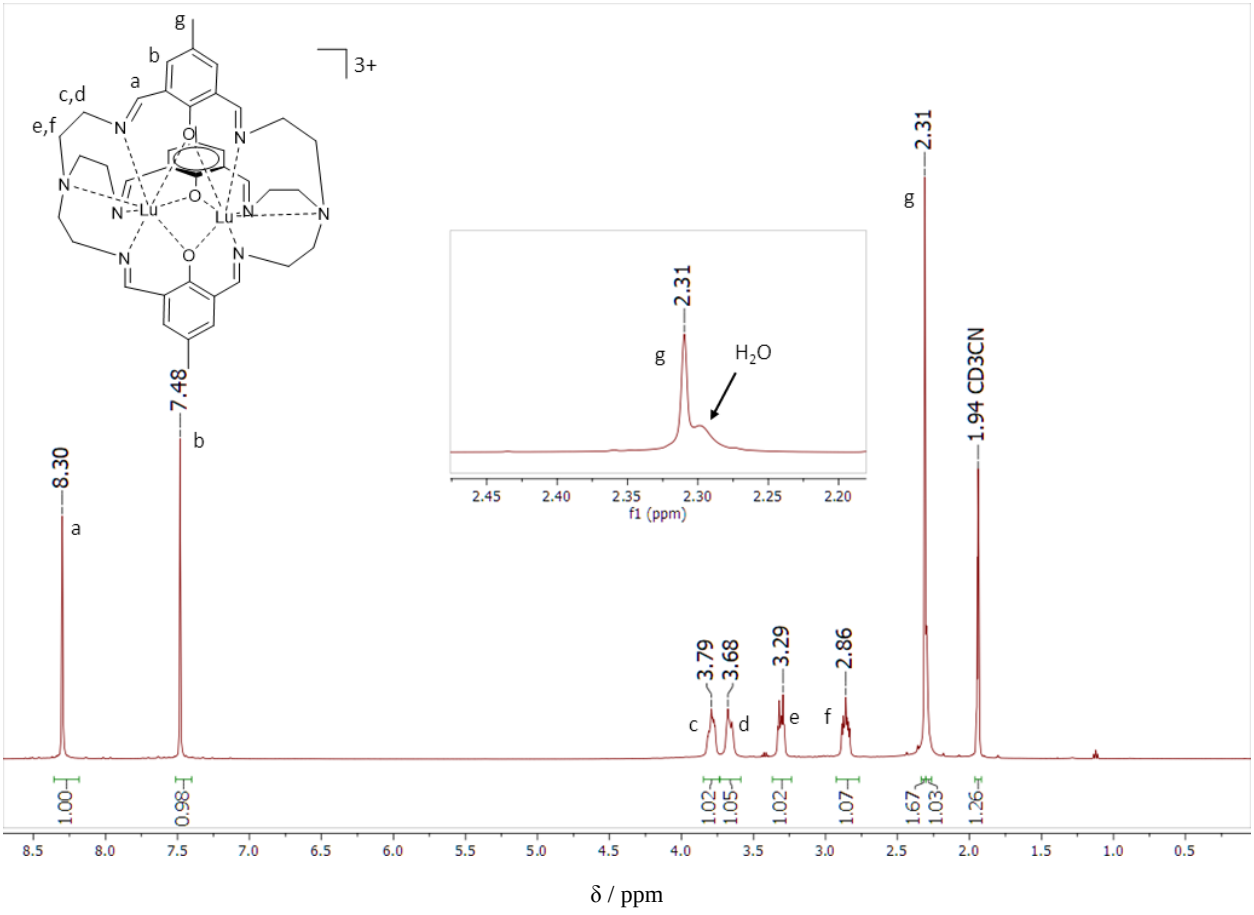

Figure S51. ^{1}H NMR of **7** in CD_3CN.

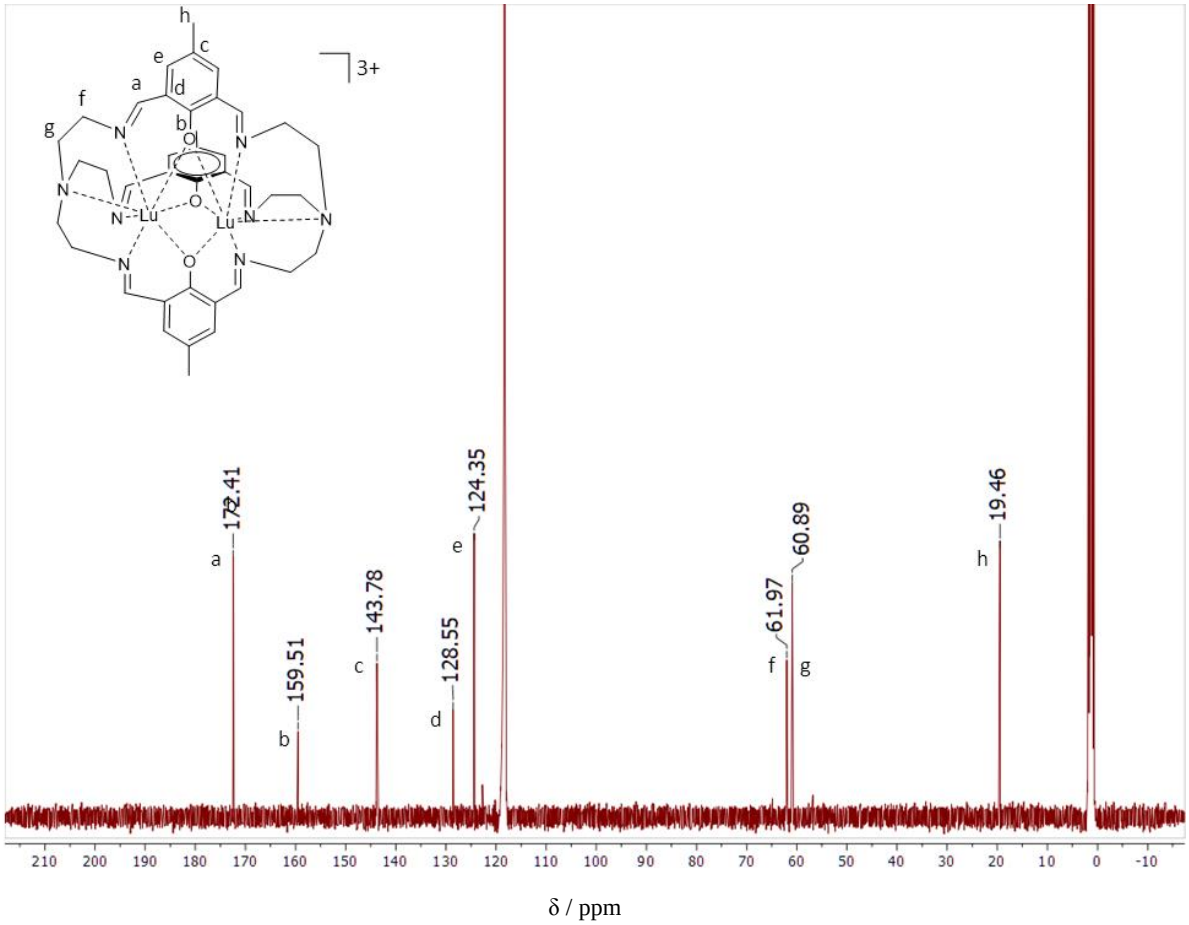

Figure S52. ^{13}C NMR of **7** in CD_3CN. The large signals at 120 and 0 ppm are from CD_3CN.

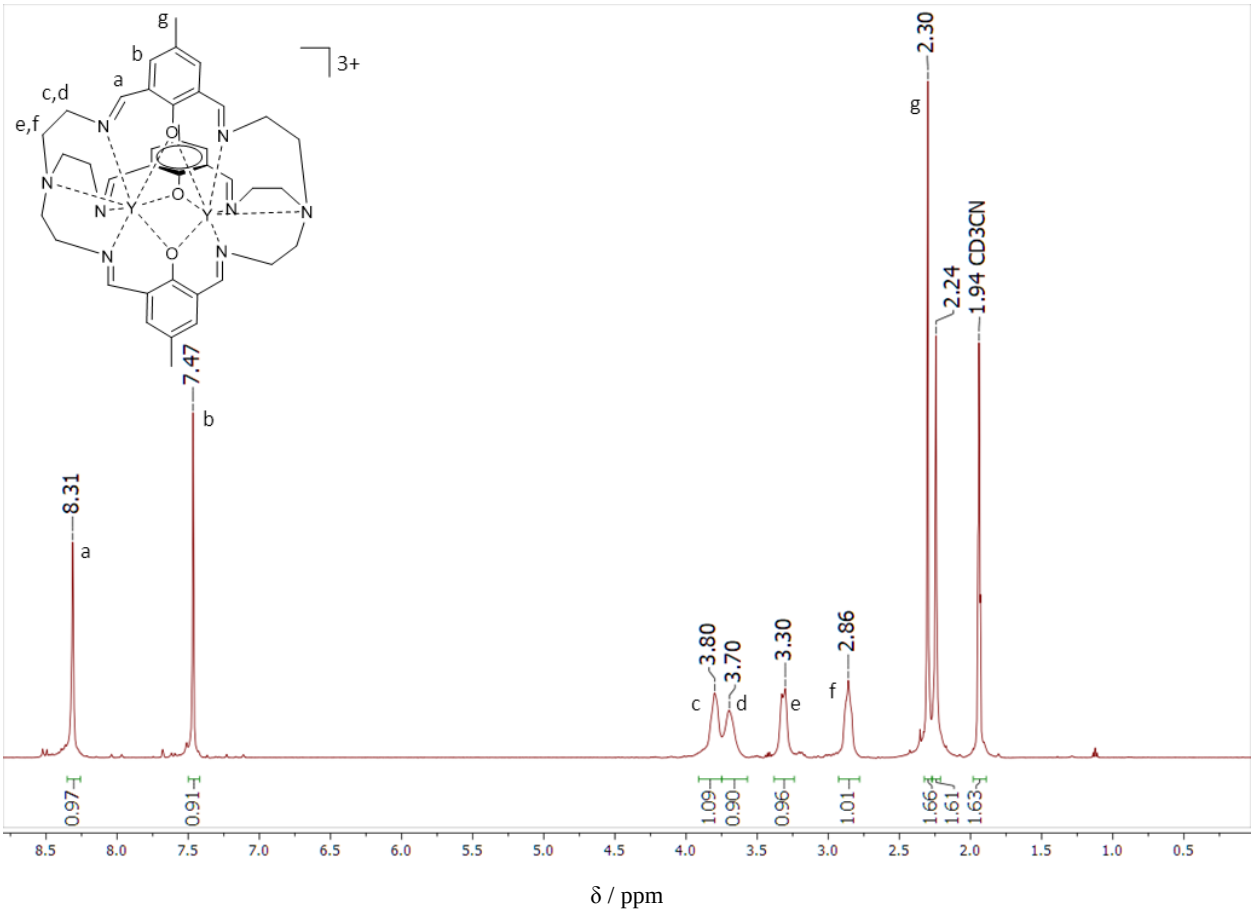

Figure S53. ^{1}H NMR of **9** in CD_3CN.

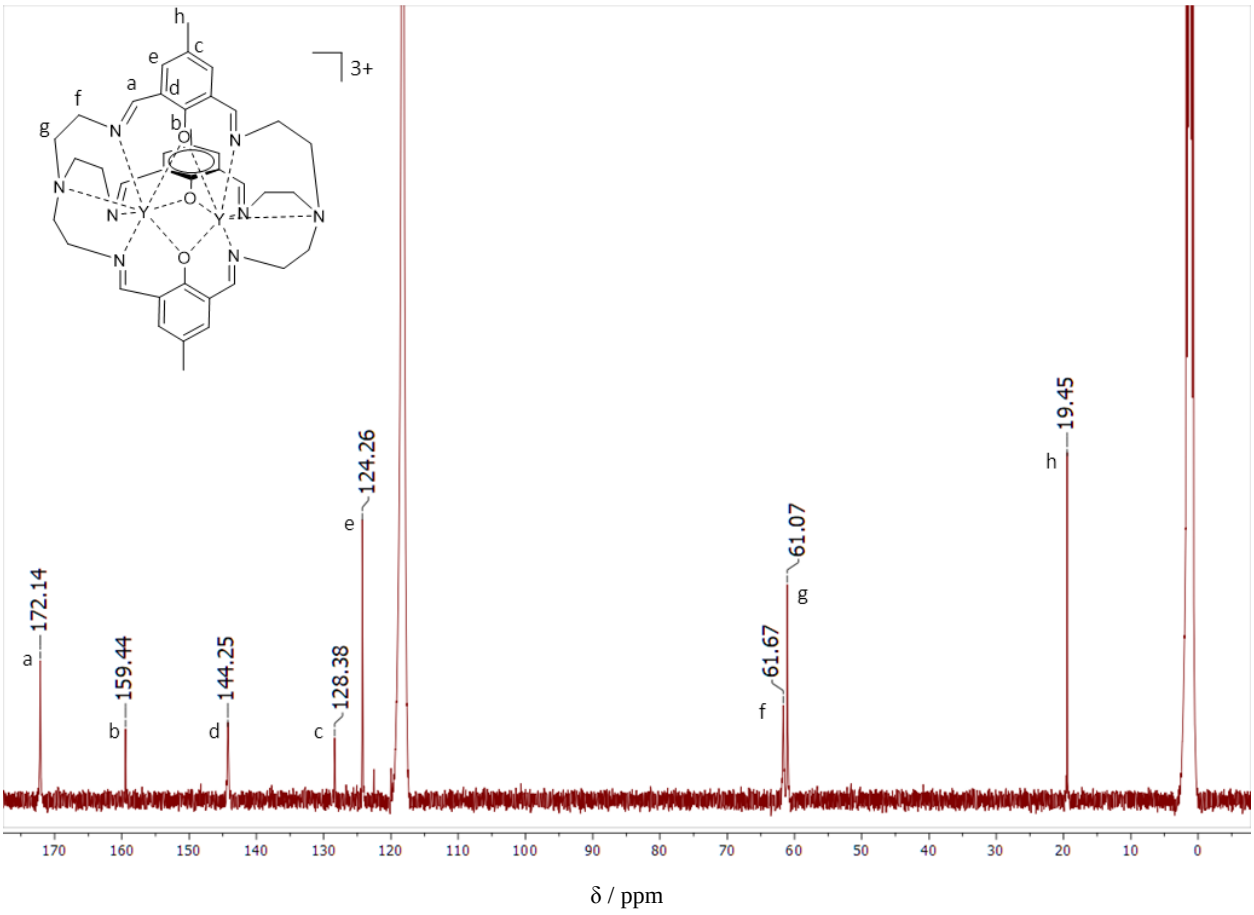

Figure S54. ^{13}C NMR of **9** in CD_3CN. The large signals at 120 and 0 ppm are from CD_3CN.

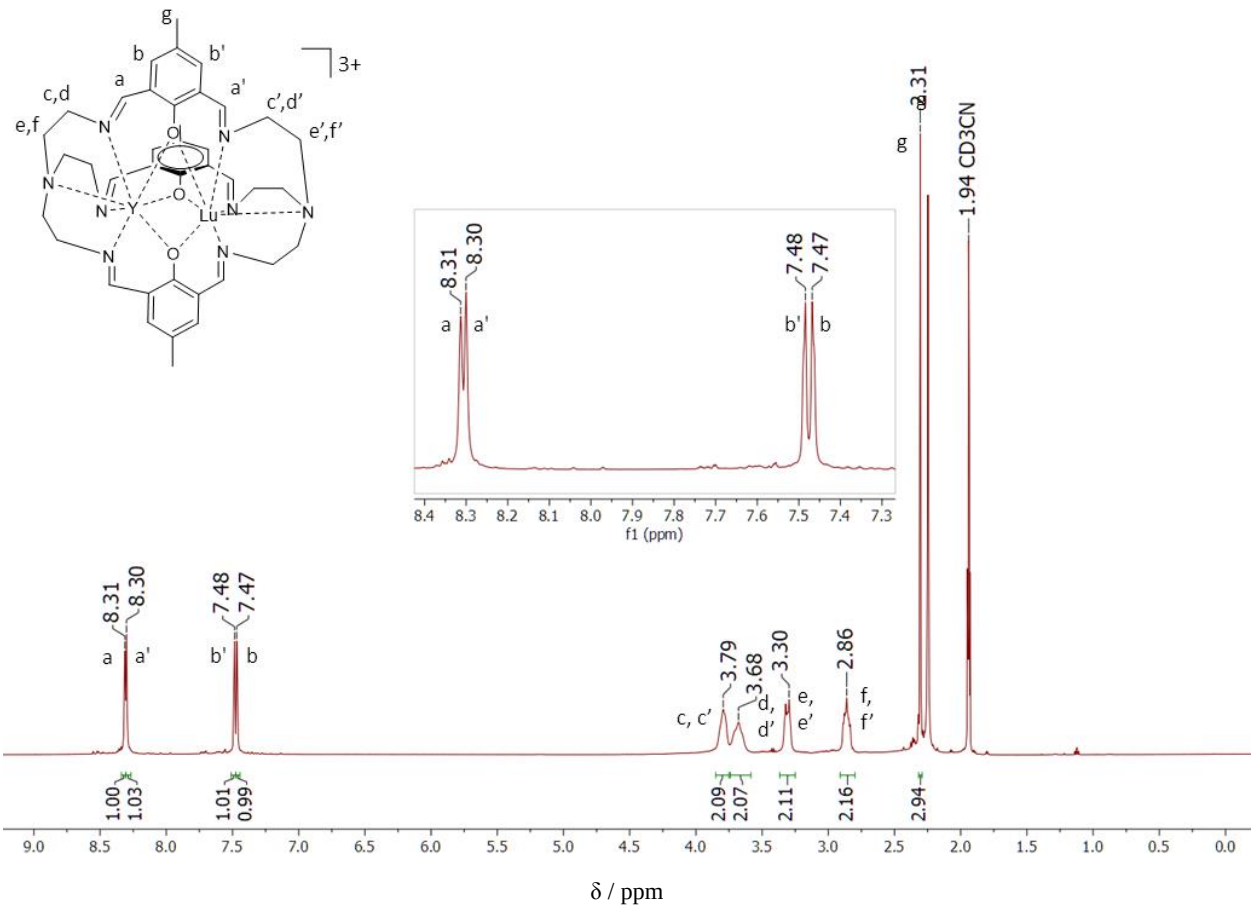

Figure S55. ^{1}H NMR of **6** in CD_3CN. Recorded after 7 days. The large signal at 2.25 ppm is from H_2O. The insert shows an enlargement of the four signals between 8.5-7.3 ppm.

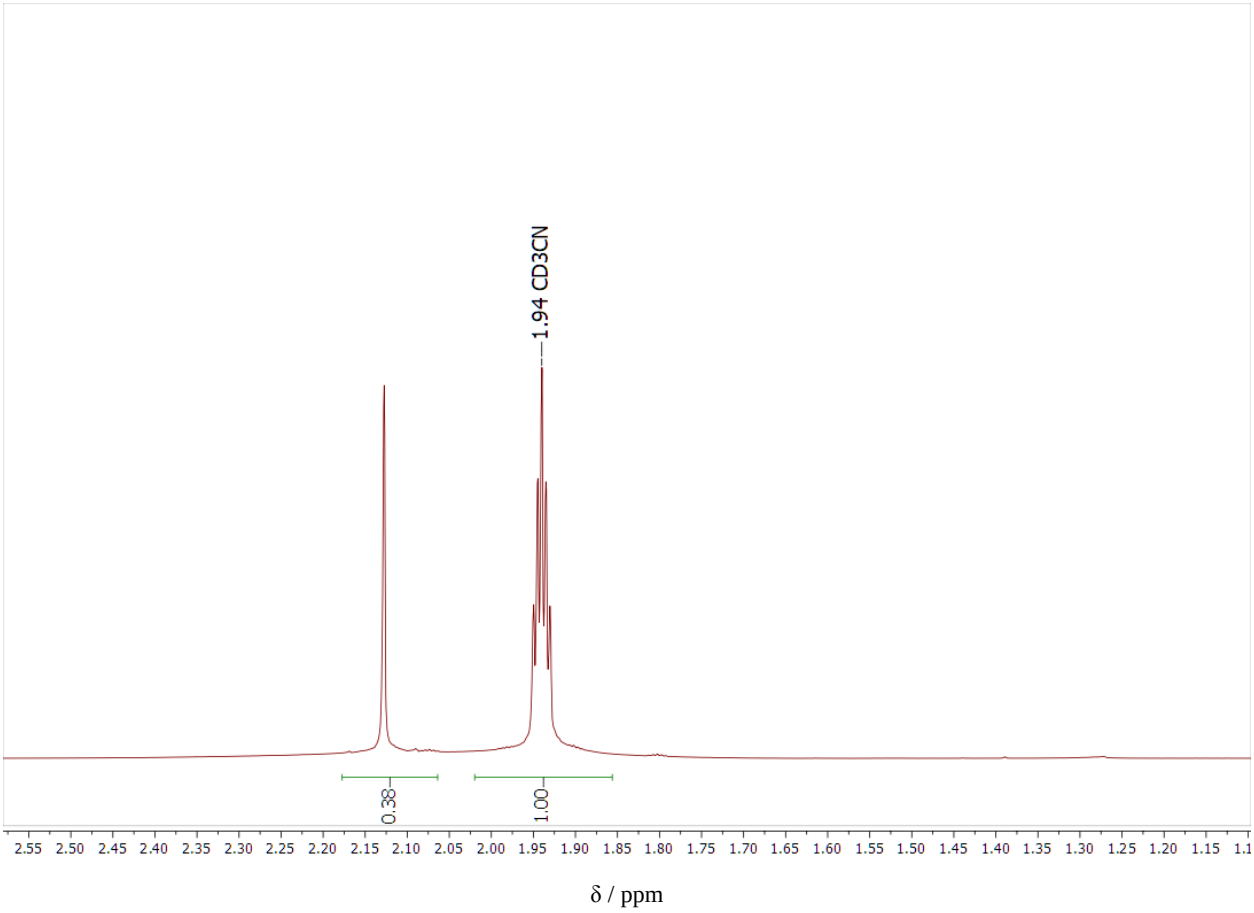

Figure S56. ^{1}H NMR of the CD_3CN used for the above NMR spectra. The large signal at 2.12 ppm is from H_2O.

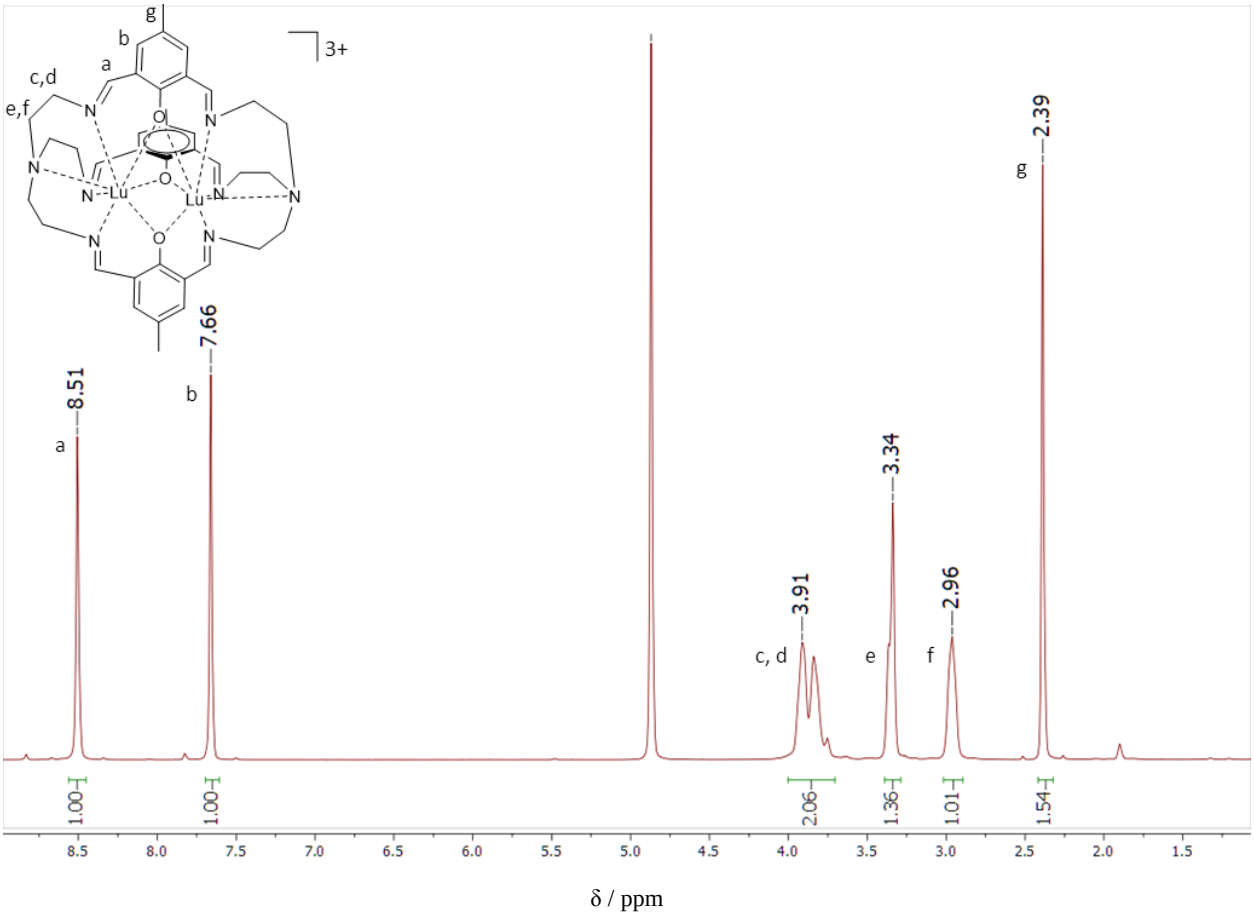

Figure S57. ^{1}H NMR of **7** in CD_3OD. The signal at 4.87 ppm stems from H_2O.

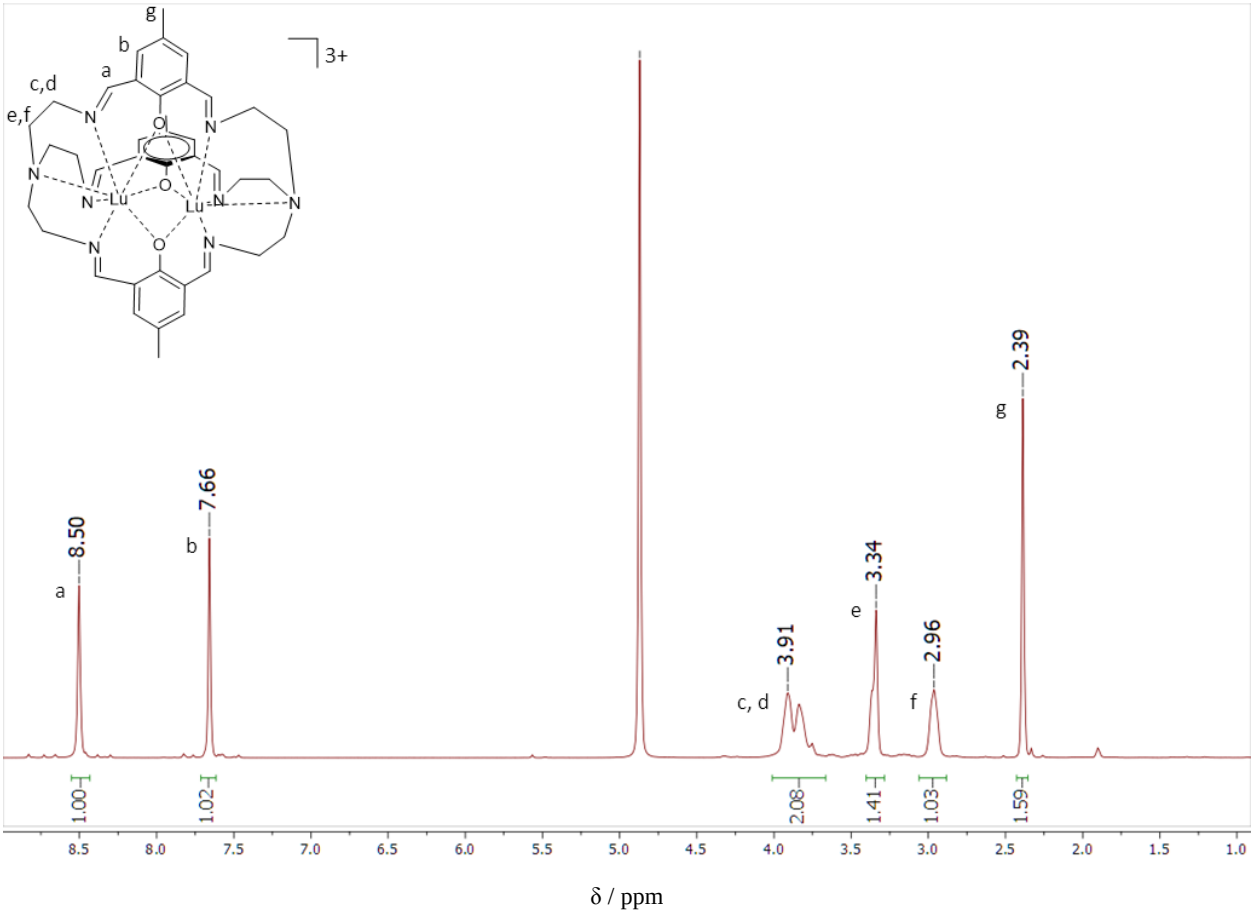

Figure S58. ^{1}H NMR of **7** in CD_3OD recorded after 4 days. The signal at 4.87 ppm stems from H_2O.

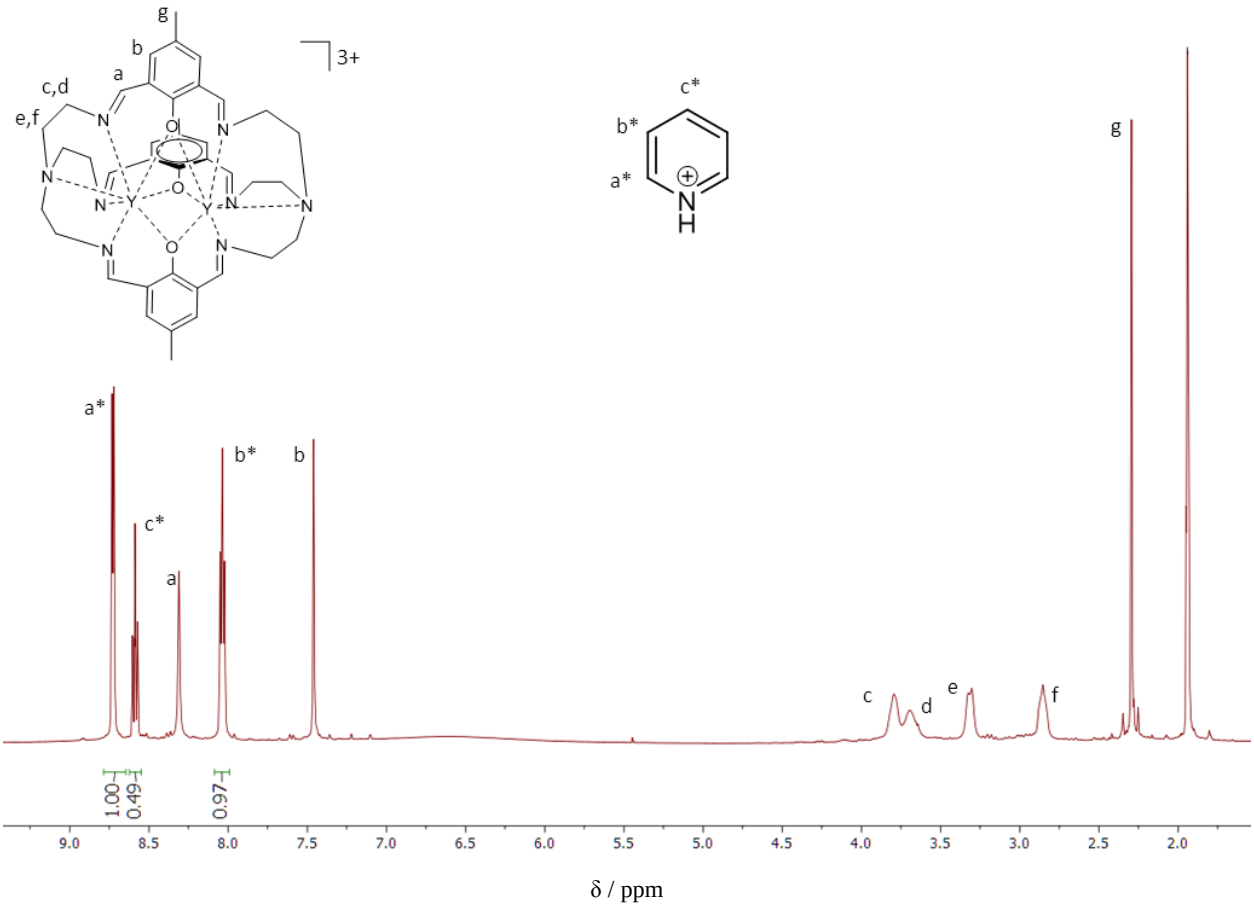

Figure S59. ^{1}H NMR of **9** in CD_3CN before treatment with THF.

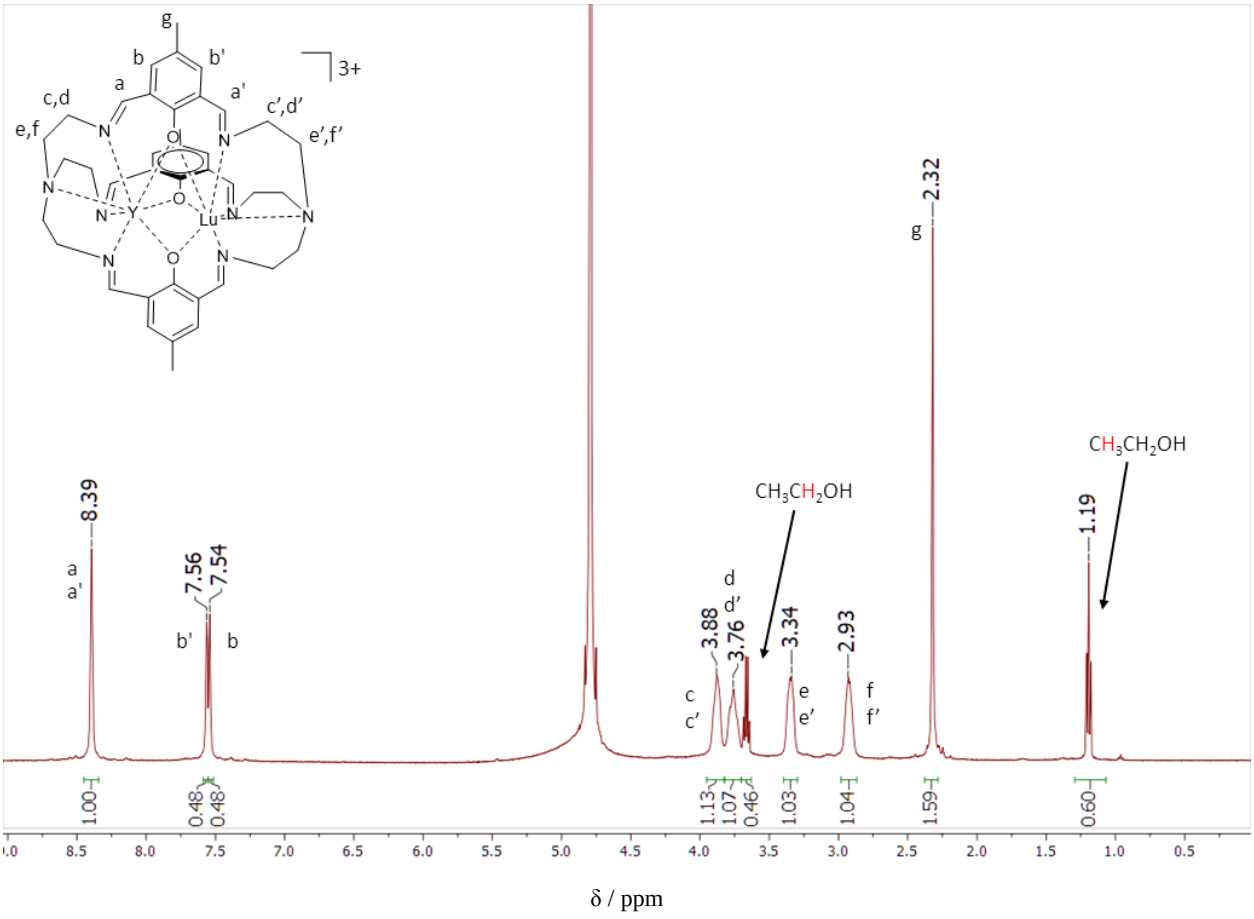

Figure S60. ^{1}H NMR of $\mathbf{6_N}$ in D_2O. The signal at 4.79 ppm is the signal from H_2O.

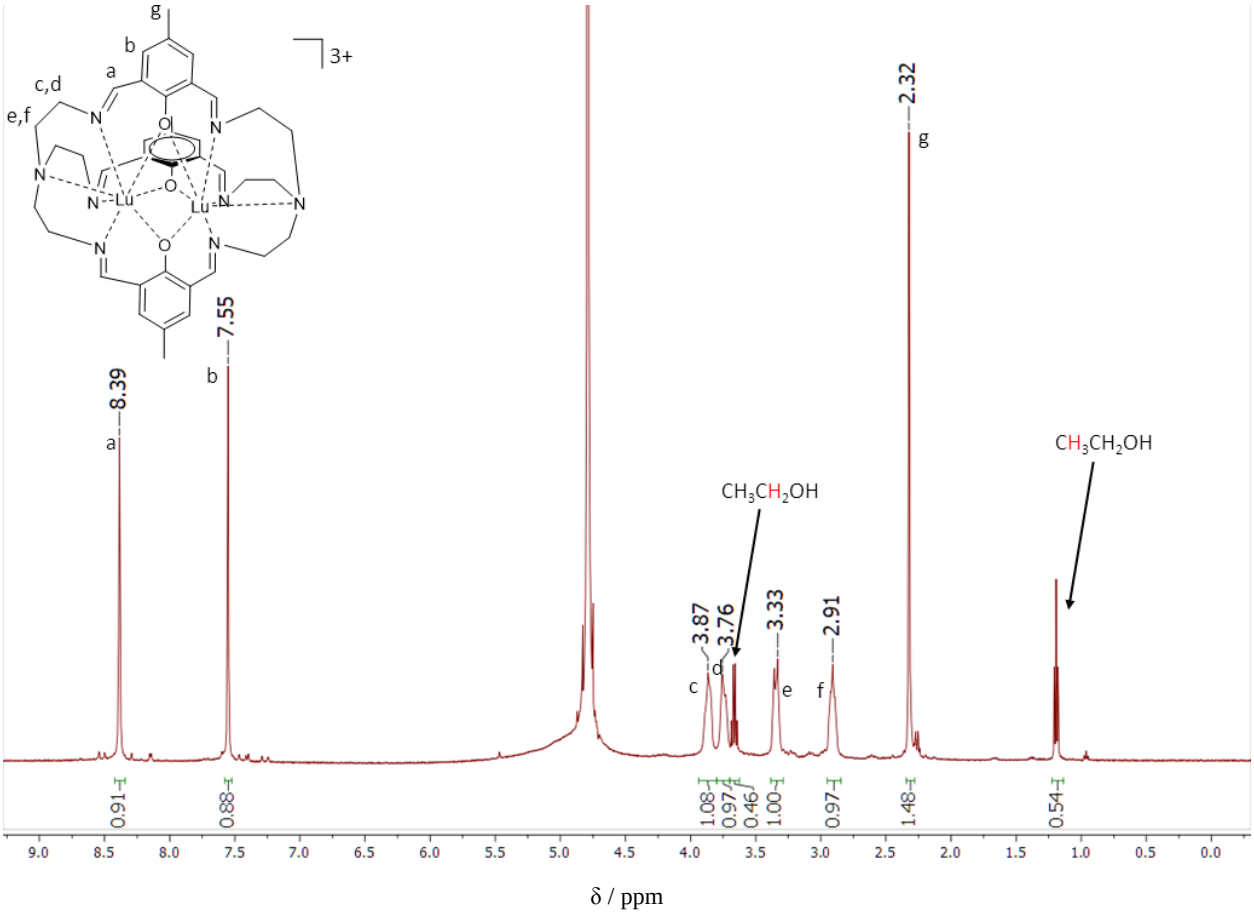

Figure S61. ^{1}H NMR of $\mathbf{7_N}$ in D_2O. The signal at 4.79 ppm is the signal from H_2O.

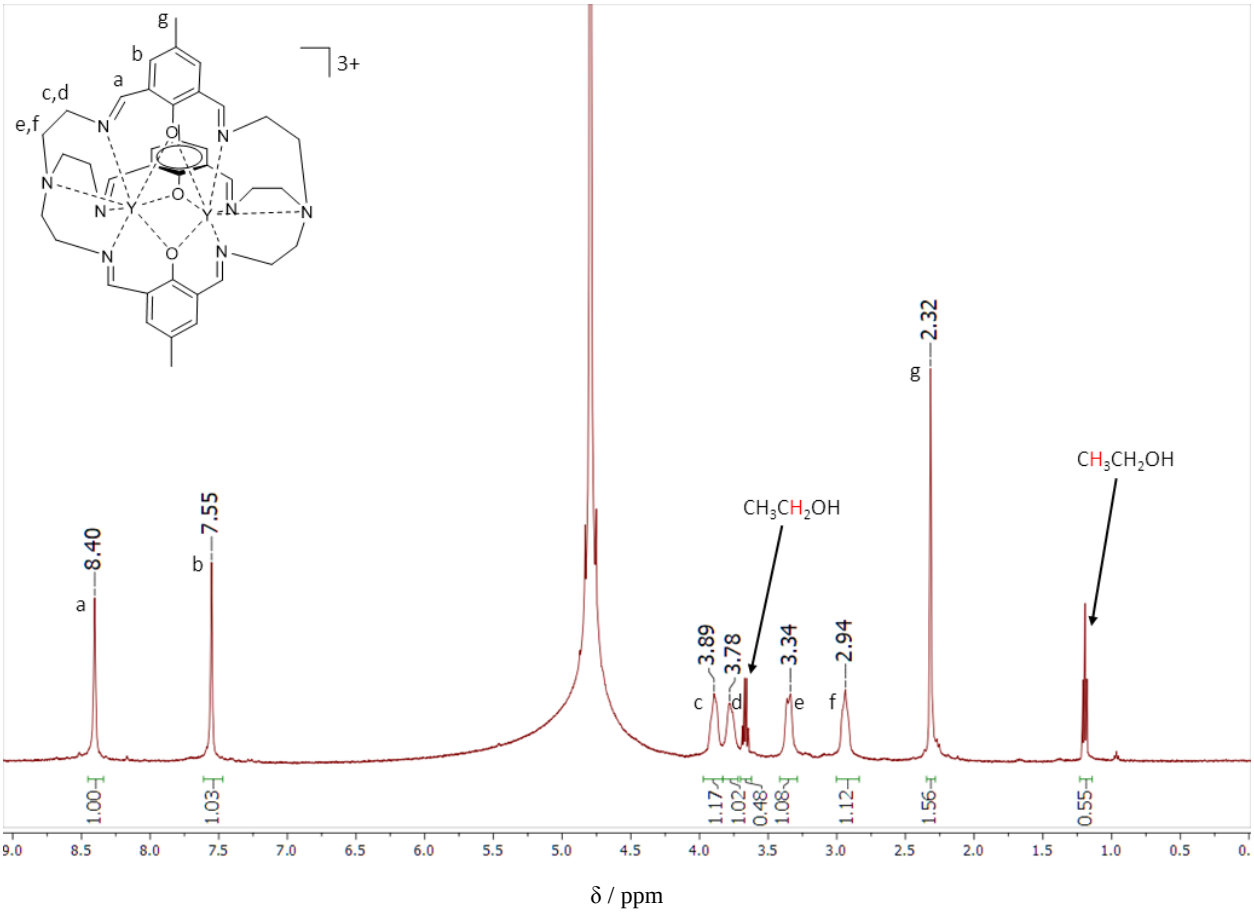

Figure S62. ^{1}H NMR of $\mathbf{9_N}$ in D_2O. The signal at 4.79 ppm is the signal from H_2O.

Powder X-ray diffraction

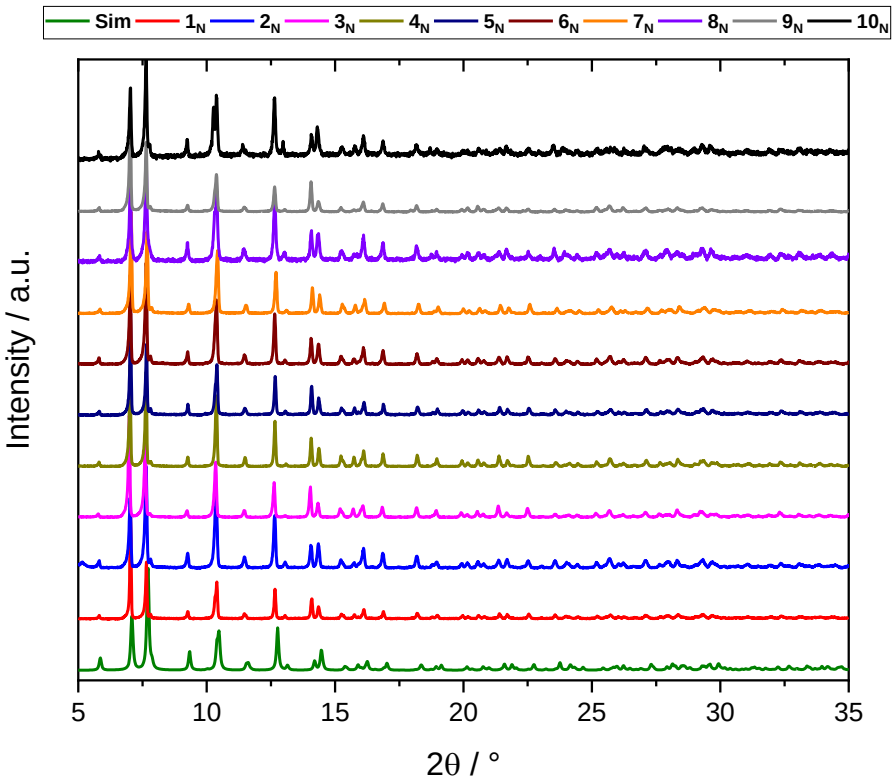

Figure S63. PXRD data for $\mathbf{1_N}$ – $\mathbf{10_N}$. The simulated spectrum is from a crystal structure of $\mathbf{1_N}$

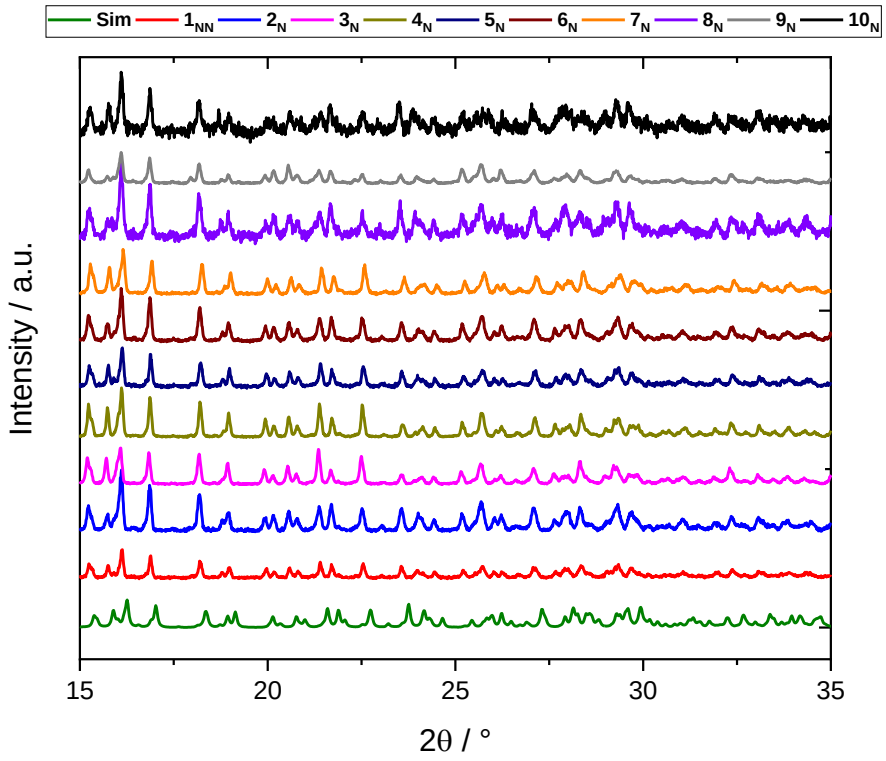

Figure S64. Enlargement of the 2θ 15 - 35° region of the PXRD for $\mathbf{1_N}$ – $\mathbf{10_N}$. The simulated spectrum is from a crystal structure of $\mathbf{1_N}$.

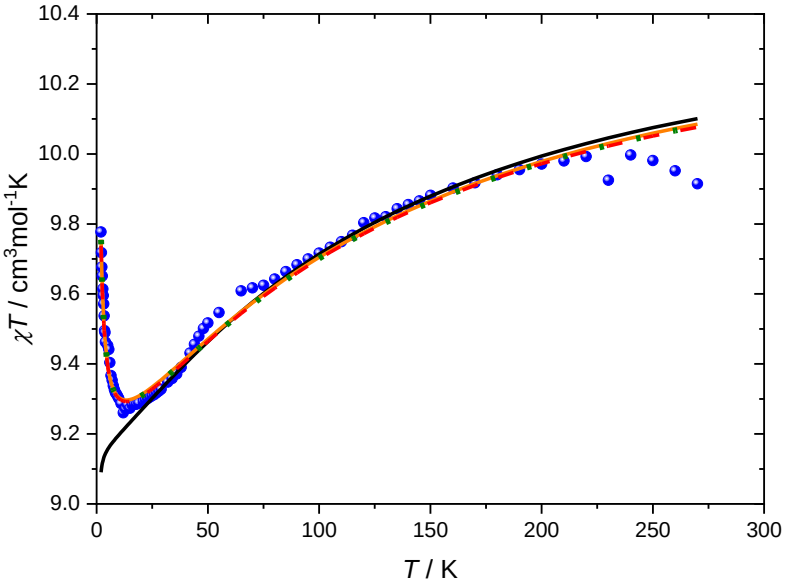

Figure S65. The temperature dependence of the χT product of $\mathbf{1}_N$ (scatter) with the best fit obtained with a model including isotropic exchange and anisotropic exchange (orange), only isotropic exchange (red), only anisotropic exchange (green) and no exchange (black). The fits are based on the CF parameters in **Table S1** and exchange couplings in **Table S3**.

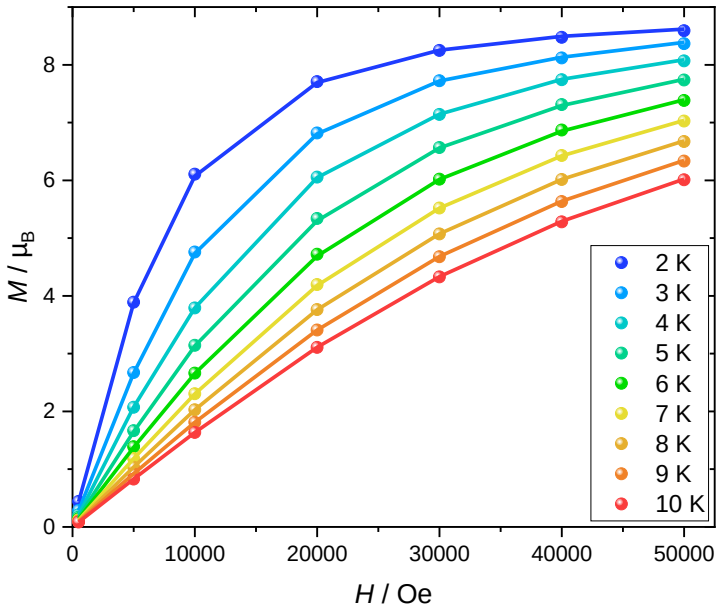

Figure S66. VTVB measurements of $\mathbf{1}_N$ (scatter) including the best fit (lines) obtained with a model including isotropic exchange and anisotropic exchange. The fit is based on the CF parameters in **Table S1** and exchange couplings in **Table S3**.

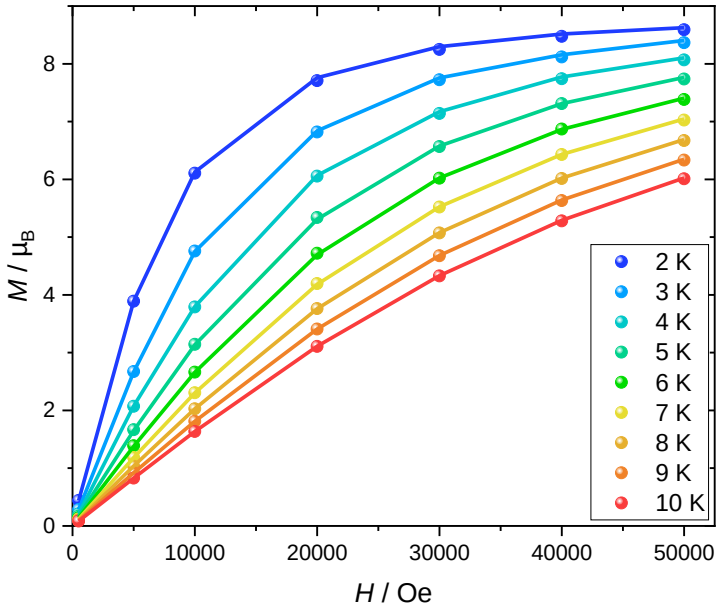

Figure S67. VTVB measurements of $\mathbf{1_N}$ (scatter) including the best fit (lines) obtained with a model including isotropic exchange. The fit is based on the CF parameters in **Table S1** and exchange couplings in **Table S3**.

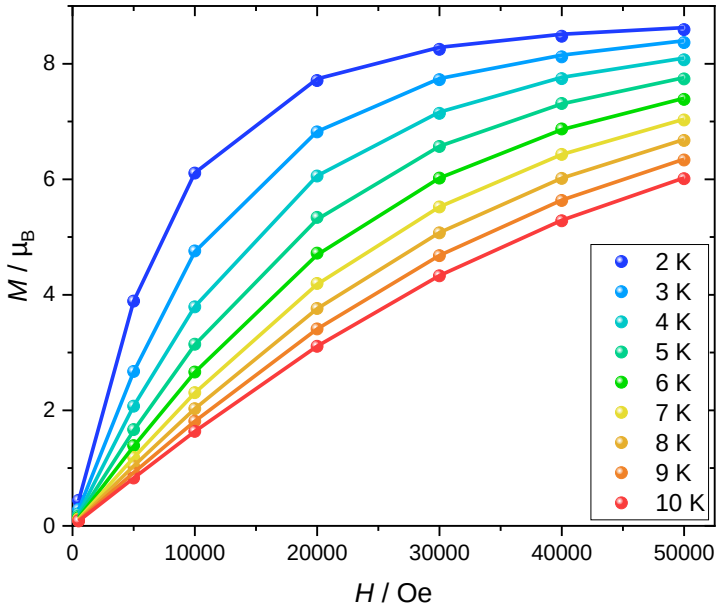

Figure S68. VTVB measurements of $\mathbf{1_N}$ (scatter) including the best fit (lines) obtained with a model including anisotropic exchange. The fit is based on the CF parameters in **Table S1** and exchange couplings in **Table S3**.

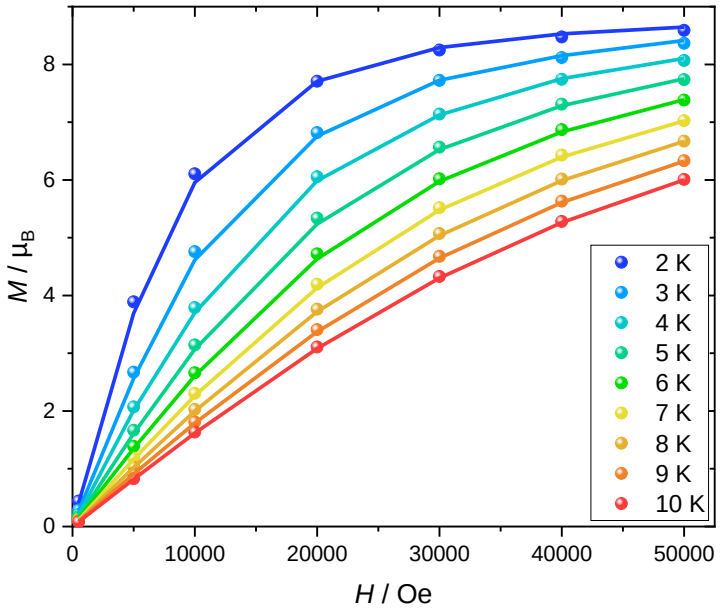

Figure S69. VTVB measurements of $\mathbf{1_N}$ (scatter) including the best fit (lines) obtained with a model with no exchange. The fit is based on the CF parameters in **Table S1**.

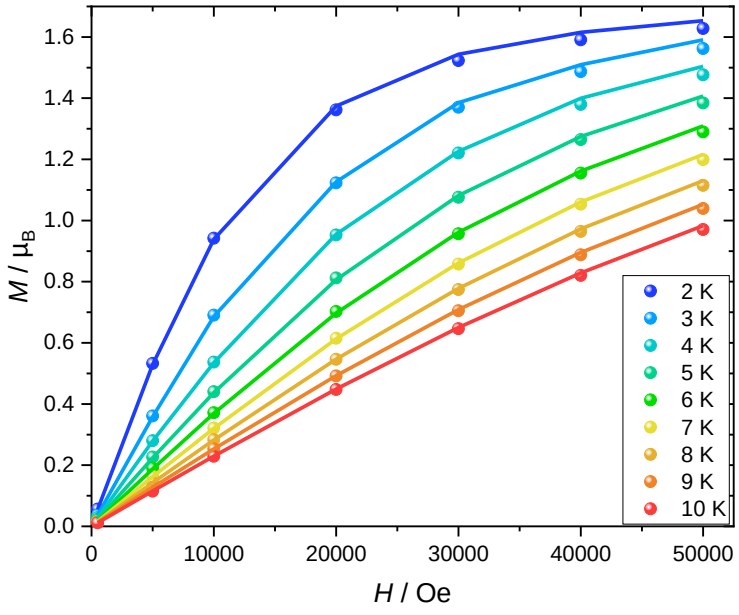

Figure S70. VTVB measurements of $\mathbf{2_N}$ (scatter) including the best fit (lines) obtained with the model described in the main text. The CF parameters can be found in **Table S1**.

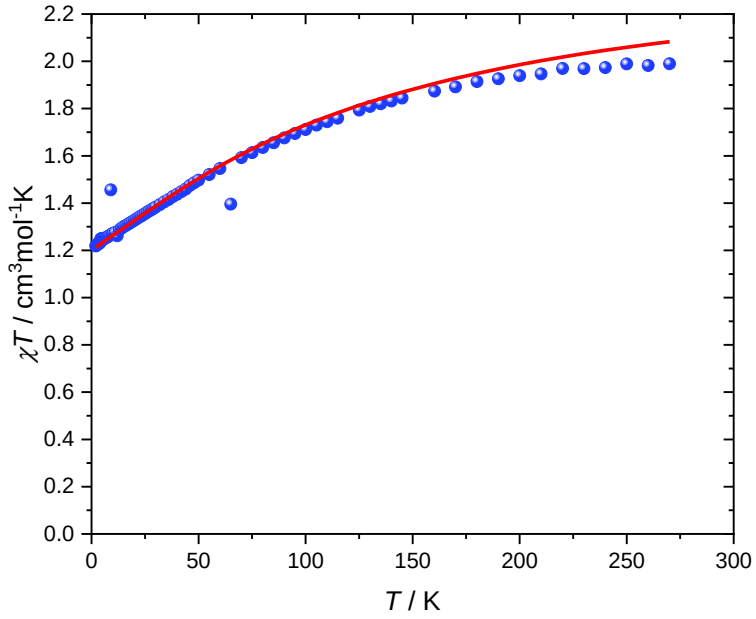

Figure S71. Temperature dependence of the χT product of $\mathbf{3_N}$ (scatter) with the best fit (line) obtained with the model described in the main text. The CF parameters can be found in **Table S1**.

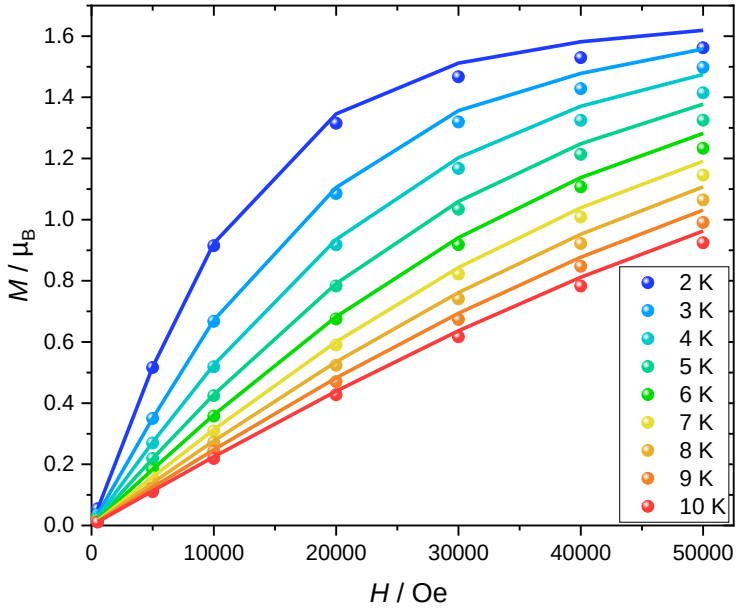

Figure S72. VTVB measurements of $\mathbf{3_N}$ (scatter) including the best fit (lines) obtained with the model described in the main text. The CF parameters can be found in **Table S1**.

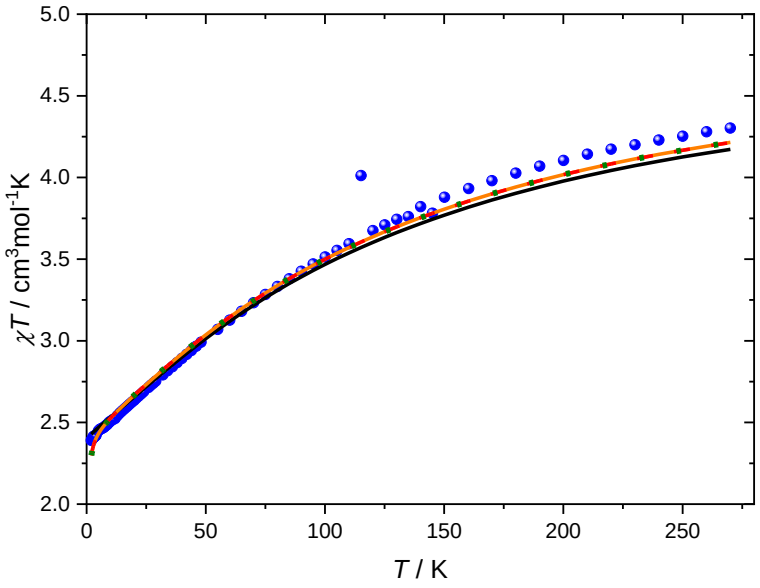

Figure S73. Temperature dependence of the χT product of $\mathbf{4_N}$ (scatter) with the best fit obtained with a model including isotropic exchange and anisotropic exchange (orange), only isotropic exchange (red), only anisotropic exchange (green) and no exchange (black). The fits are based on the CF parameters in **Table S1** and exchange couplings in **Table S3**.

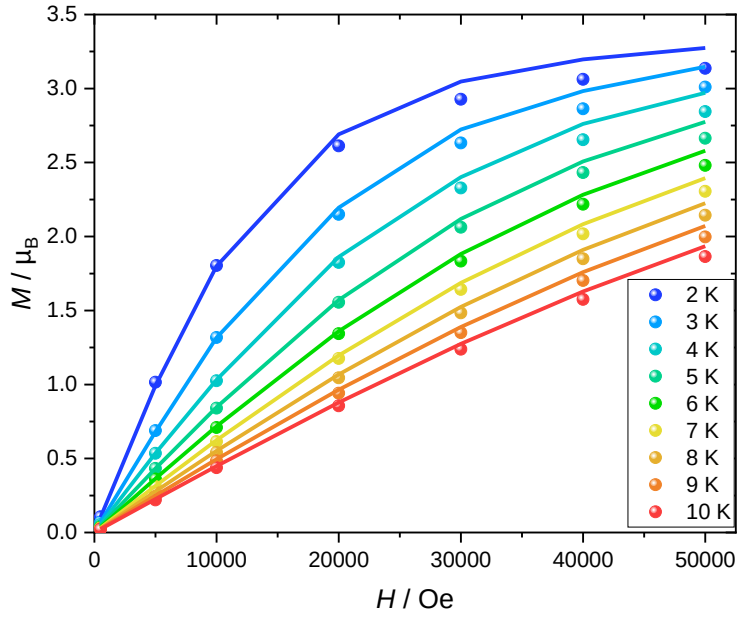

Figure S74. VTVB measurements of $\mathbf{4_N}$ (scatter) including the best fit (lines) obtained with a model including isotropic exchange and anisotropic exhcange. The fit is based on the CF parameters in **Table S1** and exchange couplings in **Table S3**.

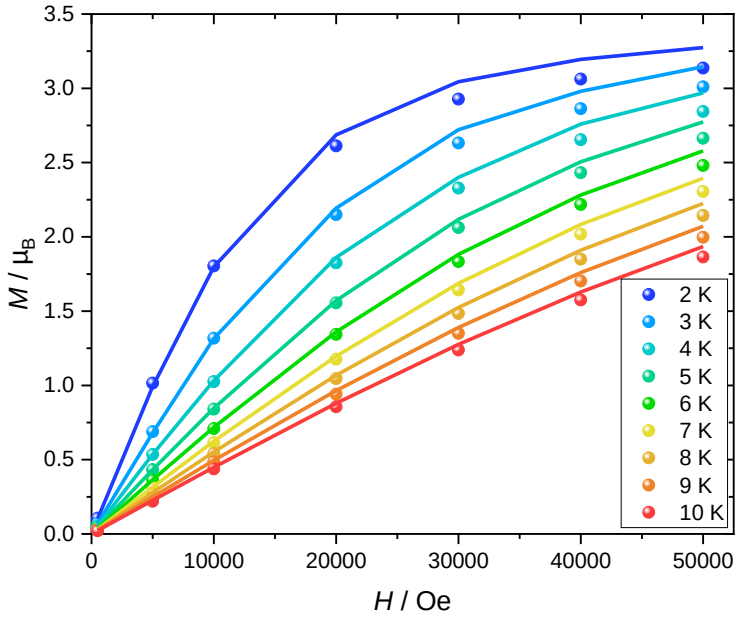

Figure S75. VTVB measurements of $\mathbf{4_N}$ (scatter) including the best fit (lines) obtained with a model including isotropic exchange. The fit is based on the CF parameters in **Table S1** and exchange couplings in **Table S3**.

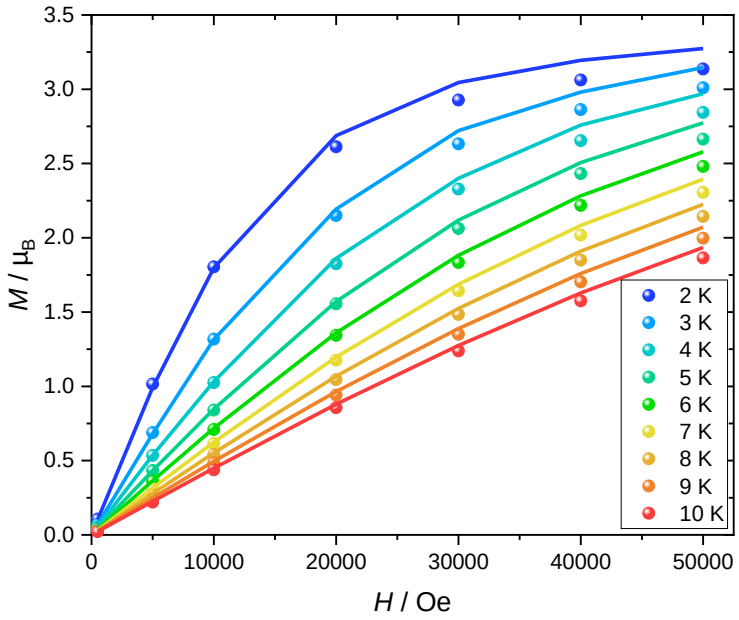

Figure S76. VTVB measurements of $\mathbf{4_N}$ (scatter) including the best fit (lines) obtained with a model including anisotropic exchange. The fit is based on the CF parameters in **Table S1** and exchange couplings in **Table S3**.

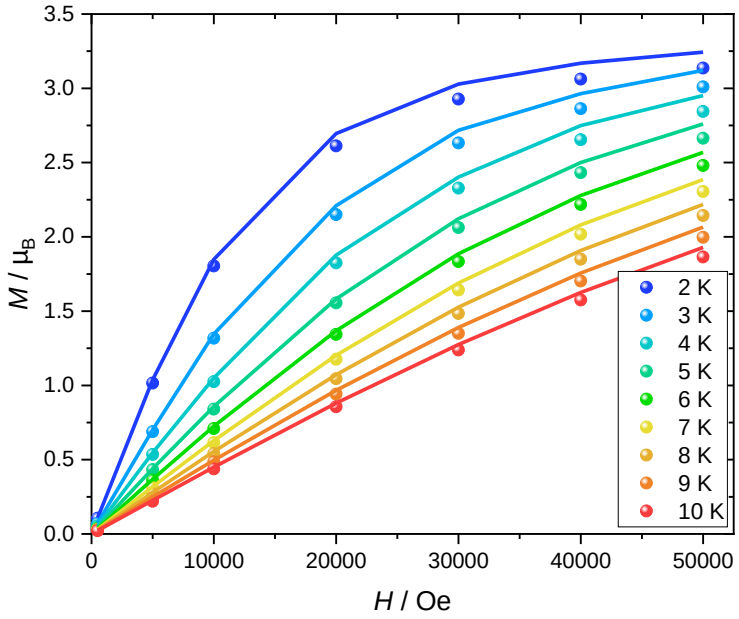

Figure S77. VTVB measurements of $\mathbf{4_N}$ (scatter) including the best fit (lines) obtained with a model including no exchange. The fit is based on the CF parameters in **Table S1**.

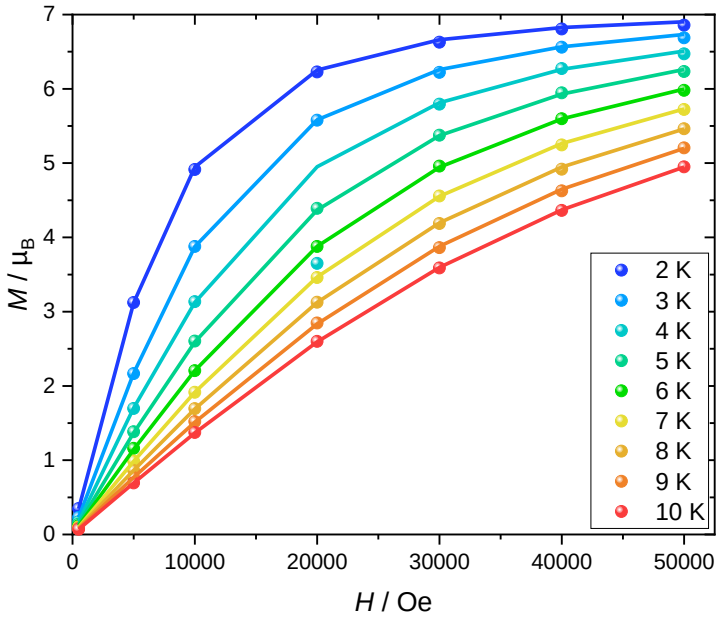

Figure S78. VTVB measurements of $\mathbf{5_N}$ (scatter) including the best fit (lines) obtained with the model described in the main text. The CF parameters can be found in **Table S1**.

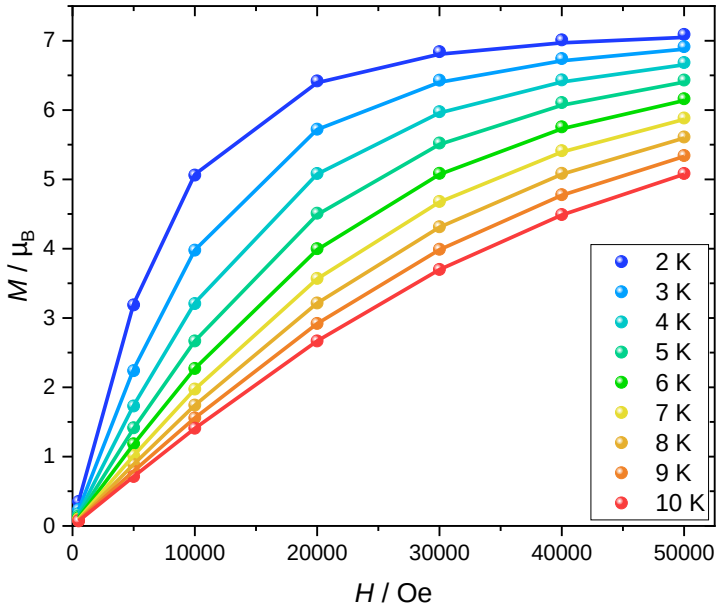

Figure S79. VTVB measurements of $\mathbf{8}_{\mathbf{N}}$ (scatter) including the best fit (lines) obtained with the model described in the main text. The CF parameters can be found in **Table S1**.

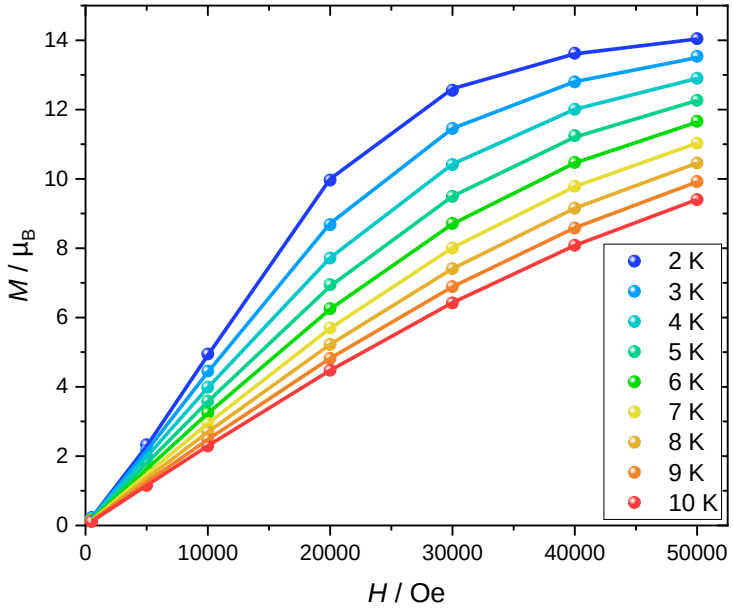

Figure S80. VTVB measurements of $\mathbf{10}_{\mathbf{N}}$ (scatter) including the best fit (lines) obtained with the model described in the main text.

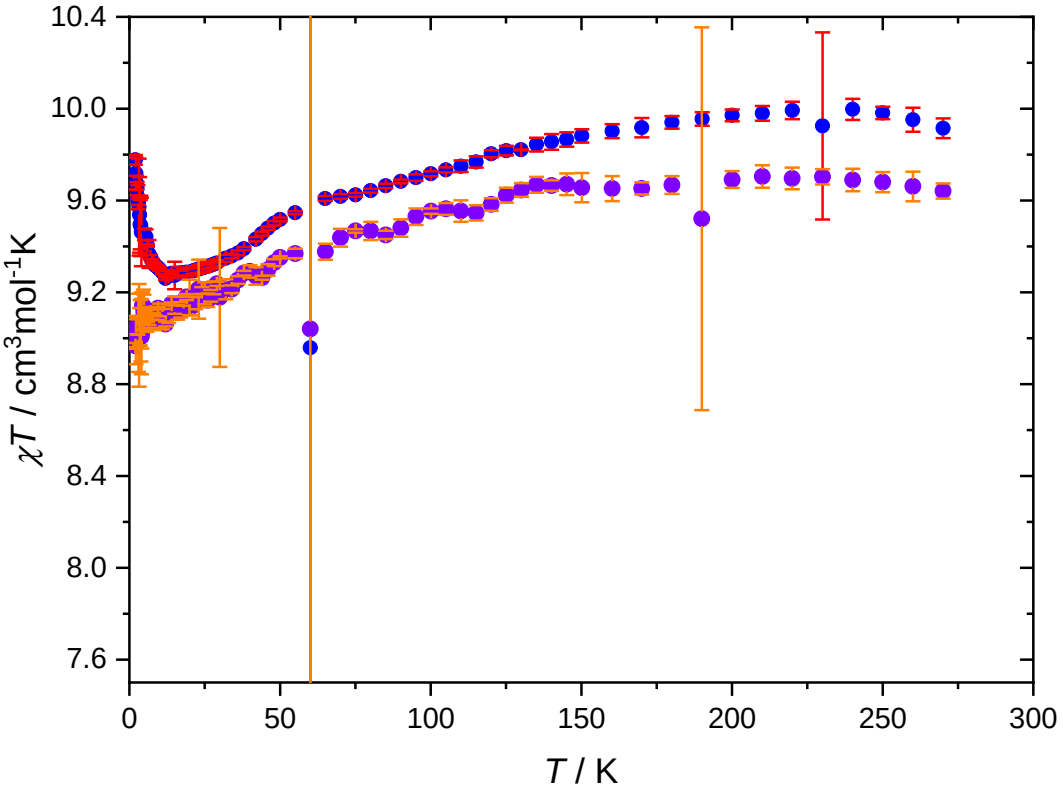

Figure S81. Temperature dependence of the χT product of $\mathbf{1_N}$ (blue scatter with error bars in red) and temperature dependence of the sum of the χT products of $\mathbf{2_N}$ and $\mathbf{5_N}$ (purple scatter with error bars in orange). Error bars correspond to the 3σ (99.7%) confidence interval.

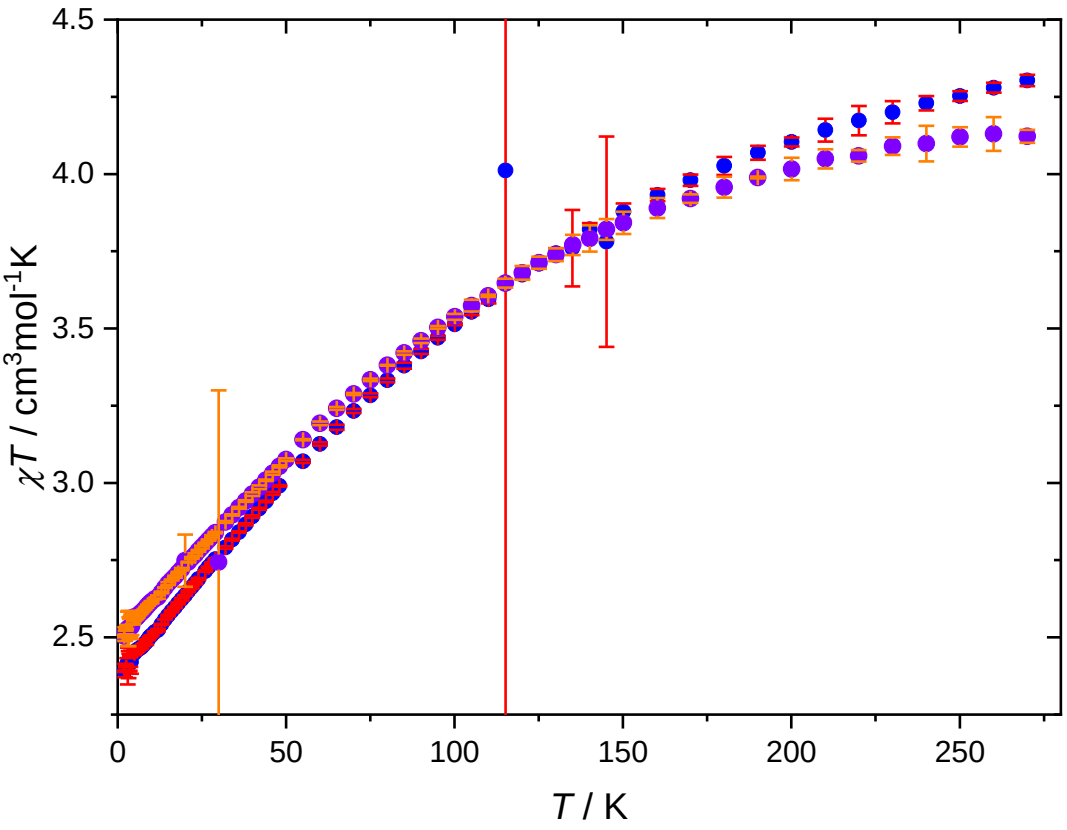

Figure S82. Temperature dependence of the χT product of $\mathbf{4}_{\mathbf{N}}$ (blue scatter with error bars in red) and temperature dependence of the χT product $\mathbf{2}_{\mathbf{N}}$ scaled by a factor of 2 (purple scatter with error bars in orange). Error bars correspond to the 3σ (99.7%) confidence interval.

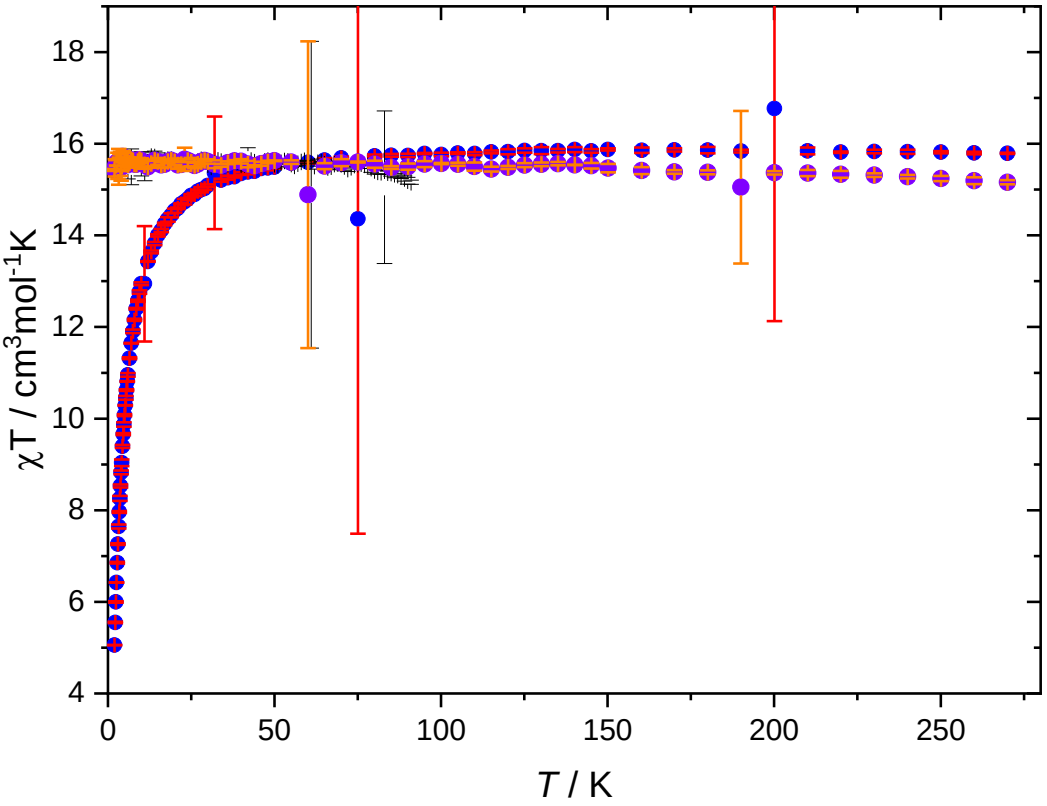

Figure S83. Temperature dependence of the χT product of $\mathbf{10}_{\mathbf{N}}$ (blue scatter with error bars in red) and temperature dependence of the χT product $\mathbf{5}_{\mathbf{N}}$ scaled by a factor of 2 (purple scatter with error bars in orange). Error bars correspond to the 3σ (99.7%) confidence interval.

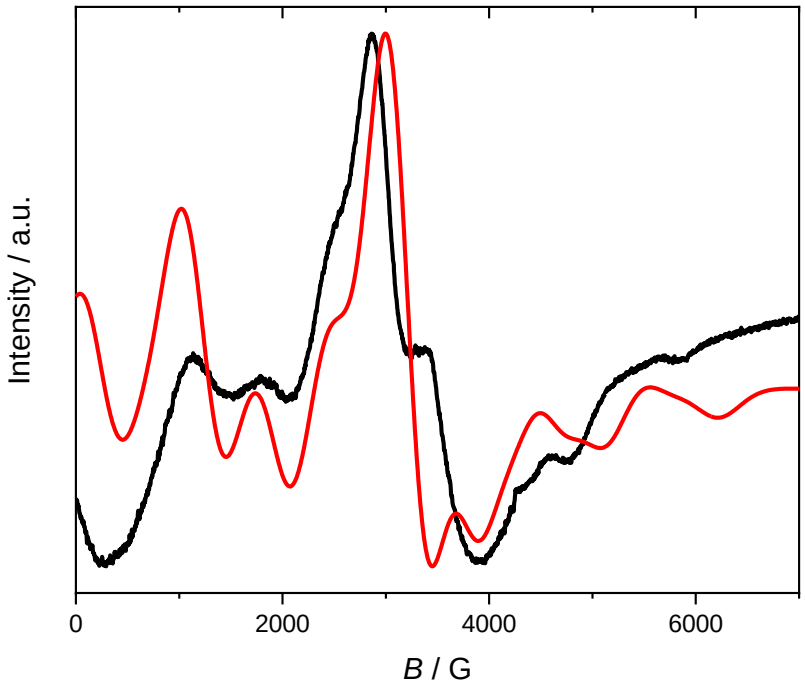

Figure S84. X-band cw EPR spectrum of $\mathbf{5_N}$ (black) including a simulation (red) based on the parameters in **Table S1**. The spectrum was recorded at 300 K. In the simulation linewidth broadening (40 G) and *D* strain were used.

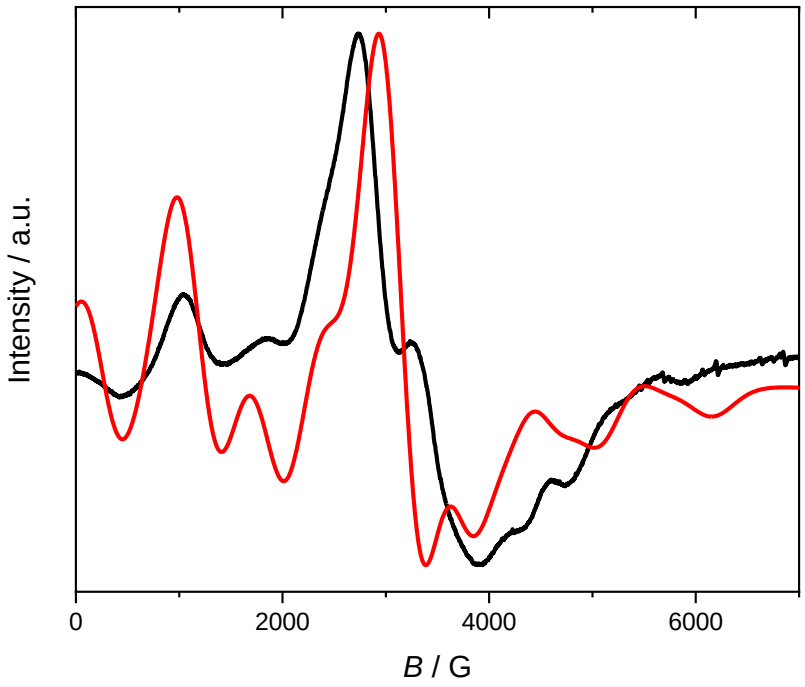

Figure S85. X-band cw EPR spectrum of $\mathbf{8_N}$ (black) including a simulation (red) based on the parameters in **Table S1**. The spectrum was recorded at 300 K. In the simulation linewidth broadening (40 G) and *D* strain were used.

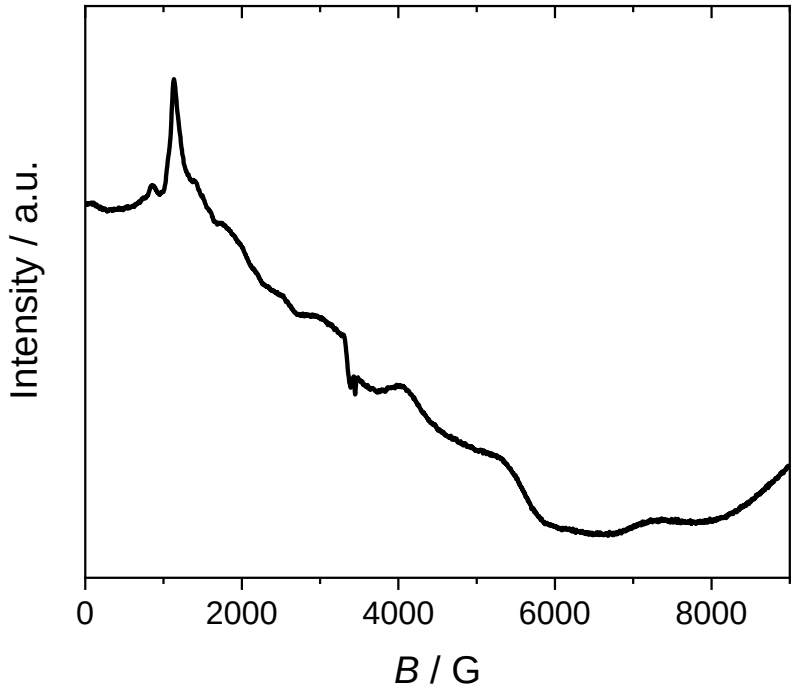

Figure S86. X-band cw EPR spectrum of **3_N'** recorded at 19 K.

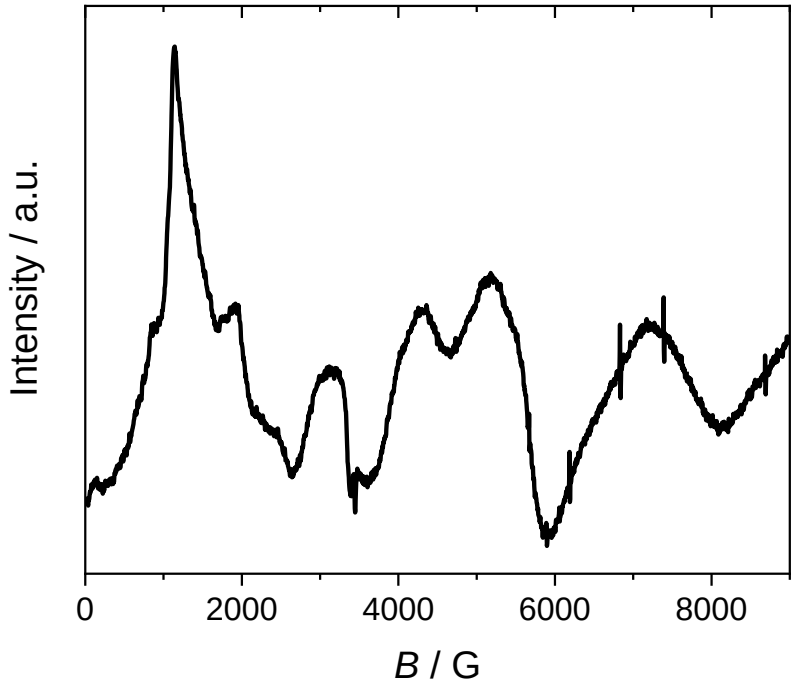

Figure S87. X-band cw EPR spectrum of **2_N'** recorded at 18 K.

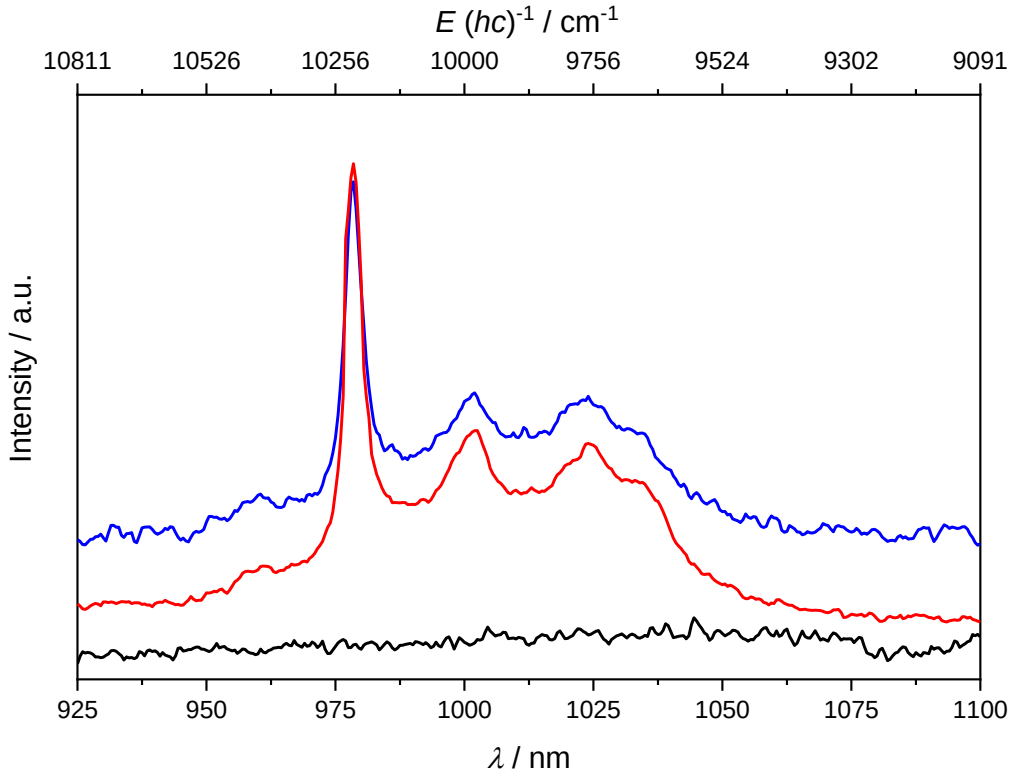

Figure S88. Emission spectra at 300 K of $\mathbf{9}_{N}$ (black), $\mathbf{2}_{N}$**'** (red) and $\mathbf{3}_{N}$**'** (blue). For the spectra an excitation wavelength of 380 nm was used, this was based on the excitation spectrum of $\mathbf{9}_{N}$, Figure S89.

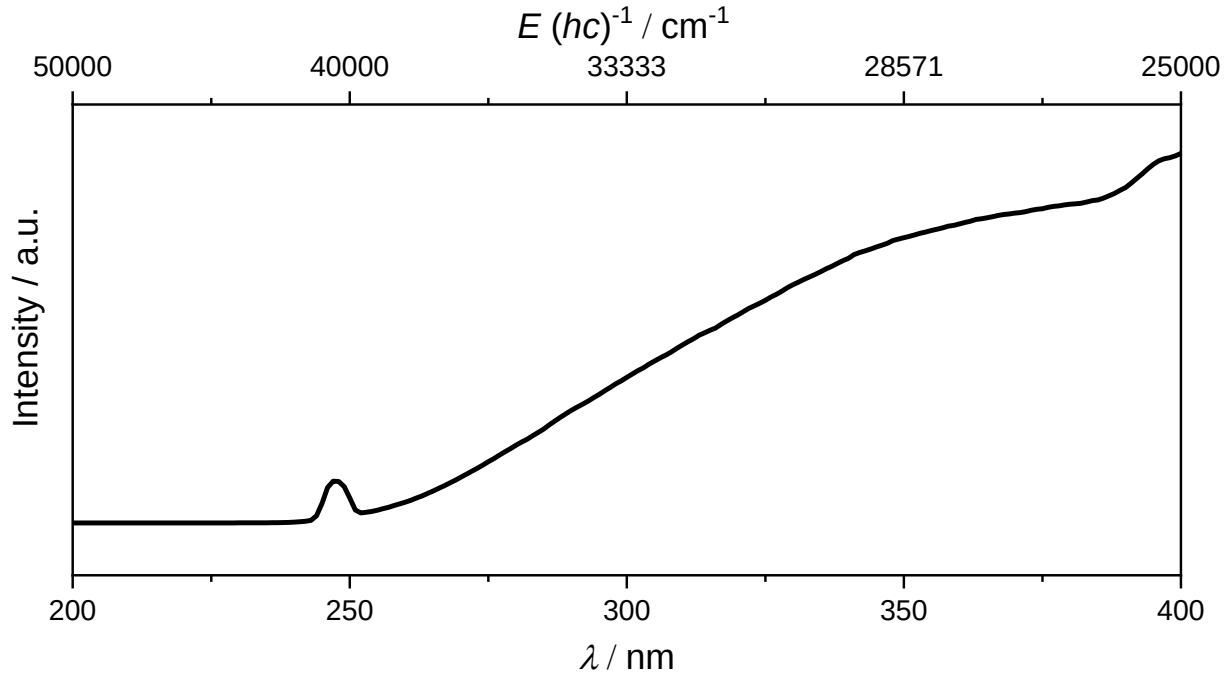

Figure S89. Excitation spectrum of $\mathbf{9}_{N}$ measured at 300 K with emission detected at 500 nm. The detection of the emission was chosen to where the ligand emits the most, Figure S90.

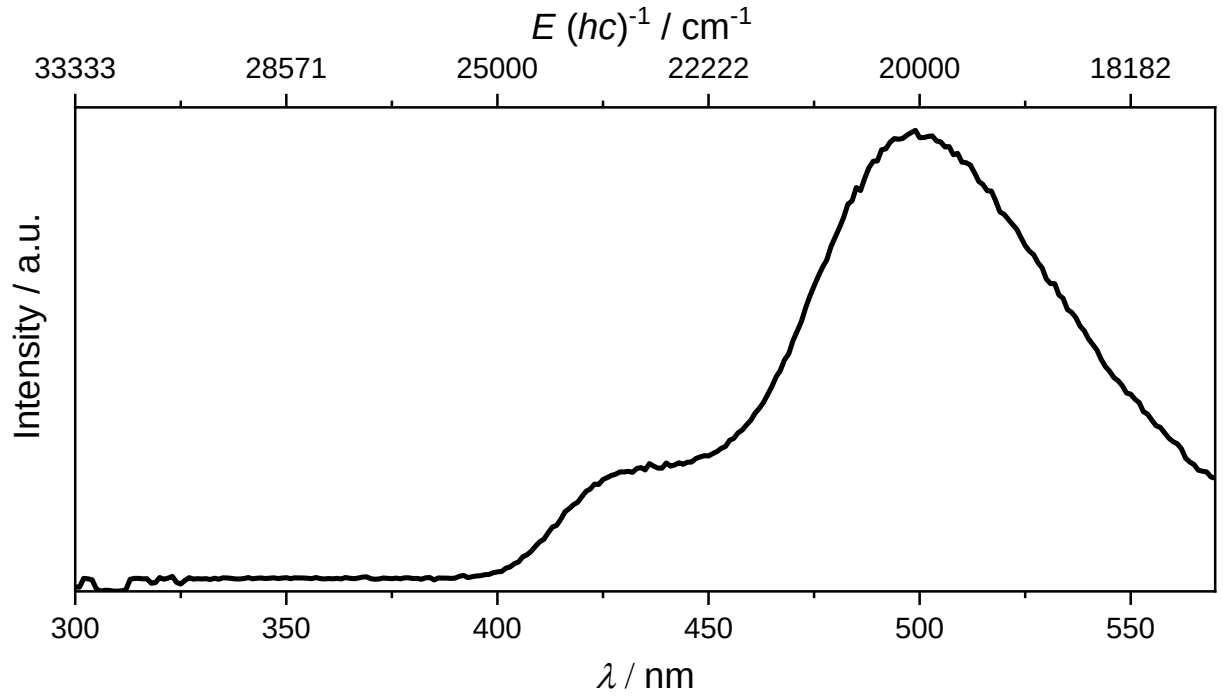

Figure S90. Emission spectrum of $\mathbf{9_N}$ measured at 300 K with excitation at 290 nm.

Energy level splitting

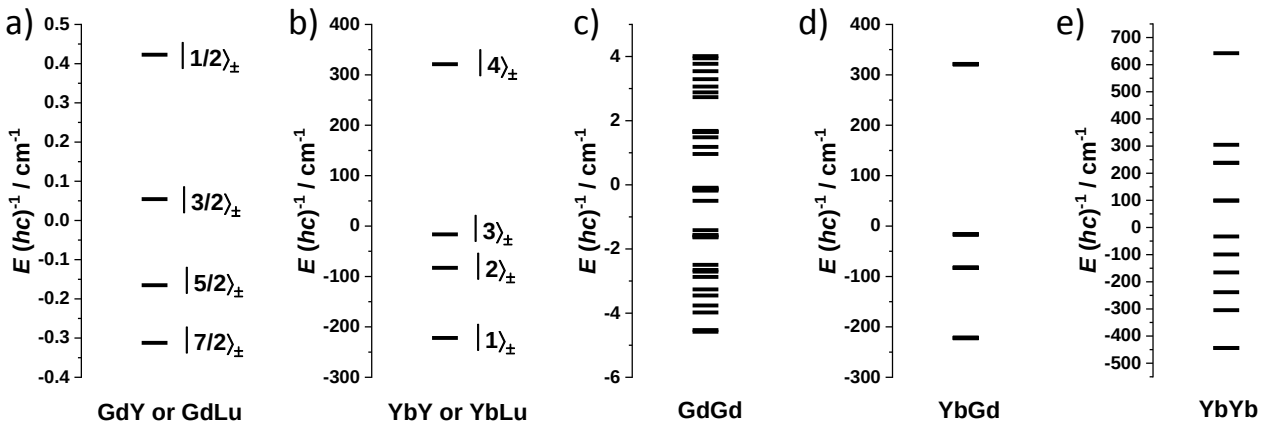

Figure S91. Energy level splitting in a) $\mathbf{5}_{\mathbf{N}}$ and $\mathbf{8}_{\mathbf{N}}$, b) $\mathbf{2}_{\mathbf{N}}$ and $\mathbf{3}_{\mathbf{N}}$, c) **10N**, d) $\mathbf{1}_{\mathbf{N}}$ and e) $\mathbf{4}_{\mathbf{N}}$.

Modelling parameters

Table S1. Best fit CF parameters (cm^{-1}) in Stevens formalism

Parameters	**2_N**	**3_N**	**5_N**	**8_N**
B_2^0/hc	-7.10	-7.10	$-1.84\cdot10^{-2}$	$-1.84\cdot10^{-2}$
B_4^0/hc	$4.78\cdot10^{-2}$	$4.78\cdot10^{-2}$	$1.95\cdot10^{-4}$	$1.95\cdot10^{-4}$
B_4^{+3}/hc	1.206	1.206		
B_4^{-3}/hc	$1.49\cdot10^{-5}$	$1.49\cdot10^{-5}$		
B_6^{-6}/hc	0.101	0.101		
B_6^{-3}/hc	0.699	0.699		
B_6^0/hc	$-1.22\cdot10^{-2}$	$-1.22\cdot10^{-2}$	$-6.67\cdot10^{-6}$	$-6.67\cdot10^{-6}$
B_6^{+3}/hc	0.239	0.239		
B_6^{+6}/hc	$3.12\cdot10^{-2}$	$3.12\cdot10^{-2}$		

Table S2. Best fit CF parameters (cm^{-1}) in Wybourne formalism

Parameters	**2_N**	**3_N**
B_{20}/hc	$-4.47\cdot10^2$	$-4.47\cdot10^2$
B_{40}/hc	$-2.21\cdot10^2$	$-2.21\cdot10^2$
B_{43}/hc	$2.35\cdot10^2 + i2.91\cdot10^{-3}$	$2.35\cdot10^2 + i2.91\cdot10^{-3}$
B_{60}/hc	$-1.32\cdot10^3$	$-1.32\cdot10^3$
B_{63}/hc	$-1.26\cdot10^3 - i3.69\cdot10^3$	$-1.26\cdot10^3 - i3.69\cdot10^3$
B_{66}/hc	$2.22\cdot10^2 + i7.18\cdot10^2$	$2.22\cdot10^2 + i7.18\cdot10^2$

Table S3. Exchange coupling parameters (cm^{-1}) in $\mathbf{1_N}$, $\mathbf{4_N}$ and $\mathbf{10_N}$ modelled with isotropic (J_{iso}) and anisotropic (D_{ex}) exchange, only isotropic exchange (J_{iso}) or only anisotropic exchange (D_{ex}).

Parameters	$\mathbf{1_N}$	$\mathbf{4_N}$	$\mathbf{10_N}$
J_{iso}/hc, D_{ex}/hc	-0.0309, -0.0607	0.0172, 0.0248	-
J_{iso}/hc	$1.78 \cdot 10^{-2}$	$-7.21 \cdot 10^{-3}$	-0.137
D_{ex}/hc	$-2.20 \cdot 10^{-2}$	$7.38 \cdot 10^{-3}$	-

Crystallographic tables

Table S4. Crystallographic data for $\mathbf{1_N}$ - $\mathbf{5_N}$

	$\mathbf{1_N}$	$\mathbf{2_N}$	$\mathbf{3_N}$	$\mathbf{4_N}$	$\mathbf{5_N}$
Formula	$C_{39}H_{50}GdN_{11}O_{14.5}Yb$	$C_{39}H_{50}N_{11}O_{14.5}YYb$	$C_{39}H_{50}LuN_{11}O_{14.5}Yb$	$C_{39}H_{50}N_{11}O_{14.5}Yb_2$	$C_{39}H_{50}GdLuN_{11}O_{14.5}$
Formula weight g/mol	1235.19	1166.85	1252.91	1250.98	1237.12
Temperature/K			100		
Crystal system			tetragonal		
Space group	$P4_12_12$	$P4_12_12$	$P4_32_12$	$P4_12_12$	$P4_12_12$
a/Å	17.6212(3)	17.5997(5)	17.5896(7)	17.5867(5)	17.6236(4)
b/Å	17.6212(3)	17.5997(5)	17.5896(7)	17.5867(5)	17.6236(4)
c/Å	29.1165(10)	28.9790(12)	28.9543(19)	28.9660(13)	29.0620(11)
α/°	90	90	90	90	90
β/°	90	90	90	90	90
γ/°	90	90	90	90	90
V/Å^3	9040.9(4)	8976.2(6)	8958.3(9)	8959.0(6)	9026.4(5)
Z	8	8	8	8	8
ρ_{calc} g/cm^3	1.815	1.727	1.858	1.855	1.821
μ/mm^{-1}	3.590	3.437	4.346	4.230	3.711
F(000)	4888.0	4688.0	4944.0	4936.0	4896.0
Crystal size/mm^3	0.414 × 0.067 × 0.062	0.282 × 0.141 × 0.122	0.478 × 0.08 × 0.068	0.288 × 0.075 × 0.065	0.284 × 0.14 × 0.086
λ (MoKα)			0.71073 Å		
2Θ range for data collection/°	3.628 to 50.698	3.64 to 55.752	3.644 to 54.96	3.644 to 55.754	3.632 to 56.694
Reflections collected	70720	84780	115628	155629	129451
Independent reflections	8257 [R_{int} = 0.0469, R_{sigma} = 0.0248]	10688 [R_{int} = 0.0574, R_{sigma} = 0.0350]	10256 [R_{int} = 0.0507, R_{sigma} = 0.0256]	10690 [R_{int} = 0.0642, R_{sigma} = 0.0273]	11234 [R_{int} = 0.0553, R_{sigma} = 0.0246]
Data/restraints/parameters	8257/127/635	10688/118/635	10256/126/636	10690/127/634	11234/99/635
Goodness-of-fit on F^2	1.110	1.067	1.164	1.139	1.101
R_1, wR_2 [I>=2σ (I)]	0.0239, 0.0594	0.0282, 0.0679	0.0278, 0.0632	0.0274, 0.0654	0.0246, 0.0565
R_1, wR_2 (all data)	0.0273, 0.0618	0.0341, 0.0710	0.0333, 0.0669	0.0356, 0.0698	0.0309, 0.0594
Residual electron density / e Å^{-3}	1.24/-0.78	1.46/-0.58	2.03/-0.96	1.88/-0.75	1.23/-0.63
Flack parameter	-0.015(4)	-0.017(3)	-0.018(3)	-0.027(3)	-0.027(3)

Table S5. Crystallographic data for **6_N - 10_N**

	6_N	**7_N**	**8_N**	**9_N**	**10_N**
Formula	$C_{39}H_{50}LuN_{11}O_{14.5}Y$	$C_{39}H_{50}Lu_2N_{11}O_{14.5}$	$C_{39}H_{50}GdN_{11}O_{14.5}Y$	$C_{39}H_{50}N_{11}O_{14.5}Y_2$	$C_{39}H_{50}Gd_2N_{11}O_{14.5}$
Formula weight g/mol	1168.78	1254.84	1169.07	1109.74	1219.40
Temperature/K			100		
Crystal system			tetragonal		
Space group	$P4_32_12$	$P4_32_12$	$P4_32_12$	$P4_32_12$	$P4_12_12$
a/Å	17.5884(5)	17.5856(5)	17.6312(4)	17.6029(6)	17.6388(4)
b/Å	17.5884(5)	17.5856(5)	17.6312(4)	17.6029(6)	17.6388(4)
c/Å	28.9743(13)	28.9382(12)	29.2044(12)	29.0488(15)	29.2421(10)
α/°	90	90	90	90	90
β/°	90	90	90	90	90
γ/°	90	90	90	90	90
V/Å^3	8963.3(6)	8949.2(6)	9078.5(6)	9001.1(8)	9098.0(5)
Z	8	8	8	8	8
ρ_{calc} g/cm^3	1.732	1.863	1.711	1.638	1.780
μ/mm^{-1}	3.558	4.467	2.802	2.650	2.969
F(000)	4696.0	4952.0	4720.0	4560.0	4840.0
Crystal size/mm^3	0.264 × 0.09 × 0.06	0.288 × 0.075 × 0.065	0.9 × 0.12 × 0.104	0.36 × 0.124 × 0.114	0.262 × 0.102 × 0.06
λ (MoKα)			0.71073 Å		
2Θ range for data collection/°	3.642 to 54.96	3.646 to 56.562	3.622 to 54.968	3.636 to 50.054	3.618 to 55.746
Reflections collected	118479	117907	118541	126935	153158
Independent reflections	10260 [R_{int} = 0.0595, R_{sigma} = 0.0280]	11099 [R_{int} = 0.0395, R_{sigma} = 0.0231]	10414 [R_{int} = 0.0524, R_{sigma} = 0.0287]	7955 [R_{int} = 0.0932, R_{sigma} = 0.0419]	10847 [R_{int} = 0.0568, R_{sigma} = 0.0250]
Data/restraints/parameters	10260/101/635	11099/98/634	10414/127/627	7955/127/634	10847/116/616
Goodness-of-fit on F^2	1.079	1.098	1.057	1.039	1.069
R_1, wR_2 [I>=2σ (I)]	0.0266, 0.0672	0.0232, 0.0553	0.0289, 0.0650	0.0342, 0.0769	0.0259, 0.0652
R_1, wR_2 (all data)	0.0312, 0.0699	0.0268, 0.0572	0.0362, 0.0693	0.0477, 0.0835	0.0311, 0.0680
Residual electron density / e Å^{-3}	1.50/-0.58	1.97/-0.73	0.53/-0.65	0.46/-0.44	1.34/-0.74
Flack parameter	-0.023(3)	-0.015(3)	-0.021(3)	-0.034(3)	-0.021(4)

Table S6. Ln-Ln distance (esd) in $\mathbf{1_N}$ - $\mathbf{10_N}$

Compound	Ln-Ln distance / Å
$\mathbf{1_N}$	3.4782(7)
$\mathbf{2_N}$	3.4567(7)
$\mathbf{3_N}$	3.4423(7)
$\mathbf{4_N}$	3.4435(7)
$\mathbf{5_N}$	3.4752(7)
$\mathbf{6_N}$	3.4563(7)
$\mathbf{7_N}$	3.4396(7)
$\mathbf{8_N}$	3.4913(7)
$\mathbf{9_N}$	3.4671(8)
$\mathbf{10_N}$	3.5035(7)

Table S7. Ln-$O_{nitrate}$ (esd) distances in $\mathbf{1_N}$ - $\mathbf{10_N}$

Compound	Nitrate site Ln		Nitrate site Ln*		
	r(Ln-O) / Å	*r*(Ln-O') / Å	*r*(Ln-O) / Å	*r*(Ln-O') / Å	*r*(Ln-O') / Å Disordered position
$\mathbf{1_N}$	2.439(5)	2.844(7)	2.383(6)	2.760(15)	3.892(19)
$\mathbf{2_N}$	2.406(4)	2.867(5)	2.332(4)	2.916(17)	3.969(11)
$\mathbf{3_N}$	2.378(5)	2.956(7)	2.309(6)	3.20(3)	3.954(14)
$\mathbf{4_N}$	2.380(5)	2.938(6)	2.314(5)	3.21(3)	3.943(13)
$\mathbf{5_N}$	2.433(4)	2.844(6)	2.380(5)	2.743(12)	3.951(15)
$\mathbf{6_N}$	2.397(4)	2.872(5)	2.324(4)	2.917(16)	3.949(11)
$\mathbf{7_N}$	2.372(4)	2.950(5)	2.309(4)	3.15(2)	3.964(11)
$\mathbf{8_N}$	2.463(4)	2.784(4)	2.418(5)	2.696(7)	3.915(17)
$\mathbf{9_N}$	2.430(4)	2.798(5)	2.344(5)	2.776(11)	3.960(11)
$\mathbf{10_N}$	2.460(5)	2.633(6)	2.490(4)	2.754(5)	-

References

1. Z. Asadi, M. Golchin, V. Eigner, M. Dusek and Z. Amirghofran, *Inorganica Chimica Acta*, 2017, **465**, 50-60.
2. P. C. Vesborg, I. Chorkendorff, T. Brock-Nannestad, J. R. Dethlefsen and J. Bendix, *Rev Sci Instrum*, 2011, **82**, 096102.
3. Bruker, *Bruker AXS, Inc. SAINT, Version 7.68A; Bruker AXS: Madison, WI, 2009*, edited by, Vol. p.
4. G. M. Sheldrick, *SADABS, Version 2008/2; University of Göttingen: Germany, 2003*, edited by, Vol. , p.
5. G. M. Sheldrick, *Acta Crystallogr A Found Adv*, 2015, **71**, 3-8.
6. G. M. Sheldrick, *Acta Crystallogr C Struct Chem*, 2015, **71**, 3-8.
7. G. M. Sheldrick, *Acta Crystallogr A*, 2008, **64**, 112-122.
8. O. V. Dolomanov, L. J. Bourhis, R. J. Gildea, J. A. K. Howard and H. Puschmann, *Journal of Applied Crystallography*, 2009, **42**, 339-341.
9. L. J. Bourhis, O. V. Dolomanov, R. J. Gildea, J. A. Howard and H. Puschmann, *Acta Crystallogr A Found Adv*, 2015, **71**, 59-75.
10. C. D. Buch, D. Mitcov and S. Piligkos, *Dalton Trans*, 2020, **49**, 13557-13565.
11. C. D. Buch, S. H. Hansen, C. M. Tram, D. Mitcov and S. Piligkos, *Inorg Chem*, 2020, **59**, 16328-16340.